MODELING, SENSING, AND CONTROL OF HUMAN BIPEDAL WALKING WITH FOOT SLIP

BY MITJA TRKOV

A dissertation submitted to the

Graduate School—New Brunswick

Rutgers, The State University of New Jersey

in partial fulfillment of the requirements

for the degree of

Doctor of Philosophy

Graduate Program in Mechanical and Aerospace Engineering

Written under the direction of

Dr. Jingang Yi

and approved by

_____

_____

_____

_____

New Brunswick, New Jersey

May, 2016

ABSTRACT OF THE DISSERTATION

Modeling, Sensing, and Control of Human Bipedal Walking with Foot Slip

by Mitja Trkov

Dissertation Advisor: Dr. Jingang Yi

Human walking is a fundamental motor skill that is developed at an early stage in our lives. Maintaining stable walking capability demands a substantial effort and requires synchronization and coordination of many neurological, sensorimotor and musculoskeletal systems. Moreover, disturbances such as foot slip require even more demanding walking control strategies for successful balance recovery and fall prevention. However, it is challenging to capture and model human motion and reaction to foot slip. Most of the existing slip-and-fall studies focus on clinical human experiments and few use control systems approaches to analyze the slip dynamics and human recovery mechanisms. Further challenges arise as few real-time sensing and robotic assistive technologies are currently available for reliably detecting foot slips and assisting human balance for slip-induced fall prevention.

The goal of this dissertation is to advance the understanding and knowledge of slip dynamics with emphasis on four interlaced topics: (i) analyzing and modeling the

shoe-floor interaction during foot slip, (ii) developing a novel bipedal modeling framework to capture human walking locomotion with foot slip, (iii) developing a novel linear inverted pendulum (LIP) modeling framework for balance recovery control, and (iv) developing new wearable sensing and robotic assistive devices for real-time detection of foot slip and effective prevention of slip-induced falls. In the first part, we present modeling of foot slip evolution and development based on a quasistatic friction force model. We present a model to obtain the normal force distribution on the shoe-floor contact patch. In addition, we extend the previously developed beam-spring network model and integrate it with the LuGre dynamic friction model. In the second part of the dissertation, we present a new bipedal modeling approach, where we relax the non-slip assumption used in the existing literature. We develop a hybrid bipedal model and the gait controllers to capture and predict human walking with foot slip. In the third part, we present a new two-mass LIP model for human balance control during walking and walking with foot slip. We extend the capture point based control approach and incorporate time-varying locations of the zero moment point and the LIP pivoting location. In the fourth part, we propose a novel real-time foot slip detection method using only wearable inertial measurement units. The developed slip-prediction algorithm is built on a dynamic model for bipedal walking and is also integrated with the human locomotion constraints. A slip indicator is introduced into the algorithm to detect the foot slip shortly after the heel-strike event. All of the above mentioned models, control strategies and devices are validated through the extensive experiments and simulations. In addition, we further design and fabricate a wearable robotic knee assistive device for slip balance recovery and slip-induced fall prevention. This device prototype serves as an enabling tool for future testing of possible robotic assistive fall prevention strategies.

Acknowledgements

First, I would like to express a special acknowledgement and appreciation to my advisor Dr. Jingang Yi, who has helped me with numerous advice, in shaping my research directions and studies as a graduate student and shaping my skills for my future career paths. He always took the time for any discussion when I encountered obstacles along my research path and to provide advice and encouragement.

Special acknowledgement goes also to Prof. Nenad Gucunski for introducing me to Rutgers and influencing my decision toward becoming a graduate student at Rutgers University, thus shaping my future with this lifetime experience.

Thanks also go to my committee members Prof. Haym Benaroya, Prof. Qingze Zou and Prof. Arthur D. Kuo for thoroughly reviewing my work and providing their feedback with constructive comments and suggestions. I am also grateful to all my labmates at Robotics, Automation and Mechatronics Laboratory, including Fei, Kuo, Yizhai, Kaiyan, Siyu, PengCheng, Moiz, Cullen and others for all helpful discussions and sharing their knowledge throughout these years at Rutgers. Special thanks go to Fei and Kuo, with both of whom I had a chance to collaborate closely and have unselfishly shared their knowledge and experiences that has helped me to expand my research ideas.

I would also like to thank my family, especially my kids Mila and Martin for being my sunshine during my study and in my everyday life and to my wife Ziva for her encouragement and support. Special thanks goes to my parents for constantly believing in my endeavours throughout my life as a graduate student and my life as a whole.

Dedication

This dissertation is dedicated to my family.

Table of Contents

List of Tables

List of Figures

Nomenclature

X, Y, Z A ground-fixed coordinate system.

$\mathcal{B}(x, y, z)$ A sole-floor contact frame attached to $\mathcal{C}$.

$\mathcal{C}$ The shoe-floor contact patch.

C_1 The origin of frame $\mathcal{B}(x, y, z)$ at the rear tip location of the contact contour.

C_2 The intersection point of x-axis and the contact contour $\mathcal{C}$ at the front tip.

$y_+(x)$ A function of the left portion of the contact contour denoted as $\widehat{C_1 C_+ C_2}$.

$y_-(x)$ A function of the left portion of the contact contour denoted as $\widehat{C_1 C_- C_2}$.

$P(x, y)$ A point on contact contour $\mathcal{C}$.

f_x, f_y, f_n The three-directional forces at point $P(x, y)$.

f_n The normal load distribution function.

f_{nx}, f_{ny} The longitudinal and the normalized lateral normal force factor.

l_s The maximum x-coordinate of the front tip point of $\mathcal{C}$.

s_H, s_T The scaling factors for the heel and the toe log-normal force distributions.

L_H, L_T The log-normal distribution density function for the heel and toe.

μ_H, μ_T The longitudinal normal force parameter for heel and toe, representing a mean of the variable's natural logarithm.

σ_H, σ_T	The longitudinal normal force parameter for heel and toe, representing a standard deviation of the variable's natural logarithm.
$\mathcal{C}_x$	The transverse area of the normal force distribution.
n_x	A number of PSECR sensor units within $\mathcal{C}_x$.
S_j	A PSECR sensor unit within $\mathcal{C}_x$ locate at (x, y_{sj}).
F_{sj}	The normal force measurements at location (x, y_{sj}).
C_+, C_-	The boundary points of $\mathcal{C}_x$ at $y_+(x)$ and $y_-(x)$.
$P_i(u)$	The ith-order Legendre polynomial defined on the interval $u \in [-1,\ 1]$.
a_i	The coefficients of the linear combination of a series of Legendre polynomials up to the 5th-order.
K	A normalization factor of the transverse normal load distribution at given x, due to mapping $y \mapsto u$.
$u(y)$	A coordinate transformation variable for Legendre polynomial.
N	A number of virtual cantilever beams.
h	The height of the virtual cantilever beams.
c	The side length of the virtual cantilever beams.
$\mathbf{f}_f^i, f_x^i, f_y^i$	The contact friction force vector and its longitudinal and transverse components.
$\mathbf{f}_d^i, \mathbf{f}_b^i, \mathbf{f}_e^i$	The boundary, bending and elastic forces on the ith beam.
δ_k^i	The bending deformation of the ith beam.
L_k	The maximum length of the contact contour in k-axis direction
$\mathbf{u_i}$	The position vector of the bottom tip of the ith beam.
μ	The coefficient of friction

$\mathcal{P}$	The soft-solid contact patch.
a	A side length of the square cross section of the beams.
$\boldsymbol{F}_f$, $\boldsymbol{F}_b$, $\boldsymbol{F}_e$	The total friction, bending and elastic force applied on $\mathcal{P}$.
$\boldsymbol{s}_i$, $\dot{\boldsymbol{s}}_i$	A position and velocity vector defined in the inertial fixed frame of the end of the ith beam that is rigidly connected to the solid surface.
$\boldsymbol{u}_i$, $\dot{\boldsymbol{u}}_i$	The absolute position and velocity vector of the free end of the ith beam in the inertial fixed frame.
m, m_i	A total mass of all the beams and a mass of the ith beam.
f_{fx}^i, f_{fy}^i	The longitudinal and lateral friction forces along the x- and y-axis
k_b^i	The bending stiffness of the ith beam.
k_b	The total bending stiffness of the soft material sample.
$\mathbf{l_i}$, $\dot{\mathbf{l_i}}$	The tip deflection vector and relative bending velocity of the ith beam.
k_e	The spring stiffness coefficient.
E	The elastic or Young's modulus.
$\mathcal{N}_i$	The index set of all the neighboring beams of the ith beam.
$\Delta\boldsymbol{u}_{ij}$	The spring deformation between the jth beam and ith beam.
u_{ij}^0	The length of the position vectors of the jth ($\boldsymbol{u}_{j0}$) and the ith ($\boldsymbol{u}_{i0}$) beams without spring deformation.
$\boldsymbol{\delta}^i$, δ_x^i, δ_y^i	The vector and its components along x- and y-axis of the local deformation of the ith beam's tip.
$\dot{u}_R^i$	The magnitude of the sliding velocity.
$g_k^i(\dot{u}_R^i)$	A function capturing Stribeck effect.
μ_{Ck}, μ_{Sk}	The Coulomb (kinetic) and static friction coefficients along the k-axis.

v_s The Stribeck velocity parameter.

α A parameter determining the shape of the function $g\left(\dot{u}_R\right)$ as a function of the ratio $|\dot{u}_R^i/v_s|$.

f_z^i The normal load on the ith beam.

$\sigma_{0k}, \sigma_{1k}, \sigma_{2k}$ The overall stiffness, micro-damping and viscous damping coefficients along the k-axis of the whole sample.

$\sigma_{0k}^i, \sigma_{1k}^i, \sigma_{2k}^i$ The stiffness, micro-damping and viscous damping coefficients along the k-axis of the ith beam.

$\hat{\sigma}_{0k}^i$ A parameter of stiffness of ith beam normalized with the normal load for $k = x, y$.

$f_{fk,ss}^i$ The steady-state friction force of ith beam.

f_{Sk}^i, f_{Ck}^i A static and dynamic friction force threshold along axis $k = x, y$.

R_0 The radius of the fingertip-like soft rubber specimen.

R_1 The radius of the cylindrical part of the rubber sample.

r The radius of the contact area.

h_1 The height of the cylindrical part of the rubber sample.

ν The poisson coefficient of the rubber material.

ρ A density of the rubber material.

F_z The desired total normal load.

p_0, p_2, p_{22}, p_4 The coefficients of the 4-th order polynomial of a fitted normal load distribution function $f(x, y)$.

q_i The relative joint angles $i = 2, \ldots, 7$.

$\boldsymbol{q}_a$ The gait configuration.

O_r The rotating center of the stance foot.

x_o, y_o The position of rotating center O_r of the stance foot.

$\boldsymbol{q}_s, x_s, y_s$ A slipping position vector and its components: longitudinal and lateral slipping coordinates.

ϕ The absolute angle of the stance foot with respect to the vertical direction.

C The stance foot-floor contact point.

$\boldsymbol{q}_e$ The generalized coordinates of the bipedal model.

$\boldsymbol{D}_s(\boldsymbol{q}_a), \boldsymbol{C}_s(\boldsymbol{q}_a, \dot{\boldsymbol{q}}_a), \boldsymbol{G}_s(\boldsymbol{q}_a), \boldsymbol{B}_s$ The inertia, Coriolis, gravity and input mapping matrices of non-slip single stance dynamics.

θ A progression variable.

$\boldsymbol{c}, \boldsymbol{c}_s$ A constant progression vector for non-slip and slip case.

$\boldsymbol{u}$ A vector of joint torque inputs.

$\boldsymbol{h}(\boldsymbol{q}_a)$ The virtual constraint.

$\boldsymbol{h}_d(\theta)$ The desired trajectory.

$\boldsymbol{H}_0$ A matrix of real coefficients specifying what is to be controlled.

F_n, F_x The normal and tangential force.

C_l, C_t The contact points of a leading and trailing feet.

$\boldsymbol{g}_l(\boldsymbol{q}_e), \boldsymbol{g}_t(\boldsymbol{q}_e)$ A slipping vectors of contact points C_l and C_t.

$\boldsymbol{D}_e(\boldsymbol{q}_e), \boldsymbol{C}_e(\boldsymbol{q}_e, \dot{\boldsymbol{q}}_e), \boldsymbol{G}_e(\boldsymbol{q}_e), \boldsymbol{B}_e$ The inertia, Coriolis, gravity and input mapping matrices of non-slip double stance dynamics.

$\boldsymbol{E}_e$ The matrix describing contact constraints.

$\boldsymbol{F}_e$ .... A vector of the collection of the tangential and normal forces at C_t and C_l.

F_{xt}, F_{nt}, F_{xl}, F_{nl} ..... The tangential and normal forces for trailing and leading leg.

$\boldsymbol{D}_{di}$, $\boldsymbol{C}_{di}$, $\boldsymbol{G}_{di}$, $\boldsymbol{M}_{di}$ ..... The matrices of the double-stance independent variable dynamics.

$\boldsymbol{q}_{di}$, $\dot{\boldsymbol{q}}_{di}$, $\ddot{\boldsymbol{q}}_{di}$ ..... A generalized coordinates vector of the double-stance independent variable dynamics and its derivatives.

$\boldsymbol{q}_{di}$, $\dot{\boldsymbol{q}}_{di}$, $\ddot{\boldsymbol{q}}_{di}$ ..... The desired trajectory of a generalized coordinates vector of the double-stance independent variable dynamics and its derivatives.

$\boldsymbol{K}_p$, $\boldsymbol{K}_d$ ..... The constant gain matrices.

$\mathcal{H}_s^d$ ..... The impact mapping.

$\boldsymbol{q}_e^-$, $\dot{\boldsymbol{q}}_e^-$ ..... The pre-impact joint angle and velocity of the single-stance phase.

$\boldsymbol{q}_e^+$, $\dot{\boldsymbol{q}}_e^+$ ..... The post-impact joint angle and velocity of the double-stance phase

α_d ..... The Bézier spline parameter.

$J_d(\alpha_d)$ ..... The objective function of the optimization process.

γ ..... A weighting factor in the objective function $J_d(\alpha_d)$.

t_0, t_f ..... The beginning and end of the time interval in the experiments used in the optimization process.

$\boldsymbol{q}_{di}^e$ ..... The measured joint angle profiles.

$\mathcal{S}_1$, $\mathcal{S}_2$ ..... The non-slip single-stance and double-stance phases states.

$\mathcal{S}_3$, $\mathcal{S}_4$ ..... The slip single-stance and double-stance phases states.

$\boldsymbol{D}_{es}$, $\boldsymbol{C}_{es}$, $\boldsymbol{G}_{es}$, $\boldsymbol{B}_{es}$ ..... The inertia, Coriolis, gravity and input mapping matrices.

$\boldsymbol{F}_{es}$, F_x, F_n The external force vector and its components: the frictional (tangential) and normal forces at the stance foot.

$\boldsymbol{q}_{es}$ A coordinate variable for single-stance slip.

$\boldsymbol{D}^s_{es}$, $\boldsymbol{C}^s_{es}$, $\boldsymbol{G}^s_{es}$, $\boldsymbol{B}^s_{es}$ The inertia, Coriolis, gravity and input mapping matrices of slip single-stance dynamics.

$\boldsymbol{F}_{es}$ The frictional (tangential) and normal external forces at the stance foot during slip.

ξ_s A variable (together with $\dot{x}_s$) used to show the zero dynamics properties of the system.

$\boldsymbol{F}_{e3}$ The external force vector for double-stance slip model.

$\boldsymbol{C}_f$ A constant for transformation of the external force vector.

$\boldsymbol{D}^s_{ext}$, $\boldsymbol{C}^s_{ext}$, $\boldsymbol{G}^s_{ext}$, $\boldsymbol{B}^s_{ext}$ The matrices of the slip double-stance dynamics.

$\boldsymbol{S}$ A constant transformation matrix from $\boldsymbol{q}_e$ to $\boldsymbol{q}_i$.

$\boldsymbol{v}_{\text{slip}}$ The slipping velocity of point C_l (along the x-axis direction) after the heel-touch impact.

M_1, J_1, L_1 A mass, mass moment of inertia and length of link 1 of double inverted pendulum model of slipping foot.

M_2, J_2, L_2 A mass, mass moment of inertia and length of link 2 of double inverted pendulum model of slipping foot.

a_1 The distance of a center of mass of link 1 from C_l.

d_s, d_t Distance between IMUs on the shank and thigh.

I_{t_i}, I_{s_i}, I_h The labels of IMUs attached to the thigh, the shank, and the heel for $i = 1, 2$.

$\boldsymbol{q}$ The generalized coordinates of slip dynamics.

$\boldsymbol{r}_1, \boldsymbol{r}_2$ The position vectors for the link 1 and link 2.

T, V The kinetic and potential energy of the 2-link limb.

g The gravitational constant.

$\boldsymbol{D}_d(\boldsymbol{q}_l), \boldsymbol{C}_d(\boldsymbol{q}_l, \dot{\boldsymbol{q}}_l), \boldsymbol{G}_d(\boldsymbol{q}_l), \boldsymbol{B}_d$ The inertia, Coriolis, gravity and input mapping matrices of 2-link slip dynamics.

$\boldsymbol{E}_d$ The contact constraints matrix.

$x_s, \dot{x}_s, \ddot{x}_s$ Slip displacement, velocity and acceleration.

M A total mass of link 1 and link 2 together.

M_a A simplified expression for $M_a = M_1 a_1 + L_1 M_2$

$\boldsymbol{\omega}_s, (\omega_{sz}), \boldsymbol{\omega}_t, (\omega_{tz})$ The IMU gyroscope (z-component) measurements attached to the shank and the thigh.

$\boldsymbol{x}$ A vector including EKF state variables.

$a_{s_i y}, a_{t_i y}$ The y-component measurements of the ith IMU accelerator attached to the shank and the thigh for ith link, $i = 1, 2$.

$\boldsymbol{a}_h, a_{hx}$ The heel IMU accelerometer measurement and its x-axis component.

α_s, α_t The angular accelerations of the shank and the thigh.

y_1, y_2, y_3 The outputs considered in the EKF design.

v_x^{Hip} The velocity of the hip along x-axis of $\mathcal{B}$.

$\boldsymbol{n}_y$ The white noise $\mathcal{N}(0, \Sigma_y)$ with variance matrix Σ_y.

$\boldsymbol{F}_{EKF}$ Jacobian matrices for the state dynamics.

$\boldsymbol{H}_{EKF}$ Jacobian matrices for the outputs at each iterative step in EKF implementation.

$S_I(t), S_s$ The slip status indicator variable and threshold value.

β, γ	A constant to compute the slip indicator factor.
$\theta_{\text{HH}}, \dot{\theta}_{\text{HH}}, \ddot{\theta}_{\text{HH}}$	Hip-Heel absolute angle, angular velocity and angular acceleration.
$\theta_{\text{Sh}}, \theta_{\text{He}}$	Shank and foot angle.
$\theta_{\text{Sh}}^{\text{thr}}, \theta_{\text{He}}^{\text{thr}}$	Shank and foot angle threshold value.
xoz	The ground-fixed frame.
C_1, C_2, C	Ground fixed coordinate system of LIP model
C_1, C_2, C	Points located on each end of LIP and its center of mass.
m_1, m_2	Masses at each end of LIP model.
x_1, x_s, x_c	The horizontal positions of the two masses and the center of mass C in xoz.
h_1, h_c, z_c	The vertical distances from C to C_1 , from C to C_2 and from C_1 to C_2.
F_z, F_x	The normal and friction force at point C_2.
P, u	ZMP location and its x-axis coordinate.
δ	Horizontal distance between points C_1 and C_2.
ξ, ξ_d	Capture point and desired capture point.
Σ_{ns}, Σ_s	The continuous motion dynamics of LIP model during normal walking and walking with foot slip.
ω_w, ω_s	Constants used in capture point for normal walking and walking with foot slip
Δt	Duration of a single stance phase.

Chapter 1

Introduction

1.1 Motivation

Walking is a fundamental and energy-efficient trained human motor skill [1]. Walking gait is inherently unstable and balance control is constantly required to maintain dynamically stable posture. Unexpected perturbations such as slipping, tripping and stumbling affect dynamic stability and can cause a human to fall. Human responses and reactions to such disturbances require complex neurological and biomechanical processes to recover dynamic stability and prevent falls. These actions are related to the individuals' sensory capabilities of perturbation detection (i.e., proprioceptor, somatosensory and vestibular sensory systems), and the musculoskeletal ability to perform proper responses to the disturbances.

The elderly often suffer from degraded sensory and musculoskeletal capabilities. They are at high risk of falls due to changes in their gait patterns, lower muscular strength and slower reaction rates. More than one third of adults older than 65 years fall each year [2]. Falls due to slipping, tripping and stumbling is the most common injury mechanism among elderly [3]. Moreover, falls due to slips and trips are also present among occupational populations, such as during delivery of mail [4] and among hospital employees [5]. Slipperiness and slipping were shown to contribute to 40-50% of occupational slip, trip and fall (STF)-related injuries [6]. The fall-related economic and societal costs for elders and professional workers are enormous [3]. In the US only, the fall-related costs in the elderly were over 19 billion US dollars in 2000 and the costs

are likely to increase in the future due to the aging population [7,8]. Fall-related injuries for professional workers also increased by 42% from 2008 to 2012 in the US [9]. Foot slip is one of the three major causes for falling injuries and therefore, it is critical to understand slip dynamics and slip detection and slip-induced fall prevention.

We currently lack theories and design tools to successfully predict and detect foot slip and to prevent slip-induced falls.

Slip-and-fall consists of a series of continuously rapidly changing, whole-body human movements and it is challenging to capture and model human motion and reaction to foot slips. The complexity of fully understanding the biomechanics and neuro-musculoskeletal control in slip-and-fall lies in several aspects. First, foot slip dynamics and its impacts on human walking are complicated. Human motor control and reactions to foot slip are also complex due to the high-dimensional, redundant human movements. It is difficult to precisely model the balance recovery strategies. Further challenges arise as few real-time sensing and robotic assistive technologies are currently available for reliably detecting the foot slips and assisting human balance after foot slips.

The goal of this dissertation is to address these challenges with four intertwined research directions as illustrated in Fig. 1.1. More specifically, the dissertation focuses on: (i) the development of the shoe-floor interactions models for slip prediction; (ii) the development of the analytical models to understand and characterize human balance recovery reactive strategies, (iii) using human kinematics and kinetics measurements to detect foot slip in real-time; and (iv) using the research outcomes of the first three topics to develop a robotic assistive device for slip-induced fall prevention.
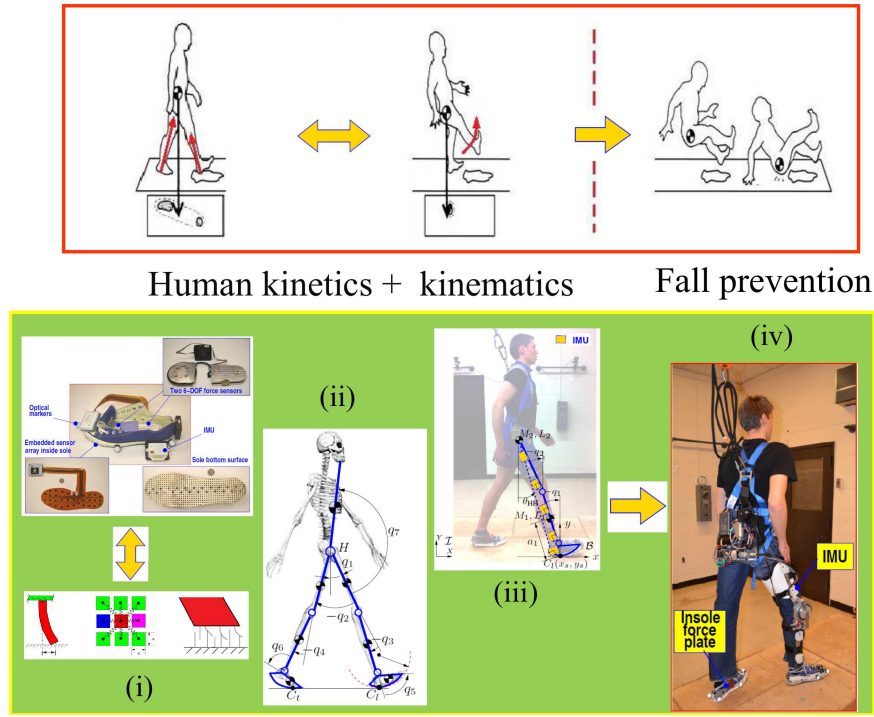
Figure 1.1: Concept schematics of slip prediction, detection and fall prevention through four approaches (i)-(iv) discussed in this dissertation.

1.2 Background

Slip-and-fall has been extensively studied in the past two decades. For a good review, readers can refer to [10, 11] and references therein. Most of these studies focus on human subjects and clinical experiments and few use human locomotion dynamics to analyze the slipping mechanism. In this dissertation, we focus on foot slip dynamics, sensing and prediction and prevention of slip-induced fall. The study of slip-and-fall prevention is related to several research topics such as slip biomechanics, bipedal robotics, in-situ sensing of human motion and wearable robotic assistive devices. Each of these four research topics will be discussed and covered individually in the following chapters. We first review the related work of each topic here.

1.2.1   Slip prediction using friction force models

Shoe-floor interactions play an important role during human walking and slip events. In [10, 12, 13], required coefficient of friction (RCOF) is used to quantify the slipperiness of the shoe-floor interactions and to determine and predict the slips of the interactions. The RCOF is defined as a ratio of the *total* friction force and the *total* normal force. The measurement of slipperiness has also been discussed in [14] and the devices to measure the friction between the shoe and the floor are reviewed in [15]. In [16], a quantitative description of the heel-floor contact dynamics is presented for slip events on oily surface of varying inclination. The kinematics of the human body's center of mass (COM) and the center of pressure of shoe-floor contact are used to predict the RCOF in real time during walking [17, 18]. While RCOF is widely used as a slip prediction parameter, a recent study [19] suggests that it is possible to predict slip by only the magnitude of the shear force after heel strike.

All of the above-mentioned studies mainly consider the total friction (i.e., shear) or the normal forces, not the force distributions on the sole-floor contact patch. Indeed, the distribution of the three-dimensional (3D) ground reaction forces (GRF) are critical not only for slip and fall applications but also for human gait and clinical studies. For instance, the normal GRF and its distribution are used to predict and diagnose abnormal gait for Parkinson disease patients [20]. The 3D foot plantar forces (i.e., normal and shear forces) are important for studying biomechanics with clinical applications for patients with diabetes and osteoarthritis [21, 22]. However, sensing and obtaining shear force distributions on the shoe-floor interactions is not as straightforward as the normal GRF [21]. Although some relationships might exist between the shear friction forces and the normal contact forces [23], a recent study in [24] shows that the peak values of these forces do not occur at the same location or time. A set of separately multiple sensor arrays are desirable to obtain the complete 3D GRF and their distributions.

Various GRF sensors have been developed in the past several decades [21]. To

measure the 3D GRF in a laboratory, a force plate is the most commonly used device. However, force plates cannot be used for monitoring daily activities outside the laboratory and they cannot provide the force distribution, either. In recent years, wearable insole pressure measurement devices were developed to obtain the normal GRF [20, 25], or 3D GRF [23, 26–29]. Some of the sensor arrays can be used to measure and obtain the normal GRF [20, 28] or 3D GRF distributions (e.g., [26]). However, none of these GRF systems aim at measuring the sole-floor interaction forces and for slip-and-fall studies. Moreover, although the 3D foot plantar pressures and their distributions are related to sole-floor interactions, few studies report the interactions (e.g., friction force distribution) between the shoe sole and the floor surface. In this dissertation, we develop a modelling framework and analysis to obtain stick-slip interaction on the shoe-floor contact to predict slip.

1.2.2 Dynamic friction force model for soft-solid contact

Contact modeling between soft materials and solid surfaces plays an important role for designing and controlling robotic and mechatronic systems, ranging from robotic grasping [30, 31], bipedal walking [32], to tire-road interactions in autonomous vehicles [33], etc. High-fidelity soft-solid contact model and tactile sensing are crucial for safe and effective control of these robot-environment interactions [34].

Contact model is highly related to robotic grasping and tactile sensing. For example, contact mechanics are used to capture the tactile sensing principles and models in [35]. The readers can refer to [34] for a review of tactile sensing. For soft-solid contact with a finite area between a soft materials and the rigid surface, the contact interaction forces are complicated [36, 37]. Besides the linear or nonlinear elastic responses, time-dependent characteristics exist in soft-solid contact [36]. To capture these complex behaviors, a set of virtual beams are used to model the fingertip contact and to obtain a dynamic model for sliding motion and stick-to-slip transition [37, 38].

Virtual springs are also used to connect any two neighboring beams to capture the elastic and shear effect. The Coulomb friction characteristic is used in [37, 38] to describe the stick-to-slip transition.

Tire-road interaction is another application of the soft-solid contact problems. Unlike the robotic fingertip contact model discussed in [37, 39, 40], the tire-road normal contact force distribution is different due to the tire's hollow and thin-layer structure. The LuGre dynamic friction model uses the bristle deformation to capture the frictional forces between two rigid contacts [41] and has been used to interpret and calculate the *total* tire-road friction forces for a given normal force distribution [42–46]. In [33, 47, 48], a beam-spring network model is used to model the rubber deformation and the friction force distributions on the contact patch during the stick-to-slip transition. Embedded force sensors are used to validate the modeling results. However, only static contact is considered in [33, 47] and no sliding or dynamic motion is assumed between the tire and the road interactions.

We propose a dynamic friction force model to capture the distributed friction force for the general soft-solid contact patch, and apply this modeling approach to capture the shoe sole-floor contact interaction for slip prediction. To demonstrate the method, we develop a computational model to obtain deformation and friction force distribution within the soft-solid contact patch. A fingertip-like soft rubber sample is used as an experimental example to validate the modeling framework.

1.2.3 Modeling and control of robotic and human walking and walking with foot slip

Analytical modeling approaches are commonly used to analyse the behaviour of biomechanical systems and processes. The biomechanics of human walking are commonly

characterized as a bipedal dynamics model. Modeling and control of the bipedal dynamics model is complementary to the understanding of clinical observations and advances knowledge that is not easy or convenient to be experimentally tested and obtained.

Bipedal modeling and control are extensively used in robotic walker design in the past decades; see [49] and the references therein. Due to the foot impact with the ground in each strike, a hybrid dynamic model is commonly used to describe the continuous dynamics in the single- or double-stance periods with discrete-switch mappings to capture the foot contact impacts. Point or flat foot models are employed in these bipedal robotic dynamics. Using the hybrid zero dynamics concept [50], a low-dimensional normal human walking model has been presented in [51] and a state feedback control is designed to track the gait profile parameterized by the stance phase variable, rather than time [49].

Use of bipedal robotic dynamic models to study human locomotion is reported recently. In [51], the bipedal model is used to study human gaits with consideration of fixed ankle joints. Both the single- and double-stance phases are included in the model and a hybrid zero dynamic control is designed to track the human gait profile. Although the kinematic variables such as hip, knee and HAT (head, arms and trunk) joint angles match the human gaits, the predicted GRFs have large discrepancies with experiments. In [52], an optimization process is used to determine the values of the parameters of the bipedal model to match the kinematics of human gaits. Only single-stance locomotion is considered in the model without the HAT. The kinematics of the model predictions match the human gaits and no predicted GRF results are reported. The models in [51, 52] use the circular curved foot-floor contact that has been developed in [53].

Simple linear inverted pendulum (LIP) model or its variations, such as spring-load inverted pendulum (SLIP) model, are also used to capture human walking and running

and humanoid robot control [54, 55]. The LIP or SLIP models are simple and are attractive to describe motion relationship between COM, zero moment point (ZMP) and other motion variables [56]. Similar to the work in [57] for studying human balance, the concepts of the capture point (CP) and the divergent component of motion (DCM) are proposed for humanoid robots control in [58] and [59], respectively. The CP- or DCM control of humanoid robots are also demonstrated in recent work [60–62].

All of the above-mentioned bipedal models are built on the assumption that the foot-floor contact friction forces are large enough to prevent the foot from slipping and thus, cannot be used and applied directly to study slip-and-fall walking gaits. Several studies use modeling based approach to investigate stability and reaction controls during foot slip. In [11], a 7-link, 9-degree-of-freedom (DOF) walking model in the sagittal plane with a 16-element foot model is used to simulate the human reaction control to a novel slip. In [63], a simulation model is optimized with human experiments and using this model, stability results are obtained and compared with the dynamic balance analyses by a simple invented pendulum model. The 2D musculoskeletal model in the sagittal plane is also used in [64] to determine the impact of the reduced RCOF on gait kinematics. Kinematic and muscle activity-based data-driven analysis (e.g., Lyapunov exponents) are used to capture the walking stability [65].

In this dissertation, we develop a multi-link bipedal model and controller to capture human walking with foot slip. The proposed model complements the existing literature and experiments are conducted to validate the model for normal walking and walking with foot slip gait.

1.2.4   Foot slip detection in human walking using wearable sensors

Effective real-time slip detection and prediction is critical for developing assistive and rehabilitation devices for preventing human slip-induced falls during human walking.

Many clinical studies mainly focus on data analysis of human gait parameters

changes to predict slip initiation [66]. Findings from these studies use gait parameters such as heel contact velocity and heel displacement as an indicator when balance recovery under foot slip is possible. For example, a criteria for slip recovery is defined as the heel velocity less than 50 cm/s and the slip distance less than 10 cm [66]. The study in [67] instead argues that these margins are conservative and that twice of those threshold values are recorded during successful slip recoveries. The studies in [16] re-confirm the thresholds in [66]. The large variations of the recovery margins reported in these publications imply the complexity of the slip dynamics.

It is suggested that slips most likely occur shortly after the heel-strike event [68]. In [69], various specific profiles of the heel slip acceleration, velocity and displacement are observed and reported. A quantitative description of the heel-floor contact dynamics is presented for slip events on oily surfaces in [16]. The heel velocity and the forward slip distance are also related to the utilized coefficient of friction at the shoe-floor interaction [70]. Prediction of slip severity is also assessed by inspecting the pre-slip gait parameters [71]. Unfortunately, the correlations of the pre-slip parameters with slip predictions are not reliable and robust.

Slip biomechanics are closely related to human walking dynamics. Physical principle-based dynamic models are widely used to design bipedal walking robotics and humanoid robots [49]. Use of the bipedal dynamic models to study human locomotion is also reported in recent years [52]. Most of these bipedal models however assume non-slip contact conditions between the foot and the floor. In [11], a seven-link, nine-DOF dynamic model is used to simulate the human reaction control to a novel slip. It is difficult to use the complex simulation model in [11] to analytically capture the slip characteristics. In [72], an analytical bipedal dynamic model is presented to characterize the human gaits under foot slip, but no slip detection algorithm is discussed.

In this dissertation, we present a slip detection system and algorithm for real-time

applications. The presented slip detection and prediction method uses only the wearable IMUs and thus, it is convenient for slip detection during personal daily activities. The slip detection algorithm not only detects but also predicts slip propagation allowing to assess the severity of the slip. Such method has the advantage over the well-established RCOF-based slip predictions because no prior measurement information is needed. Another drawback of using RCOF is the requirement of the expensive wearable force plates and is not practical for slip detection in human personal daily activities. On the other hand, the inertial measurements units (IMUs) have been commonly used to capture the dynamic motions and posses attractive features such as low-cost and lightweight etc. For the presented slip detection system, only the IMUs are attached to the lower limbs. Extensive multi-subject testing was conducted to validate the slip detection and prediction algorithm.

1.2.5   Robotic knee assistive device for slip-induced fall prevention

Currently, limited number of devices aim at slip detection and fall prevention in the commercial market and research labs.

An active slip prevention method was reported in [73] by using an intelligent laterally-extendable shoe to increase the base of support (BOS) during slip and therefore increase the dynamic stability and recovery possibility. In a same study the relationship between a ZMP and a BOS during slipping was also analysed. Fall prevention using wearable airbags was proposed in [74, 75].

Although a number of exoskeletons, humanoid robots and other assistive or orthotic devices have been developed, those devices are not suitable to be used as slip prevention device since most of them were not designed to meet the requirements of lightweight, fast response time, and high torques in a fraction of a second. The wearable device with the similar performance requirements as fall prevention devices are ankle and knee perturbators reported in [76–78] or a series elastic remote knee actuator

(SERKA) [79]. All of these devices are remotely actuated and cannot be directly used in slip-and-fall testing. The most common slip-induced fall prevention strategies are a repetitive slip training for healthy subjects with aim to train subjects cognitive reaction skills to slip [80–82]. Such repetitive slip training were shown to improve humans' motor skills for slip balance recovery for 6 months or longer [83].

It was reported that during slip occurrence, the knee and ankle joints experience the highest torque deviation compared to normal walking torque profiles [84,85]. It is also suggested that the corrective reactions to unexpected slip produced by the knee and hip moments are crucial towards successful slip recovery [84,86]. Furthermore, the knee strength, particulary extension peak and explosive strength, are reported as the most important factor in slip recovery [87]. Based on these observations, we hypothesize that the robotic knee assistive device could help provide additional torques to prevent slip-induced falls during slip recovery. We design and fabricate robotic knee assistive device with the integrated slip detection system that can provide assistance for human subjects to prevent slip-induced falls under foot slip.

1.3 Dissertation outline and contributions

There are seven chapters in this dissertation. Chapter 1 presents the introduction and background. In Chapter 2, we discuss the shoe sole-floor interactions and the friction force model for slip prediction and detection. In Chapter 3, a dynamic friction force model is presented for a general soft-solid contact application. A robotic bipedal dynamic model for human walking with foot slip is presented in Chapter 4. In Chapter 5, we present a slip detection scheme using the human kinematic measurements obtained from the IMU. A novel robotic assistive device for slip-induced fall prevention and a balance recovery control are presented in Chapter 6. Conclusions of the dissertation and discussion of the future work are presented in Chapter 7. The content of each

chapter is described as follows.

In Chapter 2, we first present a novel model to obtain the normal load distribution within the shoe sole-floor contact area. We present a computational model for the friction force and deformation distributions with the capabilities and attractive features under conditions such as: (i) contact patch has irregular shape and is constantly changing with time, and (ii) the boundary force is evenly distributed across the entire contact patch, due to the top of the rubber shoe sole being rigidly connected to the shoe. The model predictions and experimental results show similar trend of slip propagation from the regions with lower normal loads to the regions with the higher normal loads.

In Chapter 3, we extend the approaches in Chapter 2 and present a dynamic friction force model for a general soft-solid contact application, such as shoe-floor interactions. Unlike the quasistatic friction force models, the dynamic model includes frictional force properties such as Stribeck and time-dependent effects and thus captures contact friction dynamics and sliding motion. The proposed model is capable of capturing the stick-to-slip motion during the steady state behaviour and the model predictions are validated and demonstrated through the experimental results.

In Chapter 4, we present a 7-link robotic bipedal dynamic model to study human walking with foot slip in a sagittal plane. We relax a non-slip condition assumption of the stance leg at the heel strike and derive a slip dynamics model. The hybrid bipedal dynamics model includes the single-stance and the double-stance phases for both the non-slip [49, 51, 52], and foot slip cases. A hybrid zero dynamic controller using feedback linearization is designed to track the human gait profile using a progression variable rather than time [50]. The model uses curved feet [51, 52] with a radius equal to a shoe-floor contact rolling geometry [53] that are obtained from the experimental data.

In Chapter 5, we present a slip detection and monitoring device using the lower-limb kinematic measurements obtained from the wearable IMUs and the bipedal models developed in Chapter 4. Real-time slipping heel distance and velocity monitoring

are based on the 2-link dynamic model with integrated sensing fusion through an EKF design. We introduce a novel slip indicator to detect the initiation of the foot slip after the heel strike. The slip indicator captures the physical behavior of the movement of human COM with respect to the stance foot in a sagittal plane. The hip-heel angular acceleration (similar to the COM-heel angular acceleration) and the heel slip acceleration information are used to compute the slip indicator factor. Successful and effective slip detection and monitoring algorithm results are validated through extensive multi-subject experiments.

In Chapter 6, a two-mass LIP model is presented for balance recovery control of human walking with foot slip. We use a CP concept to design a balance recovery control. Extensive experiments are conducted to validate the proposed proposed slip recovery approach. In addition, we present a design of a novel robotic knee assistive device for slip-induced fall prevention. The wearable device has several attractive features, such as high torque and high angular velocity, lightweight, clutch-type mechanism and rotary series elastic actuation. The demonstration of the effectiveness and functionality of the device is out of the scope of this dissertation and remains as the future work.

The main contributions of this dissertation are described in details as follows.

1. A novel shoe sole-floor interaction modeling is proposed for human slip prediction. Combining the proposed normal load distribution model with the extended quasistatic friction force model allows us to obtain the shoe-floor contact interactions, such as friction force and slip distributions. The proposed models and computation of the deformation distribution can be used for accurate slip prediction. Analysis of the friction force and slip distribution of the shoe-floor interactions is novel for slip prediction and also complements the current understanding and knowledge of biomechanics of slip and falls.

2. The proposed dynamic friction force model in Chapter 3 offers a substantial advantage over the quasistatic friction force model by capturing sliding contact motions. It also includes contact friction dynamics and properties such as Stribeck and time-dependent effects. In comparison to quasistatic model, the dynamic model offers a simplified computation of friction force and deformation distributions. Besides the shoe-floor interaction, such model can also be applied to other types of soft-solid contacts in mechanical systems.

3. The simulation of human walking with foot slip is presented using the newly developed 7-link planar bipedal model and the hybrid zero dynamics controller. The new model extends the robotic bipedal models to study human walking and successfully predicts human gait with foot slip. Besides relaxing the assumption of non-slip foot-floor contact, compared with the other existing work, the new model comprehensively includes innovative features and properties such as: experimentally validated foot contact shape, active ankle joints, and also dynamic model and controller for the the double-stance phase in walking gaits, which is crucial for slip and fall locomotion.

4. A novel real-time slip detection and monitoring system is presented in the dissertation. The slip detection system uses only the IMU measurements. The slip detection algorithm successfully detects slip shortly after the heel strike even prior to the humans somatosensory or proprioceptor sensory systems and also monitor the severity and evolution of the slip. To our best knowledge, no such slip detection system has been reported before. Attractive features such as small size, lightweight and low cost make the slip detection system convenient and attractive to be used in personal daily life and also for robotic assistive device for fall prevention.

5. A novel two-mass LIP model is developed and used to design the balance recovery control for human normal walking and walking with slip gaits. CP-based walking

control is extended to separately capture the ZMP control and the walking pivoting point. The proposed human-inspired balance recovery control during foot slip can be used to design a new wearable assistive device to prevent slip-and-fall.

6. Finally, we present a preliminary design of a new wearable robotic assistive device for slip-induced fall prevention. The device has a set of unique design features such as a compact rotary series elastic actuator, capable of producing a high torque ($90\ Nm$) and high angular velocity ($360\ deg/s$). With an integrated clutch mechanism, the device is actuated only during the presence of foot slip and otherwise allows unconstrained motion during normal walking. Integration with the slip detection and prediction algorithms, the development of the robotic knee assistive device provides an enabling tool to explore the possibility of preventing slip-induced falls.

Chapter 2

Static Model for Shoe-Floor Interactions During Foot Slip

2.1 Introduction

Sudden changes of coefficient of friction during walking, such as stepping on a wet or icy floor, can cause humans to slip and fall. Pure grip or low friction coefficient between the shoes and the ground was reported to be the primary reason for slipping [88]. Therefore, the understanding and prediction of shoe-floor interactions is critical for the control and prevention of human slips and falls.

The most widely used parameter to determine and predict the slips of the shoe-floor interactions is RCOF [10, 12, 13], defined as a ratio of the total friction over normal ground reaction forces. Although these studies indicate the importance of the friction force in slip prediction, they do not clearly present the initiation and evolvement of the slip on the shoe-floor contact patch. Slip evolution is related to the force and deformation distributions over the contact area and provides the critical understanding of the foot slip mechanisms and dynamics.

Simultaneous measurement of shear and plantar pressure distribution under the shoe sole or barefoot is challenging [89] because of limited sensing capability on the market or in research labs. Only a few customly designed transducer-array [90, 91] or deformation-based measurement systems [24, 92] are reported to measure the shear and plantar pressure simultaneously. In [93], foot skin partial incipient slip distribution within the foot-floor contact area was measured during barefoot walking using optical

based system. Most of these measurement systems have been developed for clinical application, such as risk evaluation of diabetic ulcers [24, 90, 91] and none of them has been used for foot slip prediction. Due to the challenges in obtaining shear force distribution under the foot, several models were developed for predicting these forces during barefoot walking [94, 95]. These models are based on measured plantar pressure distribution and the total ground reaction forces. Effectiveness of those model predictions is compared to experimentally measured friction force distribution [91].

There exist devices that measure slipperiness between the shoe and the floor [15] and also stationary and wearable force plates to measure the total friction forces [29]. However, to our best knowledge, no shear force prediction models are reported for the shoe-floor interaction. The focus of this chapter is the friction force distribution on the shoe-floor contact patch for slip prediction.

Friction force modeling was studied also in many other soft-solid contact interfaces and applications, such as tire-road interactions [33, 44, 96] and grasping and tactile sensing applications [37, 38]. Studies in [33, 37, 38, 97] showed that in a presence of large shear forces at the soft-solid contact, slip gradually evolves (i.e., incipient slip) through the whole contact area. Such observations inspired us to investigate if a similar approach could be used for foot slip prediction.

To capture the shoe-floor friction force and sole deformation distribution, we extend the beam-spring network model that was developed for studying tire-road interactions [33, 98]. Compared to the tire-road interaction, shoe-floor interactions are much more complex due to the irregular contact footprint and pressure distributions and the dynamic, time-varying configurations during walking and slip-and-fall gaits.

We first build a shoe-floor sensing suite that integrates pressure-force-kinematics measurements using wearable sensors with a stationary laser-based sole-floor contact footprint system, as shown in Fig. 2.1(b). Two types of force sensor systems are used in the sensor suite: two six degree-of-freedom (6-DOF) force sensors at the forefront

and at the heel are placed inside the shoe to measure the 3D GRF and torques and a set of 2D pressure sensor arrays are implanted inside the soles. The details of the 6-DOF force sensor are discussed in [29] and the sole pressure sensors are similar to the pressure-sensitive, electric conductive rubber (PSECR) sensor discussed in [47]. Extensive experiments were conducted to test and validate the modeling and analysis framework.

The main contributions of the work in this chapter are twofold. First, for the first time, this dissertation discusses the friction force and slip distributions of the shoe-floor interactions during slip and fall. Most existing work use the resultant total friction and normal forces to describe and quantify the occurrence of the slip and therefore, the work presented here complements the understanding and knowledge of the biomechanical aspects in foot slip. Second, this chapter presents a novel, wearable sensing system to capture the pressure-force-kinematics interactions between the sole and the floor. To our best knowledge, there is no single mobile sensing system available in the market or other research labs to measure the 3D shoe-floor contact forces and their distributions for studying slip and falls or other related applications.

2.2 Shoe-floor interaction sensing systems

Figure 2.1 shows the integrated kinematics/kinetics distribution sensing suite for shoe-floor interactions. The sensing suite consists of multiple modality sensor systems: (1) the optical markers for indoor motion capture system (8 Bonita cameras from Vicon Inc.) and small wireless inertial measurement units (from Motion Sense Inc.) to obtain the kinematic information of the limb. The IMU consists of a tri-axial gyroscope, a tri-axial accelerometer and magnetometers to measure the three attitude angles. (2) Two six degree-of-freedom (6-DOF) force/torque sensors (model SS-1 from INSENCO Co., Ltd) that are located inside the shoe to measure the total 3D forces and torques at the
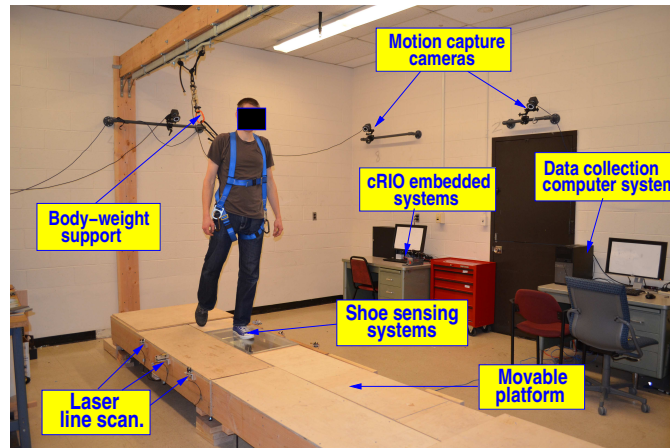
(a)
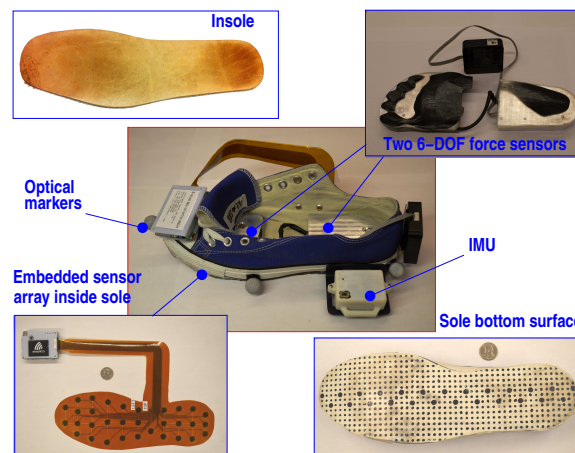
(b)

Figure 2.1: (a) The slip and fall experimental setup with various sensor suites. (b) Instrumented shoe kinematics/kinetics/forces distribution sensing suite.

forefoot and hindfoot contacts. These 6-DOF force sensors are thin (12 mm thick for the forefoot sensor and 17 mm thick for the hindfoot sensor) and can be embedded underneath insoles (Fig. 2.1). The force and torque measurements are transmitted through wireless Ethernet protocol to the host computer. (3) A pressure-sensitive, electric conductive rubber (PSECR) sensor array (of 32 independent sensor units) is embedded inside the sole rubber layer to measure the shoe-floor contact pressure distribution. The PSECR sensors are customly designed and fabricated. These flexible sensors are packaged within a thin-film layer and embedded into a molded urethane rubber layer (5mm thick). The thin rubber layer is then glued to the bottom of a regular sport shoe.
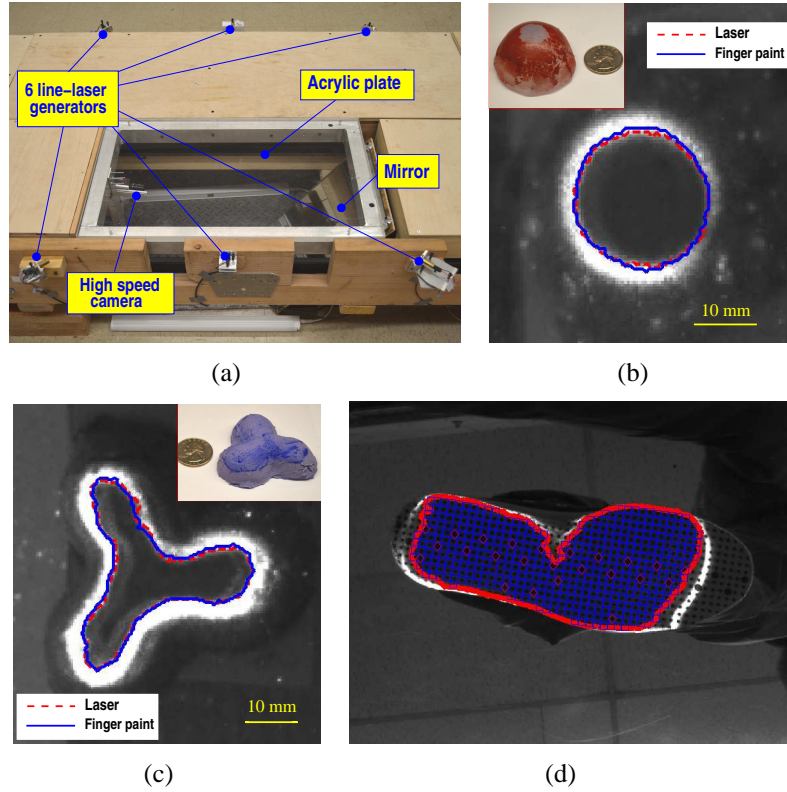
Figure 2.2: (a) Laser-based contour footprint setup. Validation results of the laser-based contour measurements by a (b) spherical regular object and (c) concave irregular object. (d) The outcomes of the contact contour and sole surface dots (blue squares) and landmarks (red diamonds) detection on a snapshot during normal human walking gait.

To measure the deformation of the shoe-floor contact and to calculate the local slip distribution, six laser line generators and a camera system are used to obtain the shoe-floor contact contour. Figure 2.2(a) shows the shoe-floor contact contour measurement system. Six laser line generators are spread out and placed at various directions to precisely aim at the shoe sole surface right above the floor surface. These lasers are used to form a closed contour on the sole bottom surface, see Fig. 2.2(b)-(d). A high-speed camera (Prosilica GX1050C color camera, 1024×1024 pixels, 112 fps) is mounted underneath the transparent acrylic floor surface. A reflective mirror is used to increase the optical distance between the camera and the footprint. The size of the square imaged area is 350×350mm and the resolution is 0.3mm/pixel. The error due to the

distortion of the lens is around 0.07mm. To validate the laser-based contour measurements, Figures 2.2(b) and 2.2(c) show two testing results for a regular shape object (a rubber hemisphere) and an irregular shape object (concave rubber toy), respectively. The comparisons between the laser-based contour measurements and the finger-paint contour in the figure confirm the non-intrusive approach to obtain the contact contour. Figure 2.2(d) shows a typical laser-based shoe-floor contour measurement during normal human walking gait.

Using a 3D printer, we fabricated a thin solid layer (the thickness of 0.5mm) with a set of black dots and transparent surrounding material. This thin solid layer is then glued to the bottom of the shoe; see Fig. 2.1. Two types of black dot arrays are used: one set of square-shape dots with a size of 3 mm are used for calculating the deformation and then slip distribution, and a set of 25 diamond-shape dots with a size of 6 mm are used as the landmarks to localize the small dots in the image processing algorithms. To obtain the contact contour and to compute the deformation and slip distributions, we designed and implemented a vision-based processing algorithms similar to the one in [47]. Figure 2.2(d) shows the detected small dots (blue square marks) and landmarks (red diamond marks) of a footprint snapshot during human walking gait.

The data collection among the optical motion capture, the forces and the force distributions, and the vision-based contact contour measurements are synchronized through the analog signal triggering connections among CompactRIO, the Vicon computer and the data acquisition computer. The sampling frequency for all the sensors is 100 Hz.

2.3 Shoe sole-floor contact forces models

The sole-floor friction forces heavily depend on the normal force distribution between the shoe and the floor. The flexible PSECR sensor array measures the normal forces at various locations. In this sections, we first present a model for the sole-floor normal

pressure distribution for the given PSECR sensor measurements and then a computational model for the friction forces calculation.

2.3.1 Normal contact forces model

Figure 2.3 illustrates the configuration for the contact forces modeling. The shoe-floor contact patch is denoted as $\mathcal{C}$. A sole-floor contact frame $\mathcal{B}(x, y, z)$ is attached to $\mathcal{C}$ with the origin at the rear tip location C_1 with the y-axis tangent to $\mathcal{C}$ and the x-axis pointing forward. The x-axis intersects $\mathcal{C}$ at point C_2; see Fig. 2.3. We denote the left portion $\widehat{C_1 C_+ C_2}$ of contour $\mathcal{C}$ as function $y_+(x)$ and right portion $\widehat{C_1 C_- C_2}$ as function $y_-(x)$. For point $P(x, y)$ on $\mathcal{C}$, we denote the three-directional forces as $f_x(x, y)$, $f_y(x, y)$ and $f_n(x, y)$, respectively.
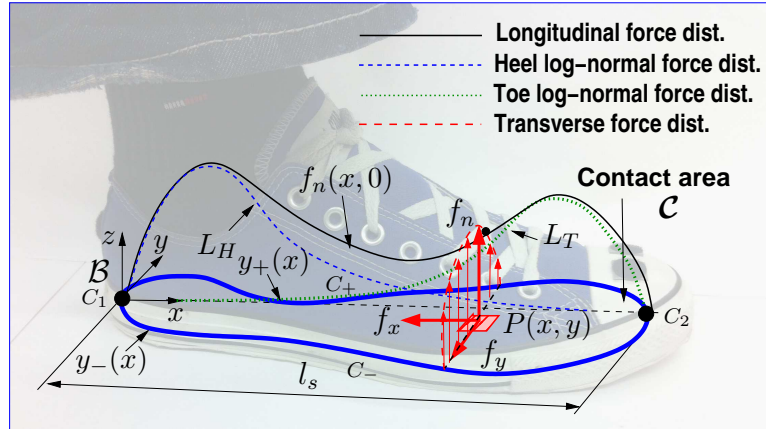
Figure 2.3: A schematic of the shoe-floor contact and force distributions.

We take a decomposition approach to obtain the model for $f_n(x, y)$. The form of $f_n(x, y)$ is expressed as the product of the longitudinal normal load $f_{nx}(x)$ and the lateral force factor $f_{ny}(x, y)$. For any $0 \leq x \leq l_s$, $y_-(x) \leq y \leq y_+(x)$, where l_s is the maximum x-coordinate of the front tip point of $\mathcal{C}$, we obtain

$$f_n(x, y) = f_{nx}(x) f_{ny}(x, y). \tag{2.1}$$

The form of $f_{nx}(x)$ consists of the contributions from the heel (H) part and the toe (T)

part, which are constructed as the sum of two log-normal probability density distribution-like pressure functions, namely,

$$f_{nx}(x) = [s_H L_H(x; \mu_H, \sigma_H) + s_T L_T(l_s - x; \mu_T, \sigma_T)], \tag{2.2}$$

where $L_i(x; \mu_i, \sigma_i) = \frac{1}{x_i \sigma_i \sqrt{2\pi}} \exp\left(-\frac{(\ln x_i - \mu_i)^2}{2\sigma_i^2}\right)$, $i = H, T$, is the log-normal distribution density function. Coefficients s_H and s_T are the scaling factors for the heel and toe log-normal force distributions, respectively. The normalized lateral force factor $f_{ny}(x, y)$ is constructed by using the Legendre polynomials. In the following, we first discuss how to determine $f_{ny}(x, y)$ and then present how to determine the model parameters for $f_{nx}(x)$.
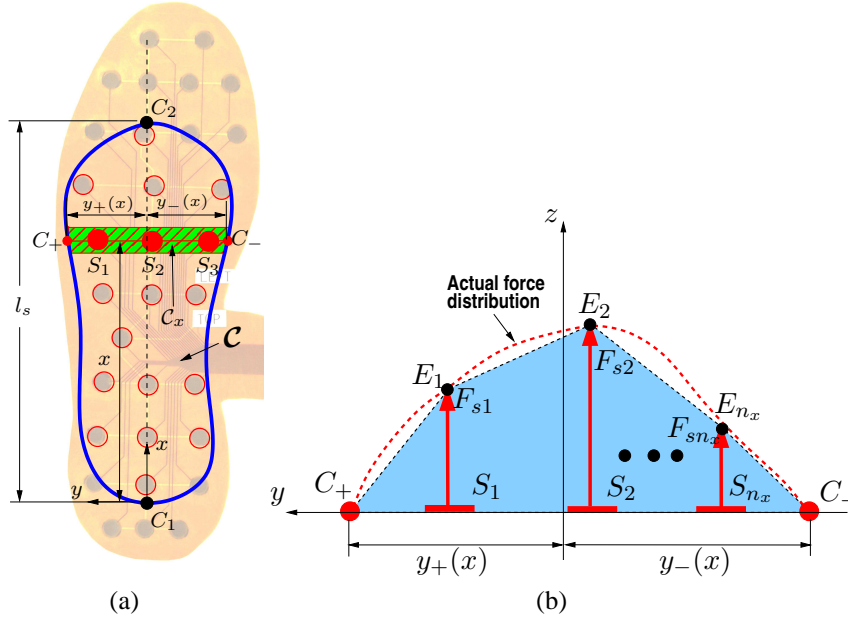
Figure 2.4: Schematic of the lateral force distribution calculation. (a) Flexible PSECR sensor array and calculation configuration. (b) Cross-section view of the normal force measurements along section $\mathcal{C}_x$.

For a given x, factor $f_{ny}(x, y)$ models the normal force distribution on a transverse area $\mathcal{C}_x$, shown as the shaded area in Fig. 2.4(a). Within $\mathcal{C}_x$, there are n_x PSECR sensor units, denoted as S_j and located at (x, y_{sj}), with normal force measurements as F_{sj}, $j = 1, \cdots, n_x$, respectively. For example, in Fig. 2.4(a), $n_x = 3$. We denote the boundary points of $\mathcal{C}_x$ with $y_+(x)$ and $y_-(x)$ as C_+ and C_-, respectively. To construct

the shape of the actual normal force along the y-axis with finite measurements as shown in Fig. 2.4(b), we consider $f_{ny}(x, y)$ as a linear combination of a series of Legendre polynomials up to the 5th-order, namely,

$$f_{ny}(x, y) = \sum_{i=0}^{5} a_i P_i(u), \quad u(y) = -1 + 2\frac{y(x) - y_-(x)}{y_+(x) - y_-(x)}, \qquad (2.3)$$

where a_i are the coefficients that will be determined later in this section and $P_i(u)$, $u \in [-1, 1]$, are the ith-order Legendre polynomial [99]. The use of the 5th-order Legendre polynomials in (2.3) is primarily due to its sufficiency to approximate the shape of the normal force. Note that the mapping $y \mapsto u$ changes the variable from $y_-(x) \le y \le y_+(x)$ to $-1 \le u \le 1$ for a given x. From the property of Legendre polynomials, from (2.3) we immediately obtain

$$\int_{y_-(x)}^{y_+(x)} f_{ny}(x, y)dy = \frac{y_+(x) - y_-(x)}{2} \int_{-1}^{1} \sum_{i=0}^{5} a_i P_i(u)du = \frac{a_0}{K}, \qquad (2.4)$$

where $K = \frac{1}{y_+(x) - y_-(x)}$.

We construct an algorithm to estimate coefficients a_i, $i = 0, \cdots, 5$. As shown in Fig. 2.4(b), for the given sensor measurements F_{sj}, $j = 1, \cdots, n_x$, we normalize F_{sj}s by the total area C_x of polygon $C_+ E_1 E_2 E_{n_x} C_-$ and factor K, and then these normalized forces are equal to the values given by (2.3) at (x, y_{sj}), namely,

$$f_j = \frac{F_{sj}}{S_x K} = \sum_{i=0}^{5} a_i P_i(u_j), \quad u_j = u(y_{sj}), \quad j = 1, \cdots, n_x. \qquad (2.5)$$

For boundary points C_+ and C_-, the normal forces are both zero and we obtain $0 = \sum_{i=0}^{5} a_i P_i(1) = \sum_{i=0}^{5} a_i P_i(-1)$. Since $f_{ny}(x, y)$ is a normalized force factor, in the above integral equation (2.4), we assign $a_0 = 1$ to simplify the calculation. The above relationships for known forces at sensors locations give us a total of $(n_x + 2)$ equations to obtain coefficients a_i, $i = 1, \cdots, 5$. Notice that for the flexible PSECR sensor arrays as shown in Fig. 2.4(a), $n_x = 1, 2, 3$, or 4. Comparing with the sampling rate for the flexible force sensor array, the shape of the lateral normal force distributions change

slowly over time in stance. Therefore, the estimates of parameters a_i can be obtained through a least square method by using the PSECR flexible sensor measurements.

For the longitudinal normal force load parameters μ_i and σ_i, $i = H, T$, we take the x-coordinate at the maximum peak value of normal force for μ_H (μ_T) and calculate μ_T (μ_H) by relationship $\mu_H + \mu_T = l_s$. We treat $\sigma_H = \sigma_T$ as a constant during the entire stance and estimate its value by the PSECR flexible sensor measurements. The values for scaling factors s_H and s_T are estimated directly from the smart shoe sensor outputs of the 6-DOF force plates under the heel and forefoot.

The use of the Legendre polynomial-based approximation for $f_{ny}(x, y)$ and the log-normal distribution function for $f_{nx}(x)$ have several advantages. The main advantage for the $f_{ny}(x, y)$ model is that for any given x, the integration of $f_{ny}(x, y)$ over y is always equal to 1. This is due to the properties of the Legendre polynomials and their properties when $a_0 = 1$. Therefore, the higher-order Legendre coefficients a_is can be tuned online to capture models for various transverse pressure distributions for different gait patterns (such as supination or pronation) without changing the total force values. Moreover, the integration of $L_i(x; \mu_i, \sigma_i)$ over a large range of x is also approximated to 1 and thus, the scaling factors s_H and s_T are exactly approximated as the normal forces measured by the heel and toe smart shoe sensors, respectively. Besides a compact form with a few model parameters, the log-normal distribution offers the advantage of specifying the location of the peak and the width of the peak for the pressure distribution along the x-axis. This property is directly used to tune the model parameters with measurements from the distributed flexible PSECR sensors and the smart shoe's 6-DOF heel and toe sensors.

2.3.2   Friction contact forces model

Since it is difficult to obtain a closed-form formulation, we take a computational approach to obtain the slip and friction force distributions between the sole and the floor

surface. Similar to the approach described in [33], a beam-spring network approach is used to compute the local deformation and the friction force distributions simultaneously. There are several differences compared to the previous modeling approach in [33]. The first difference is that the contact area has irregular shape and its size is constantly changing with time. Another difference with [33] is that the boundary force is no longer distributed across the boundary of the contact patch such as in tire-road interaction, but it is uniformly distributed across the entire contact due to the solid shoe sole configuration.

Figure 2.5 illustrates the beam-spring network modeling approach. The shoe-floor contact patch $\mathcal{C}$ is partitioned into N virtual cantilever beams and each of them has a height of h (sole layer thickness) and a square cross-section with dimension $c \times c$, where c is the side length. Virtual linear springs connect each pair of neighboring beams. We assume that for each beam, elongation and compression are ignored and only the bending deformation is considered.
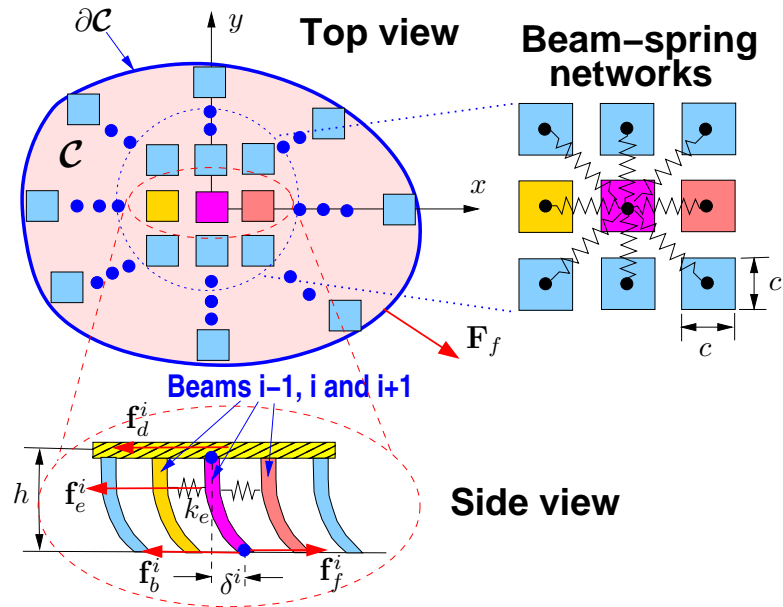
Figure 2.5: A schematic of the hybrid beam-spring network model to capture the shoe sole-floor stick-slip interaction.

Since we focus on studying the initiation of the sole slip, stick-to-slip transition

between the shoe and the floor is of the interests here. Our assumption is that the boundary friction force is evenly distributed across the entire contact patch, due to the beams being rigidly connected to the rigid top surface. Thus, the dynamic motions of the beams are negligible. For the ith beam, $i = 1, \cdots, N$, the following force balance relationship is obtained.

$$\mathbf{f}_f^i + \mathbf{f}_b^i + \mathbf{f}_e^i + \mathbf{f}_d^i = 0, \qquad (2.6)$$

where $\mathbf{f}_f^i = [f_x^i \ f_y^i]^T$ is the contact friction force, $\mathbf{f}_d^i$ is the evenly distributed boundary friction force applied at the top of all of the beams, $\mathbf{f}_b^i$ is the bending force that captures the shear deformation, and $\mathbf{f}_e^i$ is the resultant net elastic force from the connected springs; see Fig. 2.5. The resultant elastic force $\mathbf{f}_e^i$ is calculated as

$$\mathbf{f}_e^i \ = \ \sum_{j \in \mathcal{N}_i} \mathbf{f}_e^{ij} = \sum_{j \in \mathcal{N}_i} k_e \Delta \mathbf{u}_{ij} = Eh \sum_{j \in \mathcal{N}_i} \Delta \mathbf{u}_{ij}, \qquad (2.7)$$

where $\mathbf{f}_e^{ij} = k_e \Delta \mathbf{u}_{ij}$ is the spring (elastic) force between the ith beam with its neighboring jth beam, $k_e = Eh$ is the spring stiffness coefficient, and $\mathcal{N}_i$ is the index set of all the neighboring beams of the ith beam. Spring deformation is calculated as $\Delta \mathbf{u}_{ij} = (\mathbf{u}_j - \mathbf{u}_i)\left(1 - \|\mathbf{u}_{j0} - \mathbf{u}_{i0}\| / \|\mathbf{u}_j - \mathbf{u}_i\|\right)$ between the ith and jth beams, where $\mathbf{u}_i$ and $\mathbf{u}_j$ are the position vectors for the ith and jth beams, respectively, and $\mathbf{u}_{i0}$ and $\mathbf{u}_{j0}$ are respectively the original position vectors of the ith and jth beams without deformation.

The virtual cantilever beams are bent under friction force. The tip bending deformation δ_k^i of the ith beam along the k-axis is approximated by

$$\delta_k^i = \frac{f_n^i}{f_n^{ave}} \frac{3\mu F_z}{16 L_k} \frac{2 - \nu}{G} \left[1 - (1 - \psi_k)^{2/3}\right], \ k = x, y, \qquad (2.8)$$

where μ is the friction coefficient, L_k is the maximum length of the contact contour in k-axis direction, f_n^i is the local normal pressure at the ith beam's location, f_n^{ave} is the average normal pressure of $\mathcal{C}$, $\psi_k = \frac{F_k}{\mu F_z}$ is the ratio of the total friction force in the k-axis direction with the total normal force F_z times friction coefficient μ. The bending

force of the ith beam is obtained as

$$\mathbf{f}_b^i = k_b \boldsymbol{\delta}^i = \frac{3EI}{(h)^3} \boldsymbol{\delta}^i, \tag{2.9}$$

where $\boldsymbol{\delta}^i = [\delta_x^i \ \delta_y^i]^T$ is the tip deflection vector of the ith beam and $k_b = \frac{3EI}{(h)^3}$ is the bending stiffness of the beam. Compared to the definition of the bending deformation δ_k^i in [33] in our algorithm L_k represents the maximum length of the contact contour in k-axis direction.

The Coulomb friction model is adopted to compute $\mathbf{f}_f^i$. If $|\mathbf{f}_b^i + \mathbf{f}_e^i| < \mu f_z^i$, where $f_z^i = f_n^i c^2$ is the normal force at the tip of the ith beam, the beam is stuck and has no movement. In this case, $\mathbf{f}_f^i$ balances the resultant force of $\mathbf{f_b^i}$, $\mathbf{f_d^i}$ and $\mathbf{f_e^i}$. If $|\mathbf{f}_b^i + \mathbf{f}_d^i + \mathbf{f}_e^i| \geq \mu f_z^i$, $|\mathbf{f}_f^i| = \mu f_z^i$ cannot fully sustain the resultant of $\mathbf{f}_b^i$, $\mathbf{f_d^i}$ and $\mathbf{f}_e^i$. The beam will slip until the force equilibrium holds again at the new location. $\mathbf{f}_b^i$ is assumed to be saturated when the ith beam slips.

To compute the summation of forces on the contact patch we consider the fact that the spring forces $\mathbf{f}_e^i$s are internal forces and their summation is zero $\mathbf{F}_e = \sum_{i=1}^{N} \mathbf{f}_e^i = \mathbf{0}$.

Therefore the total bending force $\mathbf{F}_b$ and friction force $\mathbf{F}_f$ are defined as

$$\mathbf{F}_b = \sum_{i=1}^{N} \mathbf{f}_b^i \text{ and } \mathbf{F}_f = \sum_{i=1}^{N} \mathbf{f}_f^i, \tag{2.10}$$

By adding together all N equations of 2.6 and using the above definition the total boundary force $\mathbf{F}_d = \sum_i^{N} \mathbf{f}_d^i$ is obtained as

$$\mathbf{F}_d = -\mathbf{F}_b - \mathbf{F}_f. \tag{2.11}$$

With the above formulation, a computational algorithm is used to obtain deformation distribution $\mathbf{u}$ and friction force $\mathbf{f}_f$ on $\mathcal{C}$ simultaneously. For completeness of the modeling description, we present the Algorithm 1 used in our calculation that is modified from the original in [33].

Algorithm 1: Shoe-floor stick-slip evolution numerical calculation for slip prediction.

---

1 Initialize: Set normal force f_z^i and original position $\mathbf{u}^i$ for all N beams. Define $\mathbf{A} \in \mathbb{R}^N$ and set $\mathbf{A}(i) = 1$, $\mathbf{F}_f \leftarrow 0$, $\mathbf{f}_b^i \leftarrow 0$, $\mathbf{f}_e^i \leftarrow 0$, $\mathbf{f}_f^i \leftarrow 0$, $i = 1, \cdots, N$;

2 **while A $\neq$ 0 do**

3     $\mathbf{F}_f \leftarrow \mathbf{F}_f + \Delta\mathbf{F}_f$;

4   Update $\mathbf{f}_b^i$ and $\mathbf{F}_b$ by (2.9) and (2.10);

5     $\mathbf{F}_d \leftarrow -\mathbf{F}_f - \mathbf{F}_b$, update $\mathbf{f}_d^i = \mathbf{F}_d/N$;

6   Set iteration error indicator $Err \leftarrow 1$;

7   **while** $Err > E_{thresh}$ **do**

8        $Err \leftarrow 0$;

9   **for** $i = 1$ *to* N **do**

10   Find $\mathcal{N}_i$ and update $\mathbf{f}_e^i$ by (2.7);

11   **if** $\mathbf{A}(i) = 1$ **then**

12   **if** $\|\mathbf{f}_e^i + \mathbf{f}_b^i + \mathbf{f}_d^i\| < \mu f_z^i$ **then**

13                 $\mathbf{f}_f^i \leftarrow -\mathbf{f}_e^i - \mathbf{f}_b^i - \mathbf{f}_d^i$, $\Delta\mathbf{u}^i \leftarrow 0$;

             else

14                 $\mathbf{A}(i) \leftarrow 0$, go to Line 9;

             end

          else

15              $\mathbf{f}_f^i \leftarrow \mu f_z^i \frac{\mathbf{f}_e^i + \mathbf{f}_b^i + \mathbf{f}_d^i}{\|\mathbf{f}_e^i + \mathbf{f}_b^i + \mathbf{f}_d^i\|}$, $\Delta\mathbf{u}^i \leftarrow \frac{\eta}{6Eh}(\mathbf{f}_e^i + \mathbf{f}_b^i + \mathbf{f}_d^i - \mathbf{f}_f^i)$;

          end

16           $\mathbf{u}^i \leftarrow \mathbf{u}^i + \Delta\mathbf{u}^i$, $Err \leftarrow \max(Err, \|\Delta\mathbf{u}^i\|)$;

       end

    end

end

2.4 Experimental results

2.4.1 Experiments

We conducted human subject testing for both the normal human walking and slip and fall walking. Both types of the experiments were conducted on the walking platform as shown in Fig. 2.1. A healthy young man was recruited to conduct the experiments. In the first test, the subject was asked to walk with his normal gait on the platform. In the second test, the subject was asked to repeat the test by walking on the platform with a reduced coefficient of friction at the acrylic plate. To achieve this sudden reduction

of coefficient of friction, a cloth was permanently placed on the platform surface at the position of one step ahead of the actual step on the acrylic plate and liquid soap was applied in a certain experiment runs, while the subject was distracted by giving him a unique tasks (such as lifting legs or similar) when facing away from the platform. There was no indication of learning or changes in the gait by the subject. The subject was informed that there is a possibility of foot slippage and fall. The subject was asked to walk on the platform to become familiar with the testing environment before actual experiments were conducted. Before conducting any experiments, the subject was informed with the consent form of the testing protocol approved by the Institutional Review Board (IRB) at Rutgers University.

The subject wore a special shoe with the smart shoes sensors inside and with the flexible force sensors embedded inside the sole. The smart shoe sensors provide the 3D total forces and the evolution of plantar sole-floor pressure distribution is obtained by using the flexible PSECR force sensors as shown in Fig. 2.1(b). Each individual flexible force sensor was calibrated by using a computer controlled linear stage to load each sensor up to 25 lbs with increments of 5 lbs. Force values were measured using a 6-DOF force/torque sensor (from JR3 Inc.). An embedded system (CompactRIO from National Instruments Inc.) was used to collect the data and control the motor. Figure 2.6(b) shows the performance of three calibrated sensors and these sensors measure the actual normal pressure forces accurately. The reading from the flexible force sensors was fitted using third order polynomial to match the actual normal force within 5%.

2.4.2   Normal walking gait results

The evolution of the contact footprint during the subject's normal walking gait is shown in Fig. 2.8. A sequence of the contact evolution for the left foot from 10% to 90% stances at non-equal intervals are shown in the figure, where stance (S) is defined as a

(a)   (b)
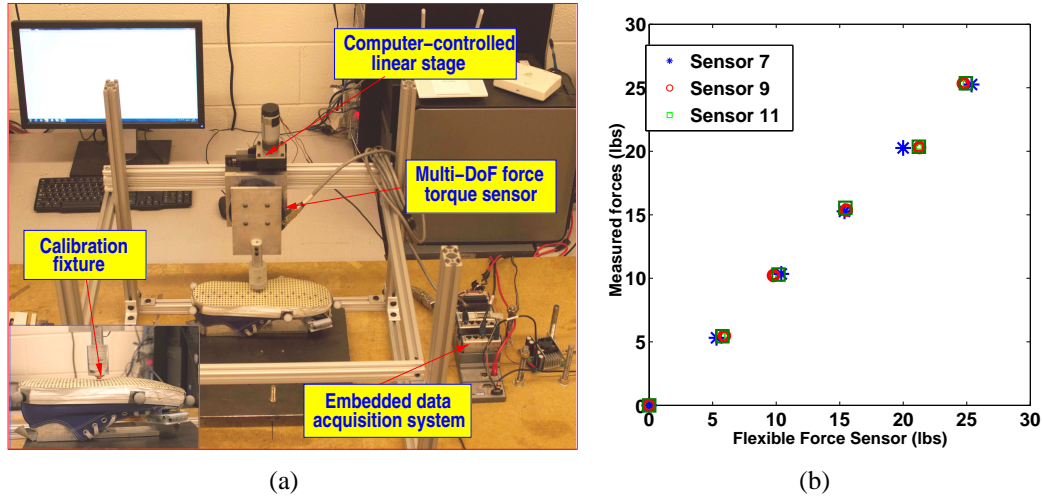
Figure 2.6: (a) Experimental setup for calibrating the flexible force sensor array. (b) Flexible force sensor measurement results.

(a)   (b)   (c)

(d)   (e)
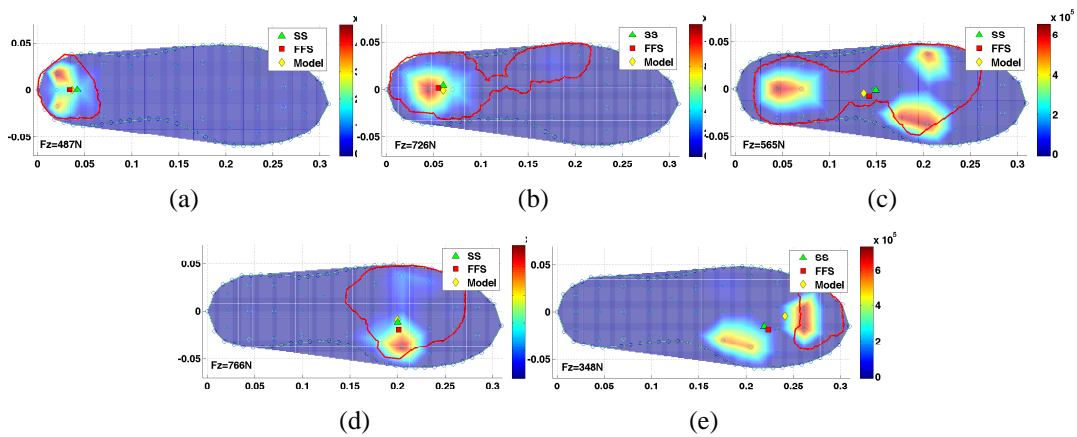
Figure 2.7: Pressure distribution with the contact contour and COP calculated from the smart shoes and the flexible force sensors at (a) 10% of the stance, (b) 25% of the stance, (c) 50% of the stance, (d) 75% of the stance and (e) 90% of the stance during normal human walking gait.

portion of the gait of a single step beginning with the heel strike (0%) and ending with the toe-off (100%). The pressure distribution obtained from the flexible force sensors and the contact contour during same time instances are presented in Fig. 2.7.

To demonstrate the validity of the normal force model, we compare the calculated center of pressure (COP) trajectory during the normal walking gait with the COP calculations by the flexible PSECR arrays and the smart shoe sensors. Figure 2.9 shows
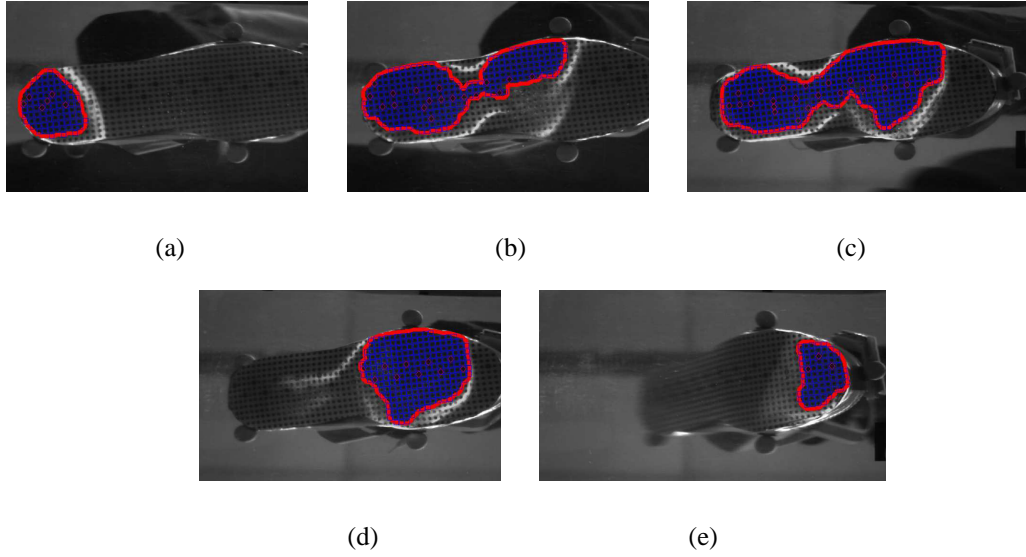
Figure 2.8: Evolution of the laser-based contact contour and detected dots inside the contour at (a) 10% of the stance, (b) 25% of the stance, (c) 50% of the stance, (d) 75% of the stance and (e) 90% of the stance during subject's normal walking gait.

the comparison results. Figures 2.9(a) and 2.9(b) demonstrate the x and y positions of the COP as a function of the percentage of the stance S, while Fig. 2.9(c) shows the x-y trajectory of the COP by measurements from various sensors. To evaluate the influence of the presence of smart shoes sensors on the pressure distribution, we also conduct the comparison experiments by removing the smart shoe sensors (both the heel and toe sensors) and only use the flexible force sensor array. As clearly shown in Fig. 2.9, the flexible force sensor measurements do not show any significant difference between the experiments with and without the smart shoe sensors inside. This implies that putting the force sensors inside the shoes does not change the normal gait pressure distribution. From the results shown in the figure, the COP predictions by the proposed normal force model match well with the calculations from both the flexible force sensor array and the smart shoe sensors. These results confirm the effectiveness of the normal force model.

In Fig. 2.9(c), we omitted data for the first and last 5% of the stance because of low
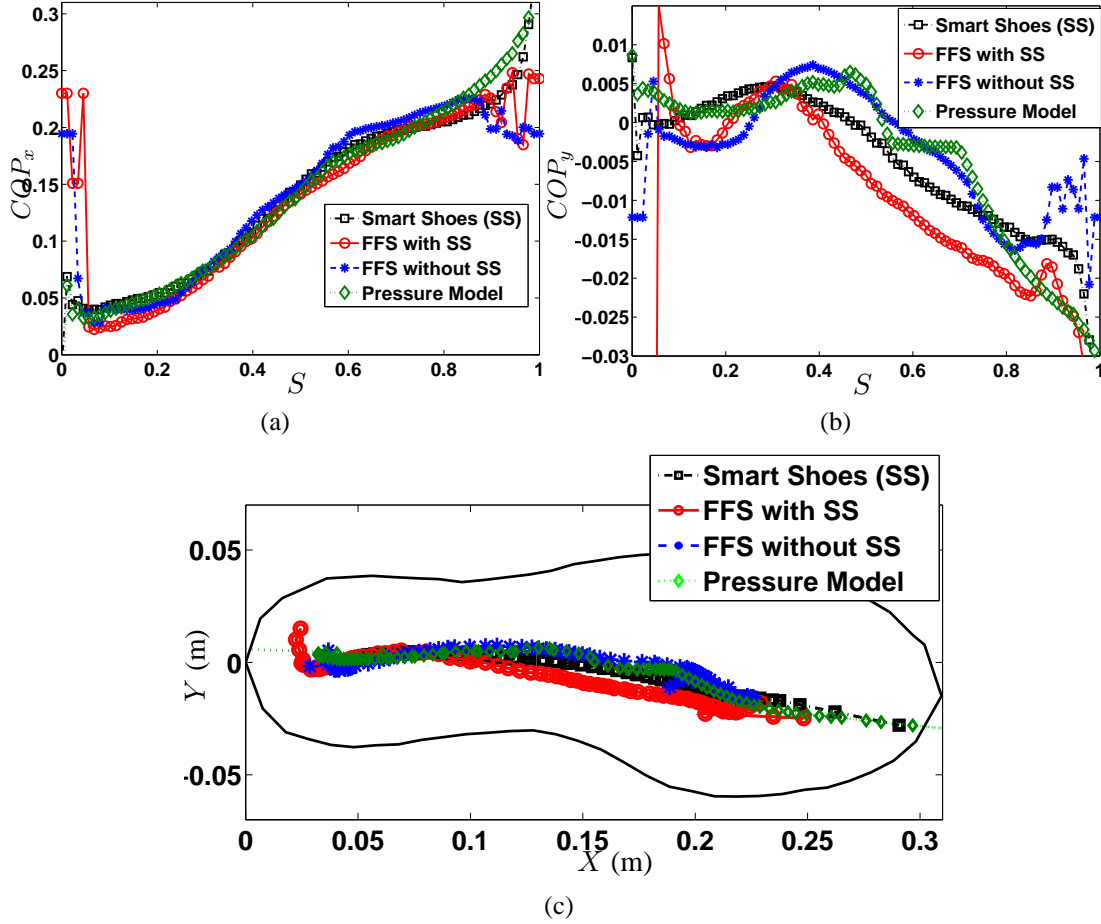
Figure 2.9: Comparison results of the COP trajectory during the normal walking gait by various sensor measurements and the normal force model. (a) Evolution of the COP in the x-axis direction vs. the percentage of stance. (b) Evolution of the COP in the y-axis direction vs. the percentage of stance. (c) The COP trajectory comparisons in the shoe frame.

accuracy of the sensor initialization and foot contact impacts on the sensor measurements. The differences of the COP positions in the y-axis direction (Fig. 2.9(b)) among various sensor measurements could be possibly due to the non-perfect foot-insert that was placed under the smart shoe sensors to emulate the anatomy of the foot and the decreased sensitivity of some flexible force sensors at certain locations. An example of such incorrect sensor reading can be observed in Fig. 2.8(e).

During normal walking when slip does not occur, the deformation of the sole was detected mainly at the contact boundary. The values of the RCOF calculated from

the smart shoe sensors shown in Fig. 2.10(a) also confirm that no global slip happens because the measured dry sole-floor coefficient of friction (around 0.8-1 in Table 2.1) is typically larger than RCOF. Figure 2.11 shows the deformation at various percentages of stance using the camera-based measurements. The deformation inside the contour is fairly small and without any significant trend. Most significant deformations happen mainly at the front and rear portion of $\mathcal{C}$.
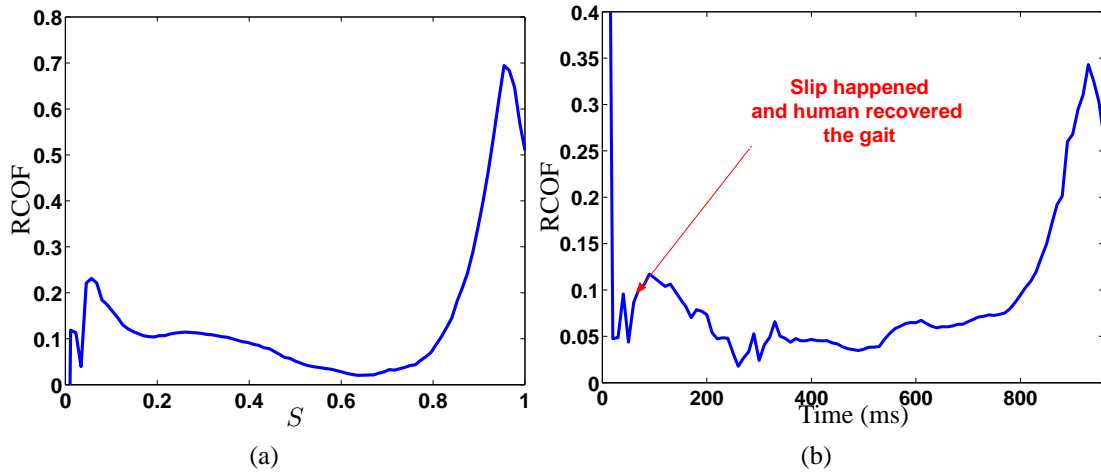
Figure 2.10: Results of the RCOF computed from the smart shoe force measurements (a) during normal walking and plotted with respect to the stance S, (b) during walking with foot slip and plotted with respect to time.
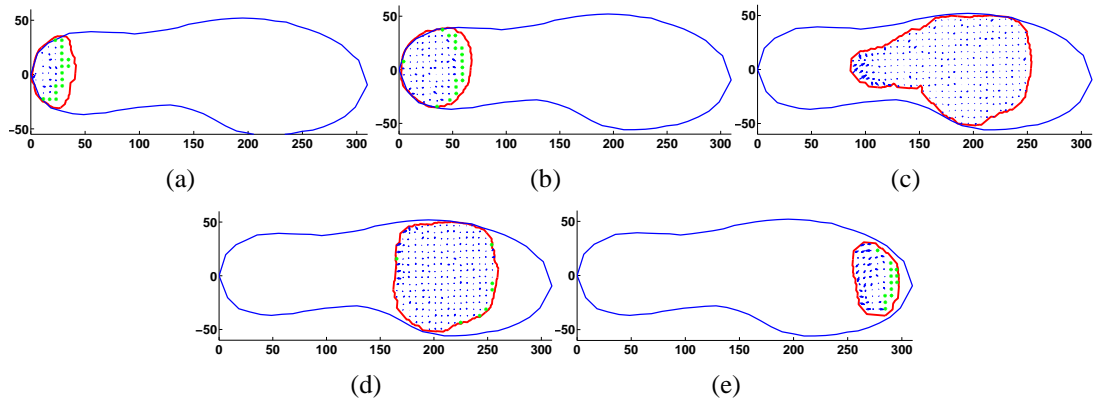
Figure 2.11: Deformations inside $\mathcal{C}$. (a) Mainly at the front edge of $\mathcal{C}$ at 8% of S. (b) Deformation at the front edge of $\mathcal{C}$ due to the bending of the sole at 12% of S. (c) Deformation at the rear edge of $\mathcal{C}$ due to the "rolling" of the shoe over the ground at 78% of S. d) Mainly at the front and rear edge of $\mathcal{C}$ due to the "rolling" effect at 84% of S. (e) At the push-off phase at 94% of S. All deformations are magnified by 20 times.

At the beginning of the stance (up to 8-10%) the main deformation is located at

the front part of the contact (Fig. 2.11(a)). At this initial stage, the shoe is pushed forward. The longitudinal friction force is acting in the direction towards the toes and deformation or local slip happens at the front part of $\mathcal{C}$ where the normal load is small. Since the stick area is relatively small and the front portion has a local slip, this is one of the most crucial phases at which slip could occur. The slip experiments presented in the next section confirm such observation.

After the initial contact is established, the flat portion of the sole comes into contact with the ground. Due to the bending effect of the sole, the deformation at the front edge of $\mathcal{C}$ points towards inside its center. The deformation due to bending is observed only after the initial contact (around 10% of S) and lasts until approximately 25% of the stance when the entire flat part of the sole is in contact with the floor; see Fig. 2.11(b). At the mid-stance, no significant local deformation or change of the contact contour is observed. During the heel-off phase, the shoe is rolling over the front curved portion. Rear edge of $\mathcal{C}$ starts to move up and forward. This is observed by the deformation at the rear edge pointing towards the center of $\mathcal{C}$ starting at approximately 50% of the stance on-wards. Figure 2.11(c) illustrates the deformations at each side of the rear edge of $\mathcal{C}$ point towards the center line of the shoe. At the last stage of the push-off, deformation was observed due to the twist around z-axis and can be observed in Figs. 2.11(d) and 2.11(e).

2.4.3   Slip and fall gait results

The slip and fall was created at the beginning of the stance. Figure 2.12 shows the results of the measured deformation from the initial contact to the point when slip starts. The initial slip starts at approximately 8% of the stance. After the first few frames of images, it is observed that the dots at the rear have almost no deformation compared to the dots at the front edge of the contact contour; see Fig. 2.12(a). Similar behavior is observed during walking without slip. Gradually, the rear portion starts

to slip (Fig. 2.12(b)). Finally, at around 70 ms after heel impact, an instantaneous slip occurs over the entire contact contour, with all the dots having the same size and direction of the deformation as shown in Fig. 2.12(c).
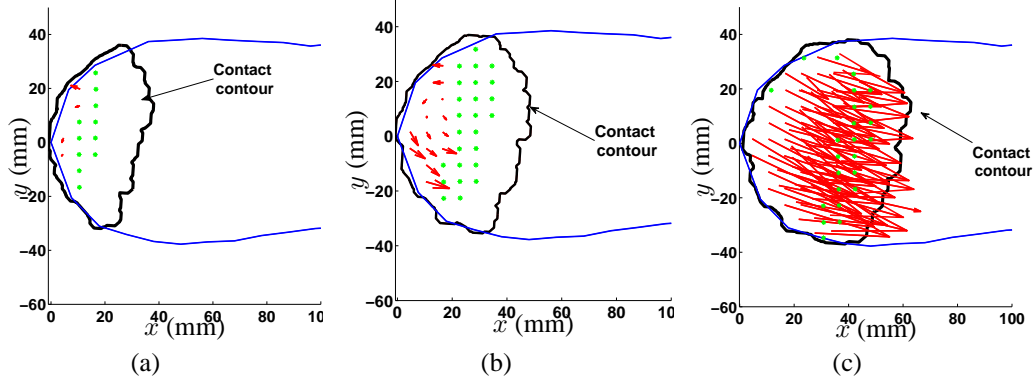
Figure 2.12: Measured deformations from initial contact to the detected slip at (a) 50 ms, (b) 60 ms and (c) 70 ms after beginning of stance. The slip happens at 70 ms. All deformations are magnified by 20 times.

During all of the slip tests, the subject was able to recover from slip and fall and continue walking. Figure 2.10(b) shows the calculated RCOF for the whole step with foot slip. We plot the RCOF as a function of time instead of stance since the duration of the step takes a longer time than that of a normal walking step (approximately 0.85 sec). Clearly, at the moment of 70 msec, the slip occurs and the RCOF is around the available sole-floor COF that is around 0.1 for the wet soap condition on the floor surface as shown in Table 2.1.

Table 2.1: Model parameters for the shoe-floor force models.

h	μ	σ_{Heel}	$\mu_{DryStat}$	μ_{DryDyn}	$\mu_{SoapStat}$	$\mu_{SoapDyn}$
0.005	0.1	0.4	1.05	0.75	0.55	0.1

We use the beam-spring model discussed in the previous section to compute the deformation evolution for the slip experiments. The normal force distribution model developed in Section 2.3 is used in the deformation computation. To use the computational model, the coefficient of friction between the shoe sole and the acrylic plate is
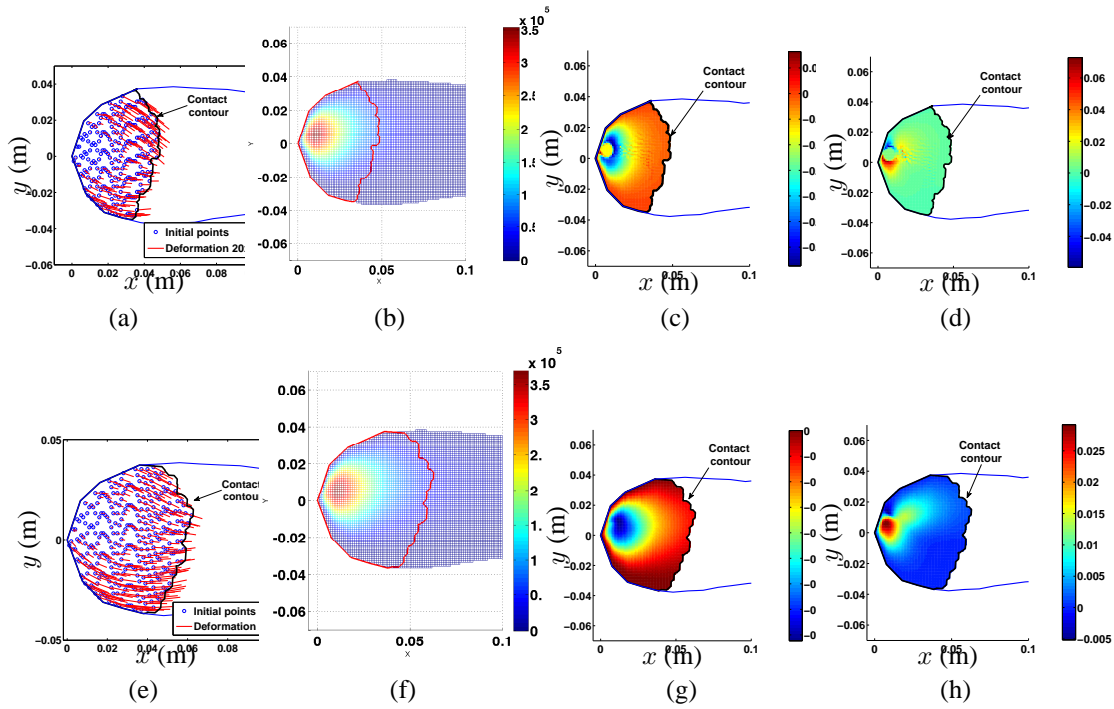
Figure 2.13: Results right before slip occurs. (a) Computed deformation distribution. (b) Measured normal load $f_n(x, y)$. (c) Computed longitudinal friction force distribution $f_x(x, y)$. (d) Computed lateral friction force distribution $f_y(x, y)$. Results right after slip occurs. (e) Computed deformation distribution. (f) Measured normal load $f_n(x, y)$. (g) Computed longitudinal friction force distribution $f_x(x, y)$. (h) Computed lateral friction force distribution $f_y(x, y)$.

needed. We obtained and estimated the shoe-acrylic plate friction coefficient through experiments that are similar to the walking gait. Measured coefficients of friction under various conditions are listed in Table 2.1. We compute the sole deformation and sole-floor friction distributions before (Fig. 2.13(a)) and after (2.13(e)) the slip happens. The results demonstrate that the large deformations and slip start at the front edge of the contact area, similar to the observed experimental results. The areas with the large normal load slips the last.

The computed longitudinal and lateral friction force distributions are shown in Figs. 2.13(c), 2.13(d) (before slip) and 2.13(g), 2.13(h) (slip occurred), respectively. We also plot the measured normal force distributions before and after slip as shown in Fig. 2.13(b) and 2.13(f), respectively. At the time instance right before foot slip,

the friction forces have the highest values in the neighborhood around the stick portion of the contact area. The lateral friction force distribution shows the large values, but different signs, around the stick contact area (Fig. 2.13(d)). The opposite signs indicate compression and tension in these areas. Friction forces show a smaller value inside the stick region than those in its neighborhood area. This could be due to the large contribution of elastic forces in non-stick areas and also possibly due to the use of Coulomb friction law in the computational framework. At the instance of slip, both the longitudinal and lateral forces show a high correlation with the normal load distribution and have peak values at the same areas.

Due to small contact area and the high stiffness of the sole material, the sole-floor interaction is like a rigid contact and thus, the resultant RCOF calculation seems to serve as a good prediction of slip occurrence. The sole deformation could also serve as a good indicator for possible slip, especially when the actual coefficient of friction is either unknown or is difficult to obtain it in real time. Using sole deformation as a slip predictor complements the current reported RCOF indicator and could be used as a true assessment for slip occurrence. One advantage of using deformations for slip indicator is that no prior knowledge of the true sole-floor coefficient of friction is needed. Of course, obtaining the deformation distribution in a real time is not straightforward and this is one of our future research directions.

2.5   Conclusion

In this chapter, we studied shoe-floor interactions during human normal and slip walking gaits. We measured plantar pressure distribution using flexible force sensors embedded inside the shoe sole as well as the resultant forces using two 6-DoF load-cells under the hindfoot and forefoot. A normal force distribution model was first built and then used to compute the sole deformation and friction force distributions. We validated the normal force distribution model through experiments and the results showed

good agreement by comparing the COP trajectory during the normal walking gaits. Computer vision-based sole deformation measurements were used to obtain slip distribution during the walking gaits. The experimental and computational results confirmed that the largest deformations occurred in the areas with the smallest normal load, where partial slips also happened first. Detection of slip occurrence using the deformation measurements was compared to that by using the RCOF calculation. The comparison results showed a good agreement. One advantage of using the deformation over the RCOF to predict slip occurrence is the qualitative assessment of slip, especially when the friction coefficient is unknown.

Chapter 3

Dynamic Model of Soft-Solid Interactions

3.1 Introduction

This chapter is an extension of a quasistatic model presented in Chapter 2. To character-ize the complex dynamic shoe-floor interactions for foot slip prediction, we developed a novel dynamic friction model that is integrated with the beam-spring network model to compute the deformation and friction force distribution in soft-solid contact.

Shoe sole-floor contact is an example of a soft-solid contact with friction forces generated on the contact patch. For soft-solid contact with a finite area between the soft materials and the rigid surface, the contact interaction forces are complicated [36, 37]. During foot slip, these interactions become even more complicated due to highly dy-namic foot slip and changing of the contact area, the normal load distribution and slid-ing velocity. Dynamic friction models seems a natural option to be used to capture the friction forces in the soft-solid contact under dynamically challenging conditions [100].

The dynamics friction models, such as LuGre model [101], have been used to cap-ture and interpret the total friction forces through rubber deformation distribution. The LuGre friction model uses the bristle deformation to capture the frictional forces be-tween two solid contacts [41] and has been used to interpret and calculate the *total* tire-road friction forces for a given normal force distribution [42–46]. In [33, 47, 48], a beam-spring network model is used to model the rubber deformation and the friction force distributions on the contact patch during the stick-to-slip transition. Embedded force sensors are used to validate the modeling results. However, only static contact is

considered in [33, 47] and no sliding or dynamic motion is assumed between the tire and the road interactions.

In this chapter, we integrate the LuGre friction model with the beam-spring network model to capture the dynamics of the soft-solid contact. The new scheme uses the LuGre friction model to calculate the frictional force properties such as Stribeck and time-dependent effects, while the beam-spring network model is used to describe the elastic characteristic of soft materials and its interactions with the solid. The use of the beam-spring network model not only provides a means to compute the deformation and force distributions in soft-solid contact, but also fits well with the LuGre friction model structure. The use of the LuGre friction model simplifies the friction force calculation such as the computation in dynamic motion [33, 37]. We validate and demonstrate the modeling scheme through the fingertip-like contact application and experiments.

3.2 LuGre/beam network model

Figure 3.1 shows two soft-solid contact examples. Figure 3.1(a) shows the tire-road contact example, while Fig. 3.1(b) shows the soft semi-spherical contact with a rigid flat surface contact example in fingertip contact applications. For both examples, the soft-solid contacts are through a contact patch and the interaction forces are through the soft materials deformation and interaction with the solid.

(a)   (b)
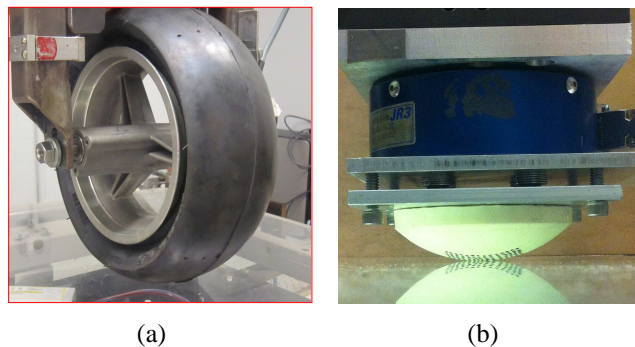
Figure 3.1: (a) Tire-road contact example [33]. (b) A fingertip contact example.

3.2.1 Beam-spring network model

To model the soft-solid interaction deformation and force distributions, we take a similar setup of the beam-spring networks in [33] as shown in Fig. 3.2. The soft-solid contact patch is denoted as $\mathcal{P}$. The contact is considered through N virtual beams and each of them has a height of h and a square cross section with side length a. All the beams are clamped and rigidly connected together at one end. For simplicity, we use the following assumptions: (1) for each beam, elongation and compression are ignored and only the bending deformation is considered; (2) all the beams are clamped at one end on the top layer and are connected with their neighboring beams at the bottom end with virtual linear springs; and (3) the mass of each beam is considered to be concentrated at the bottom tip.
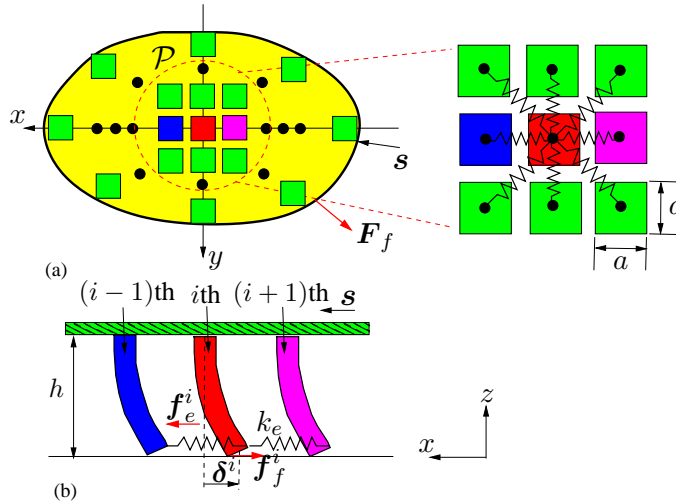
Figure 3.2: A schematic of the beam-spring network model for soft-solid contact. (a) Top view of the contact patch and the beams. (b) Side view of the three beams and their elastic connections.

The total friction force on $\mathcal{P}$ is denoted as $\boldsymbol{F}_f$. The total applied force on $\mathcal{P}$ is a resultant of the bending forces of all the beams and the elastic force among adjacent beams, denoted as $\boldsymbol{F}_b$ and $\boldsymbol{F}_e$, respectively. For the ith beam, one end is rigidly connected on the solid surface and defined with a position vector $\boldsymbol{s}_i$ in the inertial fixed

frame. The position of the free end of the beam is denoted as $\boldsymbol{u}_i = [u_x^i \ u_y^i]^T$ in the inertial frame, where u_x^i and u_y^i are the displacements along the x- and y-axis, respectively. Equation of motion for the ith beam is given by

$$m_i \ddot{\boldsymbol{u}}_i = \boldsymbol{f}_b^i + \boldsymbol{f}_e^i - \boldsymbol{f}_f^i, \tag{3.1}$$

where m_i is the mass of the beam, $\boldsymbol{f}_b^i$ and $\boldsymbol{f}_e^i$ are the bending and elastic force acting on ith beam, respectively, and $\boldsymbol{f}_f^i = [f_{fx}^i \ f_{fy}^i]^T$ is the friction force of the ith beam. The longitudinal and lateral friction forces f_{fx}^i and f_{fy}^i are along the x- and y-axis, respectively. In the following, we first describe how to calculate the bending and elastic forces $\boldsymbol{f}_b^i$ and $\boldsymbol{f}_e^i$ and then the friction force $\boldsymbol{f}_f^i$.

Let k_b^i denote the bending stiffness of the ith beam. Because of the large ratio of the beam height and cross section width, we cannot use the formulation in [33] to obtain k_b^i. Instead, we relate the estimation of k_b^i with the total stiffness of the soft material k_b as $k_b^i = \frac{k_b}{N}$, where N is the number of all the beams. We use $k_b = \frac{dF_f}{ds_x} = \Delta F_f / (\dot{s}_x \Delta t)$ to compute the total stiffness of the rubber layer.

For the ith beam, the absolute position $\boldsymbol{u}_i$ is obtained as the composite motion of the beams tip deformation $\boldsymbol{l}_i$ and the sliding motion of the other common end $\boldsymbol{s}_i$, namely,

$$\boldsymbol{u}_i = \boldsymbol{s}_i + \boldsymbol{l}_i, \tag{3.2}$$

where $\boldsymbol{l}_i = [l_x^i \ l_y^i]^T$ is the tip deflection vector of the ith beam. The bending force calculation of the ith beam for the hollow structure of a soft material can then be calculated as

$$\mathbf{f}_b^i = k_b^i \boldsymbol{l}_i, \tag{3.3}$$

Similar to [33], the elastic force is calculated as

$$\boldsymbol{f}_e^i = \sum_{j \in \mathcal{N}_i} \boldsymbol{f}_e^{ij} = \sum_{j \in \mathcal{N}_i} k_e \Delta \boldsymbol{u}_{ij} = Eh \sum_{j \in \mathcal{N}_i} \Delta \boldsymbol{u}_{ij} \tag{3.4}$$

where $\boldsymbol{f}_e^{ij} = k_e \triangle \boldsymbol{u}_{ij}$ is the spring (elastic) force between the ith beam and its neighboring jth beam, $k_e = Eh$ is the spring stiffness coefficient, and $\mathcal{N}_i$ is the index set of all the neighboring beams of the ith beam. $\triangle \boldsymbol{u}_{ij}$ is the spring deformation between the jth beam and ith beam

$$\triangle \boldsymbol{u}_{ij} = (\boldsymbol{u}_j - \boldsymbol{u}_i) \left(1 - \frac{u_{ij}^0}{\|\boldsymbol{u}_j - \boldsymbol{u}_i\|} \right) \tag{3.5}$$

where $\boldsymbol{u}_j$ and $\boldsymbol{u}_i$ are the position vector for the jth and ith beam, respectively, and $u_{ij}^0 = \|\boldsymbol{u}_{j0} - \boldsymbol{u}_{i0}\|$ is the length of the position vectors of the jth ($\boldsymbol{u}_{j0}$) and the ith ($\boldsymbol{u}_{i0}$) beams without spring deformation, that is,

$$u_{ij}^0 = \|\boldsymbol{u}_{j0} - \boldsymbol{u}_{i0}\| = \begin{cases} \sqrt{2}a & i \text{ and } j \text{ are diagonal} \\ a & \text{otherwise.} \end{cases} \tag{3.6}$$

In the soft-solid contact model, the known controlled variable is the velocity profile of $\dot{\boldsymbol{s}}_i$ for the computation. Knowing the absolute velocity $\dot{\boldsymbol{u}}_i$ of the free end of the beams, from (3.2) we compute the relative bending velocity $\dot{\boldsymbol{l}}_i$ as $-\dot{\boldsymbol{l}}_i = \dot{\boldsymbol{s}}_i - \dot{\boldsymbol{u}}_i$. Note that the bending velocity is negative due to the backwards bending direction.

3.2.2 Friction force calculation

Let $\boldsymbol{\delta}^i = [\delta_x^i \ \delta_y^i]^T$ denote the local deformation of the ith beam's tip, where δ_x^i and δ_y^i are the deformations along the x- and y-axis, respectively. To calculate the friction force $\boldsymbol{f}_f^i$, we use the LuGre friction model [100]. The LuGre friction model is built based on the interaction of microscopic contact bristles between two contact surfaces. The bristles dynamics are treated as an internal states and are related to the surfaces/bristle relative sliding velocity $\dot{\boldsymbol{u}}_i$. Compared to the LuGre model described in [41], we consider a finite number of bristles associated with an individual beam of the beam-spring network. For the ith beam, we use the two-dimensional (2D) LuGre

friction model as follows.

$$\dot{\delta}_k^i = \dot{u}_k^i - \hat{\sigma}_{0k}^i \frac{|\dot{u}_R^i|}{g_k(\dot{u}_R)} \delta_k^i \tag{3.7a}$$

$$f_{fk}^i = \sigma_{0k}^i \delta_k^i + \sigma_{1k}^i \dot{\delta}_k^i + \sigma_{2k}^i \dot{u}_k^i, \ k = x, y, \tag{3.7b}$$

where $\dot{\boldsymbol{u}}^i = [\dot{u}_x^i \ \dot{u}_y^i]^T$ is the relative sliding velocity of the free end of the ith beam with respect to the ground, $\dot{u}_x^i$ and $\dot{u}_y^i$ are the velocities along the x- and y-axis, respectively, $\dot{u}_R^i = \sqrt{(\dot{u}_x^i)^2 + (\dot{u}_y^i)^2}$ is the magnitude of the sliding velocity, and

$$g_k^i(\dot{u}_R^i) = \mu_k = \mu_{Ck} + (\mu_{Sk} - \mu_{Ck})e^{-(\dot{u}_R^i/v_s)^\alpha}, \ k = x, y, \tag{3.8}$$

captures the Stribeck friction effect [41]. μ_{Ck} and μ_{Sk} are respectively Coulomb (kinetic) and static friction coefficients along the k-axis, v_s is the Stribeck velocity and parameter α determines the shape of the function $g(\dot{u}_R)$ as a function of the ratio $|\dot{u}_R^i/v_s|$. In (3.7a), $\hat{\sigma}_{0k}^i = \sigma_{0k}^i/f_z^i$, $k = x, y$, where f_z^i is the normal load, σ_{0k}^i, σ_{1k}^i and σ_{2k}^i are the stiffness, micro-damping and viscous damping coefficients along the k-axis of the ith beam, respectively. These coefficients describe the contact properties at the soft-solid interaction, independently of the normal load distribution and/or material deformation. We define a simple relationship relating the lumped coefficients and the coefficient for the finite number bristles in contact through $\sigma_{jk}^i = \sigma_{jk}/N$, for $k = x, y$ and $j = 0, 1, 2$.

Note that the coupling effect of the longitudinal and lateral motions in (3.7) is captured by the term $\dot{u}_R^i$. It is straightforward to obtain that $\mu_{Ck} \leq g_k(\dot{u}_k) \leq \mu_{Sk}$, $k = x, y$. At steady state, the virtual cantilever beams reach a constant deformation and then the steady-state friction force $f_{fk,ss}^i$ is obtained as

$$f_{fk,ss}^i(\dot{u}_k) = f_z^i \frac{g_k(\dot{u}_k^i)\dot{u}_k^i}{\bar{\gamma}(\dot{u}_R^i, \mu)} + \sigma_{2k}^i \dot{u}_k^i, \ k = x, y. \tag{3.9}$$

3.3 Computation of the deformation and friction force distribution

In this section, we present a computational approach to obtain the contact deformation and friction force distributions for the soft-solid contact. Particularly, the existence of the stick-slip interactions plays an important role in the soft-solid contact and also increases the complexity of the computation.

Under the external force, the top end of the beams moves in the horizontal direction with position s_i and the bending force $\boldsymbol{f}_b^i$ (smaller than the static friction force) is balanced by the contact friction force $\boldsymbol{f}_f^i$ at the bottom of the ith beam. When the total external force is smaller than the total static friction force, the patch is under micro-motion, also called the zero-slip behavior [41]. While a portion of the contact patch of soft material still sticks to the solid material, the rest of the contact patch might start to slip. When the external force keeps increasing, the stick portion of $\mathcal{P}$ reduces and finally, when it is greater than the total static friction force, the entire patch starts slipping and sliding. Further increasing the displacement s_i results in high dynamic oscillating motion of the beams interchanging between stick ($\dot{\boldsymbol{u}}_i = 0$) and slip ($\dot{\boldsymbol{u}}_i \neq 0$) state, known as stick-slip motion [41].

To compute the deformation and friction force distributions during the initial stick-to-slip transition and the stick-slip oscillating motion, we assume that the entire contact patch is initially at rest and then gradually increasing $\boldsymbol{s}$. This results in a gradual increase of the total bending force $\boldsymbol{F}_b = \sum_{i=1}^{N} \boldsymbol{f}_b^i$ from zero to the value that is greater than the static friction force when the patch starts sliding motion. Using the LuGre/beam-network model, Algorithm 2 illustrates a computational procedure to obtain the deformation and friction force distributions under a given normal force distribution.

In the algorithm, we first define the current position and velocity $\boldsymbol{u}_i$ and $\dot{\boldsymbol{u}}_i$ for each beam, respectively, and zero friction force. The input to the model is the velocity

---

Algorithm 2: Numerical calculation of soft-solid contact.

---

1 Initialize: Set normal force f_z^i, velocity input $\dot{s}$ and top and bottom positions, s_i and u_i, for all N beams. Define $n \in \mathbb{N}$ and set $n \leftarrow 0$, $f_f^i(0) \leftarrow 0$, $f_b^i(0) \leftarrow 0$, $f_e^i(0) \leftarrow 0$, $\dot{u}_i(0) \leftarrow 0$, $l_i(0) \leftarrow 0$, $\delta_k^i(0) \leftarrow 0$, $i = 1, \cdots, N$;

2 **for** $n = 1$ *to* $N_{\max} = T_{\max}/\Delta t$ **do**

3   **for** $i = 1$ *to* N **do**

4   Find $\mathcal{N}_j$ and update $f_e^i(n)$ by (3.4);

5   Update $\dot{l}_i(n)$ by (3.2), $l_i(n+1) \leftarrow l_i(n) - \Delta t \dot{l}_i(n)$;

6   Update $f_b^i(n)$ by (3.3) and $\ddot{u}_i(n)$ by (3.1);

7          $\dot{u}_i(n+1) \leftarrow \dot{u}_i(n) + \Delta t \ddot{u}_i(n)$;

8          $u_i(n+1) \leftarrow u_i(n) + \frac{1}{2}\Delta t(\dot{u}_i(n+1) + \dot{u}_i(n))$;

9   Update $g_k^i(\dot{u}_R^i)$ by (3.8) and $\dot{\delta}_k^i(n)$ by (3.7a);

10         $\delta_i(n+1) \leftarrow \delta_i(n) + \Delta t \dot{\delta}_i(n)$;

11   Update $f_f^i(n)$ by (3.7b);

    end

end

---

profile $\dot{s}_i$ of the top end of the beams, where beams are rigidly connected. At each time step Δt, we first update the bending deformation rate $\dot{l}_i$ using the velocity of the free end of the beams $\dot{u}_i$ from the previous iteration. Using a forward Euler integration, we compute the bending deformation l_i. Then, the friction and elastic force distributions, f_f^i and f_e^i, are obtained by (3.3) and (3.4), respectively. We use same bending and elastic stiffness constants k_b^i and k_e^i for all the beams. Using the friction force f_f^i from the previous iteration, the acceleration $\ddot{u}_i$ is updated. A forward Euler integral method is employed to solve the motion dynamics (3.1). The velocity term $\dot{u}_i$ and the Stribeck friction function $g_k^i(\dot{u}_R^i)$ are used to compute the velocity $\dot{\delta}_i$, which is an internal state of the LuGre model and represents an internal bristle dynamics. Note that the normal load distribution is captured in (3.7a) by the term $\hat{\sigma}_{0k}^i$. We integrate velocity term $\dot{\delta}_i$ to compute the bristle deformation δ_i. Through the internal bristle dynamics with known bristle's stiffness σ_{0k}^i and micro-damping σ_{1k}^i coefficients as well as viscous friction coefficient σ_{2k}^i, we compute the distributed friction force of each beam and deformation distribution. Parameter $\sigma_{1k}^i = 2\sqrt{m\sigma_{0k}^i}$, $k = x, y$, is used when the system is critically

damped [41].

Considering beam's dynamics, the forward Euler integration and the beam's network elastic force calculation both require choosing sufficiently small time steps. Due to the involved beams and bristles dynamics, no convergence of elastic force by checking the u_i position error is assured in Algorithm 2 while the algorithm in the quasistatic case is guaranteed to be convergent in [33].

Remark 3.1. *The velocity based criterion cannot be used for detection of beams' stick or slip state. This is due to the nature of the LuGre bristle's dynamic model which allows microscopic displacements to build up the friction force [100]. In Algorithm 2, the stick or slip status for each beam is not explicitly defined. However, since the friction force is calculated and obtained, we can uniquely determine the stick or slip status according to the property of friction force characteristic. From (3.9), we know that $f_{fk}^i \leq f_z^i \mu_{Sk} =: f_{Sk}^i$, $k = x, y$. If $f_{fk}^i < f_{Ck}^i := f_z^i \mu_{Ck}$, then the ith beam is in stick status. Now if $f_{fk}^i \geq f_{Ck}^i$, two possible cases exist: one in the stick state and the other in the slip state. To distinguish them, we need to check the rate of the friction force. If $df_{fk}^i/dt \leq 0$, the ith beam is in slip status and if $df_{fk}^i/dt > 0$, the ith beam is in stick status.*

3.4 Experiments

3.4.1 Experimental systems and procedures

We designed and fabricated an experimental setup to study the soft-solid contact interaction as shown in Fig. 3.3. Two linear stages in the vertical (z-axis) and the horizontal (x-axis) directions are used to regulate the normal force and the horizontal displacement/friction force, respectively. To simulate the fingertip-like contact, we molded a semi-sphere shape specimen made of urethane rubber (VytaFlex 60, Smooth-On Inc.) A schematic representation of the rubber dimensions is shown in Fig. 3.3(c) and the

values of the geometric parameters are listed in Table 3.1. The specimen is glued on an aluminum plate and installed on a linear stage. A thick transparent acrylic plate is chosen as a flat rigid surface such that we can use camera mounted underneath the plate to capture the image of the soft-solid contact area. A set of small black dots are painted on the surface of the rubber and by using the image processing algorithms we calculate the rubber deformations. Similar to the design in [32], a set of 6 laser line-generators, a high-speed camera (Prosilica GX1050C, 1024x1024 pixels, 112 fps), and an image processing algorithm are used to obtain the contact contour and rubber deformations. The normal and friction force are measured by a 6-DOF force/torque sensor (model 45E15, JR3 Inc.) installed between the linear stage and the rigid plate. A real-time control is performed using the CompactRIO (National Instruments Inc.) embedded system. The sampling frequency for all the components is 100 Hz except the image acquisition rate at 50 fps.

Table 3.1: Fingertip-like rubber geometric and material property parameters (the unit for all geometry variables is millimeter).

R_0	R_1	r	h_1	μ_S	μ_C	a	h	$E[MPa]$	ν	$\rho[g/cm^3]$
65	45	10	10	0.76	0.57	2	22	2e5	0.49	1.04

A set of separate experiments were conducted to obtain the normal load distribution over the contact area. Normal load distribution was measured using a set of 4-cell pressure sensitive electric conductive rubber (PSECR) sensors (see Fig. 3.3(c)). Two PSECR sensors were attached flat side-by-side on the acrylic plate. A rubber sample was loaded several times at different positions along the x-axis with a 5-mm increments until the the entire normal load distribution was scanned from the front to the back end of the contact contour. Each time same magnitude of the normal load was applied as in the sliding experiments.

In sliding motion experiments, we first applied the desired normal load F_z and then moved the linear stage at a constant velocity $\dot{s}$ along the x-axis direction. This
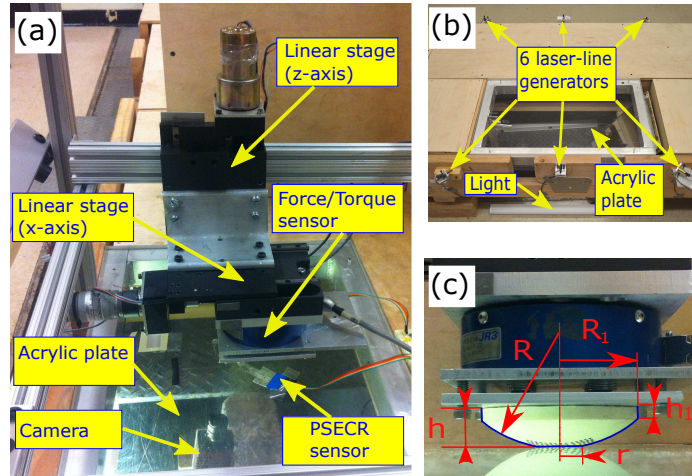
Figure 3.3: Experimental setup for dynamic sliding motion of a fingertip-like rubber against transparent acrylic plate. (a) The entire system of 2-DOF linear stage. (b) Laser line generators setup [32]. (c) Schematics of rubber dimensions.

resulted in increasing the force in the x-axis direction. During this entire process, the normal load was maintained at constant by the linear stage along the z-axis. The sliding distance of the rubber layer was around 20 mm. During the sliding motion, the soft rubber layer exhibited a repeated stick-slip oscillating motion as we discuss and show in the next section.
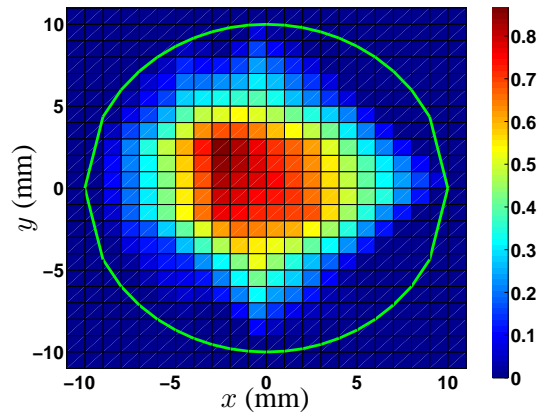
Figure 3.4: Normal load distribution on the contact patch with a normal load $F_z = 80$ N and no applied horizontal external force.

3.4.2 Experimental results

Figure 3.4 shows the applied normal load distribution on the contact patch $\mathcal{P}$. To obtain the normal load at any arbitrary location on $\mathcal{P}$, we use a 4th order polynomial along the x and y-axis to fit the experimental data. To keep symmetry along the both axes, we use an even function $f(x,y) = p_0 + p_2x^2 + p_2y^2 + p_4x^4 + p_{22}x^2y^2 + p_4y^4$ to fit the PSECR sensor measurements. By a least square estimation with additional consideration of no negative pressure distribution on $\mathcal{P}$, we obtain the values for the coefficients as $p_0 = 0.8680$, $p_2 = -0.0198$, $p_{22} = 2.2498 \times 10^{-4}$, and $p_4 = 1.1251 \times 10^{-4}$.

(a)

(b)

(c)
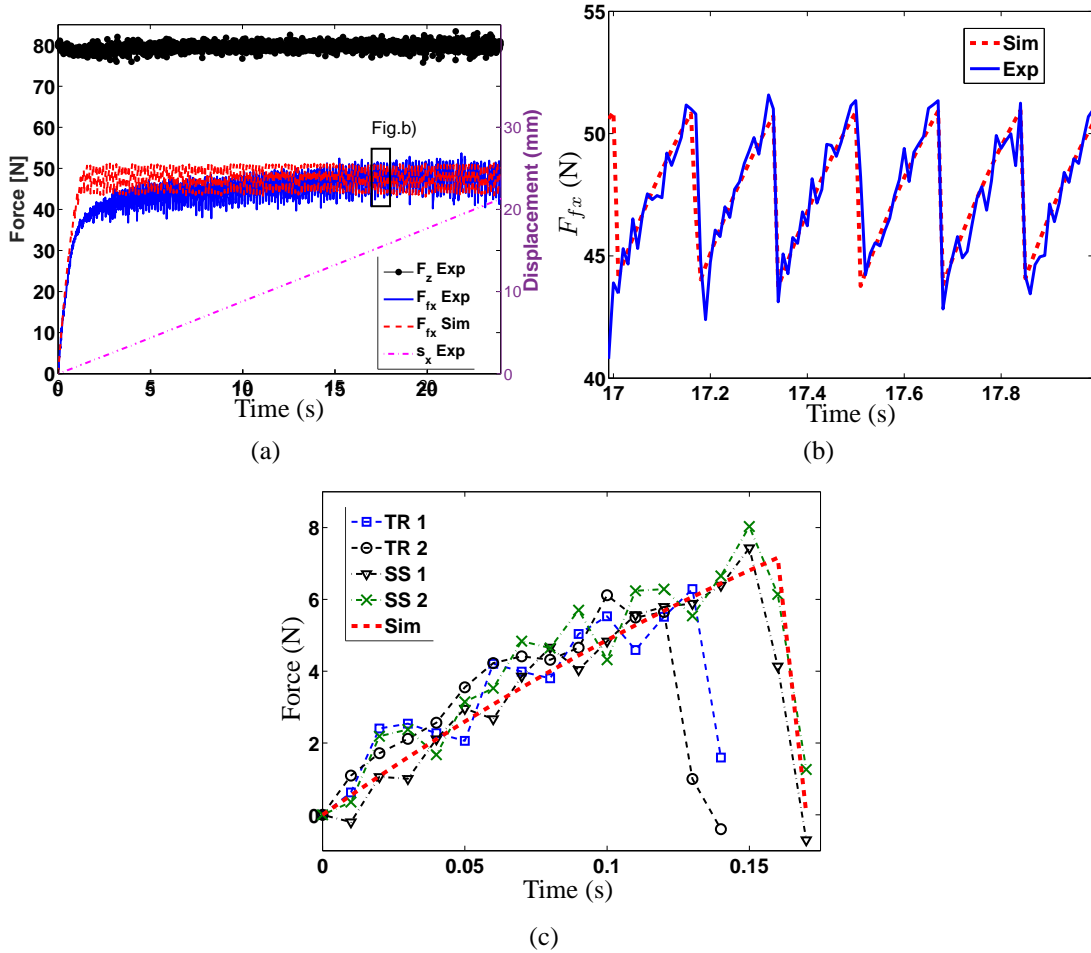
Figure 3.5: Total friction force and linear stage displacement from the experiments and simulation under constant normal load $F_z = 80$ N. (a) Whole range of motion; (b) Zoomed in friction force oscillations; (c) Two representative single stick-slip force oscillation from experimental data for transient (TR) and two for steady state (SS) regime overlaid by one from the simulation results (Sim).

With the above normal load, Fig. 3.5(a) shows the total friction force F_{fx} as well as the contact patch moving displacement s_x. For the first 2 sec., the friction force experiences a rapid increase until micro-slips start causing the average friction force to increase steadily. Then the slip of the entire contact area occurs and the stick-slip motion with periodic friction force oscillations is observed after around 5 sec. By further increasing the sliding distance, the amplitude of the friction force oscillations increases. Finally, the friction force reaches steady state with a constant oscillation amplitude (at around 15 sec). In the figure, we also plot the friction force prediction by the LuGre/beam-network model using the values of the model parameters listed in Table 3.2.

Table 3.2: The values of the LuGre/beam-network model parameters

$\dot{\boldsymbol{s}}_i$ (m/s)	k (N/m)	σ_{0k} (N/m)	σ_{1k} (Ns/m)	σ_{2k} (Ns/m)	v_s (m/s)	α $(/)$	F_z (N)
[8.8e-4; 0]	7.38e4	1e6	$2\sqrt{\sigma_{0k}m}$	0.04	0.002	2	80

Figure 3.5(b) further shows the comparison results between the model prediction and the experiments of the friction force at the stick-slip steady state. The results clearly show that the model predicts the experiments closely. We also compare the friction force oscillating cycles at the beginning of sliding motion and during the steady-state sliding motion. Figure 3.5(c) shows the comparison of two transient (TR) cycles at the beginning of sliding motion (around 5 sec) and two steady-state (SS) cycles (around 17 sec). It is shown that the amplitude of the friction force oscillation increases from 6.5 N to 8 N and time interval increases from 0.145 sec to 0.175 sec, respectively. The slope of the force increase during stick regime remains constant, which implies the beam stiffness k_i is constant during the entire oscillating motion.

Figure 3.6 shows the deformation distribution and its evolution for the initial slip (occurred at around 2 sec). Partial slip starts at the outer ring of the contact patch and
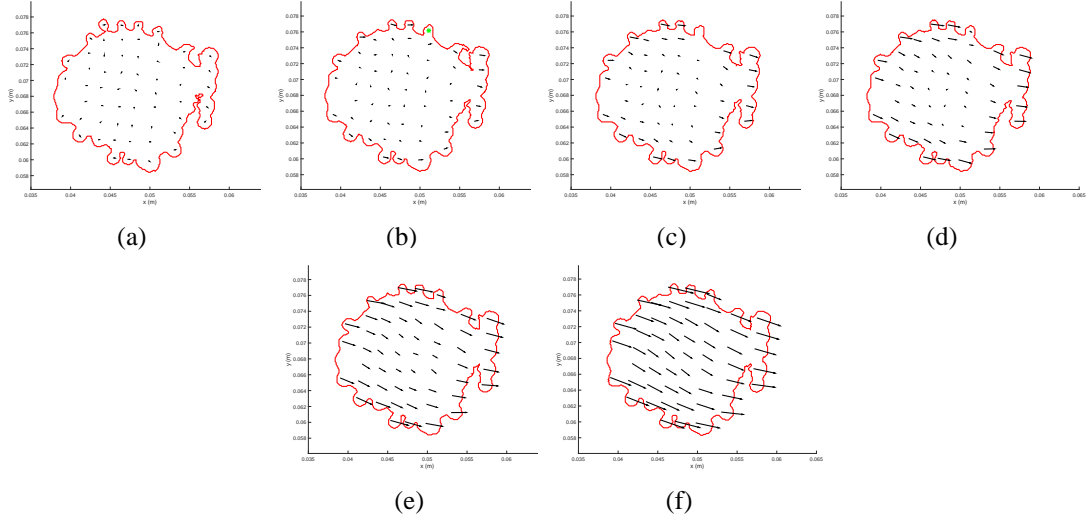
Figure 3.6: Deformation evolution of a very initial stick to slip transition with time increments of 0.1 sec.
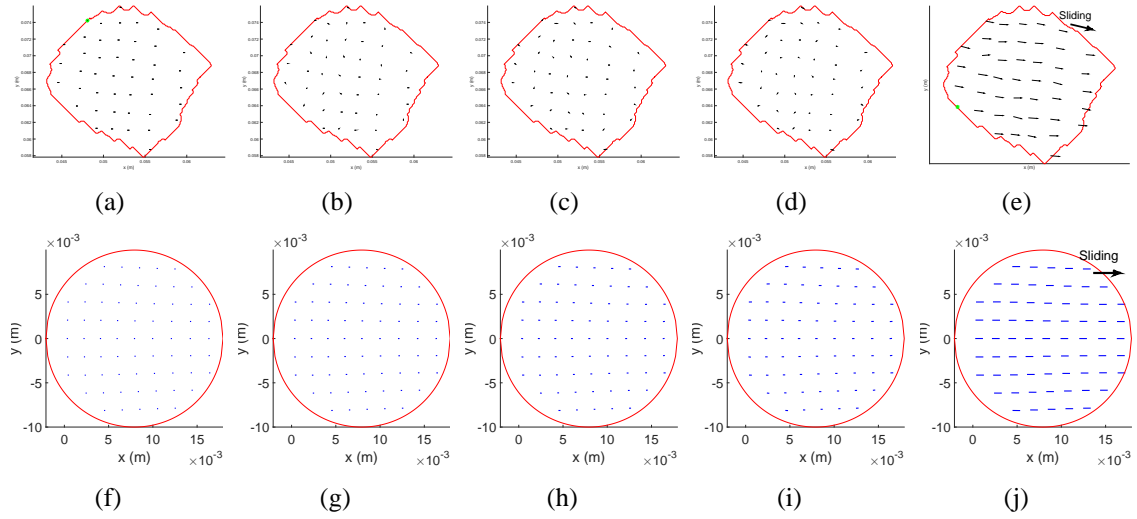
Figure 3.7: Experimental (a)-(e) and simulation (f)-(j) results of deformation evolution of a single stick-slip oscillation during sliding. Time increment between images is 0.04 sec.

then propagates towards the center of $\mathcal{P}$ until the entire patch slides. These results are consistent with that of the tire-road interactions [33] and the human fingertip sliding experiments [37, 38].

Figure 3.7(a)-(e) shows the results of the deformation evolution during steady-state stick-slip oscillating motion. Rapid oscillations cause slip to happen instantaneously

over the entire contact patch. The reason for the fast sliding motion in this case probably lies in the fact that rubber relaxation and elastic deformation responses are much slower than the high dynamic oscillations and thus, the rubber layer acts like a hard material with a rapid evolution of the deformation growth over the contact patch. Similar trend of an instantaneous slip over the entire patch is confirmed through the simulation results shown in Fig. 3.7(f)-(j). Combining with the force prediction shown in Fig. 3.5, these results confirm the LuGre/beam-spring network model captures the soft-solid contact interactions.

Figure 3.8 shows the friction force evolution across the centerline of the contact (at $y = 0$) from the initial loading until steady state sliding. It is interesting to note that the shape of the friction force profile has initially a double-peak feature though the normal load is a central-peak profile. While the slip evolves, the friction force profile becomes a central-peak profile and maintains its shape during sliding oscillation motion. The change of the friction force profiles are clearly shown in the figure from the bottom to the top curves. This observation is similar to the results reported in [33] and the explanation lies in the friction force characteristic and the slip and deformation evolution profile during the process.
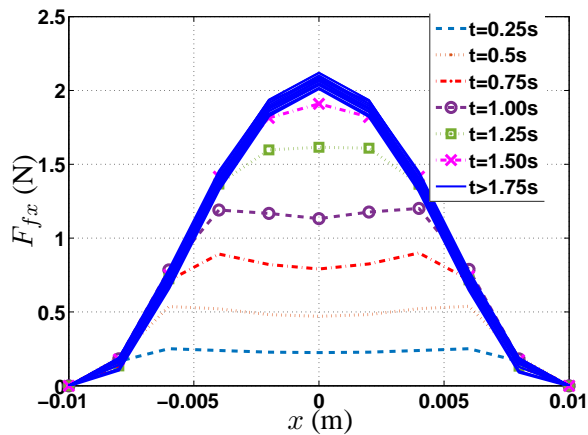
Figure 3.8: Friction force distribution F_{fx} along the x-axis at $y = 0$ for initial loading until steady-state sliding.

When computing the model predictions, the static and dynamic coefficients of frictions are constant. Thus, the model cannot capture the slight increase of the average friction force as observed in experiments and also shown as the blue solid line in Fig 3.5(a). Although not demonstrating here, we can adjust the shape of a Stribeck curve by allowing parameter α and Stribeck velocity term v_s as a time-dependent or sliding distance-dependent parameters to further enhance the model prediction results to match the experiments.

3.5 Conclusion

This chapter presented a novel computational approach to capture the deformation and friction force distributions of the soft-solid contact. The new method integrated the LuGre dynamic friction model and the beam-spring network model. The advantages of the integrated LuGre/beam network model lie in its ability to capture the dynamics of the soft-solid contact and to simplify the calculation of the friction force and deformation distributions on the contact patch. We validated the proposed computational approach through an application of the fingertip-like rubber sliding on the flat rigid surface. The experimental results demonstrated and confirmed that the new model successfully predicted the experimental deformation and force distributions during the steady state stick-slip motion.

Chapter 4

Robotic Bipedal Model for Human Walking with Foot Slip

4.1   Introduction

Humanoid robots share a similar locomotion pattern as the human walker and therefore, robotic bipedal models are highly related to human walking. Bipedal dynamic models have been extensively used to design and control robotic walkers [49]. Recently, multi-link bipedal models are used to predict the human walking gait [52, 102] and design the prosthetic devices for lower-limbs [102]. However, all of these bipedal models assume non-slip conditions at the foot-floor contact and the results cannot be directly used to study locomotion with slips.

In this dissertation, we develop an analytic bipedal model to capture the human walking locomotion with foot slip and to further understand the unsteady, unstable human and humanoid robot locomotion. We first build a foot-floor contact model to capture the foot rolling characteristics. The proposed human locomotion model is built on a 7-link robotic bipedal dynamics with actuated ankle joints. The model includes the dynamics of the both single- and double-stance motion in one stride. Moreover, the model explicitly considers the foot contact slips and therefore, it can predict the human gait under slip conditions. We also conduct extensive human experiments, including both the normal walking gait and the gait with recovered slips, to validate and demonstrate the capability of the new model.

The presented robotic bipedal model in this dissertation extends the robotic bipedal

models to study human walking under foot slip. The new model not only predicts the human gait with slips, but is also helpful for understanding of the motion stability when slips happen. The new bipedal model naturally helps design the balancing controller to prevent human from slip and fall. Besides relaxing the assumption of non-slip foot-floor contact, the new model brings innovative features and properties compared with the other existing bipedal models. For example, compared with the bipedal models with a point, a flat or multi-contact foot in [49, 103–105], the new model includes an experimentally validated foot-floor contact. Unlike the bipedal model in [52] that only deals with a 6-link robotic bipedal for single-stance human locomotion, the proposed model includes the human trunk (e.g., 7-link) and also the double-stance phase in walking gaits, which is crucial for slip and fall motion. Compared with the work in [51, 102] that include the double-stance in human gait, the proposed model includes the active ankle joints and also generates the matched GRF with the experiments. Finally, using the novel wearable sensors [32], we conduct a set of extensive experiments to validate and demonstrate the proposed bipedal model [1].

4.2   Bipedal walking model without slips

In this section, we present a bipedal model for human walking gait without slips. The model considers the actuated ankle joints and the foot geometry and therefore, it can precisely represent not only the joint angles but also the GRFs.

4.2.1   System configuration

Figure 4.1(a) illustrates the setup of the coordinates for bipedal modeling of human walking. The human motion is considered only in the sagittal plane. The human body is considered as a seven-link rigid body. The HAT is considered as one link that is

---

[1]The presented work in this chapter is a joint work that resulted in publication [72]. It is presented here for completeness of this dissertation.
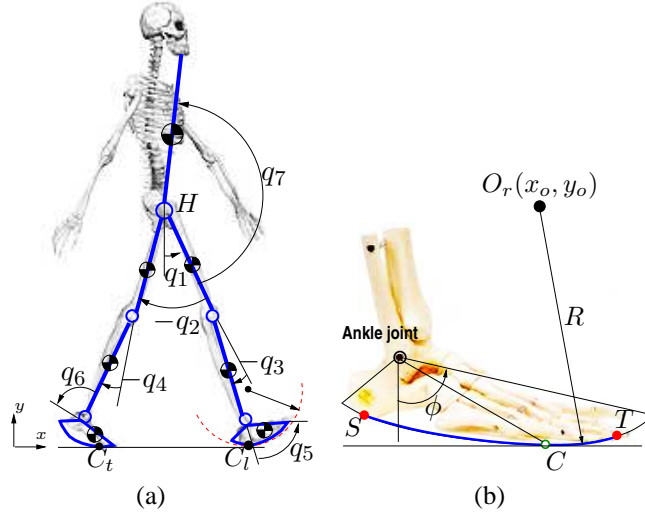
Figure 4.1: (a) Schematic of the 7-link human walking model with curved foot contact. (b) Schematic of the foot-contact model.

connected to the left- and right-thigh. The human has two active hip joints, two active knee joints and two active ankle joints. Similar to those in [52], we use relative angles q_i, $i = 2, \ldots, 7$ to define the configuration of the system and the absolute angle q_1 denotes the leading leg orientation with respect to the vertical position.

We define $\boldsymbol{q}_a = [q_1 \; \cdots \; q_7]^T$ as the gait configuration. The foot-floor contact is considered as a circular disk rolling on the solid ground; see Fig. 4.1(b). To capture the slip motion of stance foot, we denote the position of rotating center O_r of the stance foot rolling as $[x_o \; y_o]^T$. To capture the slipping motion of stance foot, we define a slipping vector $\boldsymbol{q}_s = [x_s \; y_s]^T = [x_o + R\phi \; y_o - R]^T$, where ϕ is the absolute angle of the stance foot with respect to the vertical direction and is a function of $\boldsymbol{q}_a$. It is straightforward to see that when the stance foot is purely rolling on the ground, $\boldsymbol{q}_s = \boldsymbol{0}$. We use $\boldsymbol{q}_s$ and $\boldsymbol{q}_a$ (i.e., foot rotating angle) to calculate the stance foot-floor contact point C. To completely determine the walking gait with foot slip, we define generalized $\boldsymbol{q}_e = [\boldsymbol{q}_a^T \; \boldsymbol{q}_s^T]^T$.

A human walking cycle consists of a series of repeated sequential movements and events [49]. During the *single-stance phase*, the stance foot rolls on the ground while the swing foot moves in the air from position behind to in front of the stance foot. The

robotic bipedal in the single-stance phase is underactuated [49]. Once the swinging foot impacts on the ground (i.e., heel-touch), the joint velocity suddenly changes and the joint configuration is relabeled due to the switching role of the stance and swing legs. The *double-stance phase* refers to the stage when both legs roll on the ground. In this phase, the joint velocity satisfies a two-dimensional constraint and the system is overactuated or fully actuated. Finally, the trailing stance foot leaves the ground (i.e., toe-off) and the pose returns to the single-stance phase. Hybrid models shown in Fig. 4.2 are used to capture the above-mentioned discrete-continuous dynamics.

4.2.2   Single- and double-stance models and gait controller

The non-slip single-stance dynamics are described as [49]

$$\Sigma_s: \quad \boldsymbol{D}_s(\boldsymbol{q}_a)\ddot{\boldsymbol{q}}_a + \boldsymbol{C}_s(\boldsymbol{q}_a, \dot{\boldsymbol{q}}_a)\dot{\boldsymbol{q}}_a + \boldsymbol{G}_s(\boldsymbol{q}_a) = \boldsymbol{B}_s\boldsymbol{u}, \tag{4.1}$$

where $\boldsymbol{D}_s(\boldsymbol{q}_a)$, $\boldsymbol{C}_s(\boldsymbol{q}_a, \dot{\boldsymbol{q}}_a)$, $\boldsymbol{G}_s(\boldsymbol{q}_a)$ and $\boldsymbol{B}_s$ are the inertia, Coriolis, gravity and input mapping matrices, respectively. There are six joint torque inputs $\boldsymbol{u} \in \mathbb{R}^6$ and the system is underactuation since absolute joint angle q_1 is not controlled by any joint torque. To use (4.1) for modeling human walking gait, a feedback linearization approach is adopted to control the joint angles $\boldsymbol{q}_a$ to follow a desired trajectory that is specified by a progression variable $\theta = \boldsymbol{c}\boldsymbol{q}_a$, where $\boldsymbol{c}$ is a constant progression vector. During the single-stance phase, θ monotonically increases and the desired trajectory of actuated joint angles are expressed by θ. The feedback linearization controller then enforces the virtual constraint specified by

$$\boldsymbol{y} = \boldsymbol{h}(\boldsymbol{q}_a) = \boldsymbol{H}_0\boldsymbol{q}_a - \boldsymbol{h}_d(\theta) = \boldsymbol{0}. \tag{4.2}$$

If $\boldsymbol{u}$ is properly chosen by feedback linearization to drive $\boldsymbol{y} = \dot{\boldsymbol{y}} = \boldsymbol{0}$, only the dynamics of θ is left as the zero dynamics [49].

To calculate the GRF for single-stance walking, we treat the 7-link human walker as one rigid body that is subject to only three external forces, i.e., gravitational force and

stance foot GRF, including normal force F_n and tangential force F_x. It is straightforward to obtain F_x and F_n by Newtonian mechanics. This force calculation method can be also generalized to the single-stance slip case that will be discussed in Section 4.3.2.

During the double-stance phase, both the leading and trailing feet are in contact with the ground at contact points C_l and C_t, respectively, see Fig. 4.1(a). We here consider a general modeling approach by defining slipping vectors $\boldsymbol{g}_l(\boldsymbol{q}_e) \in \mathbb{R}^2$ and $\boldsymbol{g}_t(\boldsymbol{q}_e) \in \mathbb{R}^2$ of contact points C_l and C_t, respectively. Note that both $\boldsymbol{g}_l(\boldsymbol{q}_e)$ and $\boldsymbol{g}_t(\boldsymbol{q}_e)$ are determined as functions of the extended coordinates $\boldsymbol{q}_e$. Because of the constraints at the foot-floor contact interactions, the equations of motion during the double-stance can be expressed as

$$\Sigma_d : \ \boldsymbol{D}_e(\boldsymbol{q}_e)\ddot{\boldsymbol{q}}_e + \boldsymbol{C}_e(\boldsymbol{q}_e, \dot{\boldsymbol{q}}_e)\dot{\boldsymbol{q}}_e + \boldsymbol{G}_e(\boldsymbol{q}_e) = \boldsymbol{B}_e\boldsymbol{u} + \boldsymbol{E}_e^T\boldsymbol{F}_e, \qquad (4.3)$$

where $\boldsymbol{D}_e(\boldsymbol{q}_e)$, $\boldsymbol{C}_e(\boldsymbol{q}_e, \dot{\boldsymbol{q}}_e)$, $\boldsymbol{G}_e(\boldsymbol{q}_e)$ and $\boldsymbol{B}_e$ are the inertia, Coriolis, gravity and input mapping matrices, respectively. Matrix $\boldsymbol{E}_e = [\frac{\partial \boldsymbol{g}_t(\boldsymbol{q}_e)}{\partial \boldsymbol{q}_e} \ \frac{\partial \boldsymbol{g}_l(\boldsymbol{q}_e)}{\partial \boldsymbol{q}_e}]^T \in \mathbb{R}^{4 \times 9}$ describes the contact constraints and $\boldsymbol{F}_e = [F_{xt} \ F_{nt} \ F_{xl} \ F_{nl}]^T$ is a vector of the collection of the tangential and normal forces at C_t and C_l, respectively. Note that with non-slip conditions at C_l and C_t, we have four kinematic constraints $\boldsymbol{E}_e\dot{\boldsymbol{q}}_e = \boldsymbol{0}$ and the degree of freedom given by (4.3) is $9 - 4 = 5$.

Since there are six active joints and five degrees of freedom, the bipedal system is *overactuated*. Using a similar derivation as in [51], the constrained dynamics can be reformulated as

$$\boldsymbol{D}_{di}\ddot{\boldsymbol{q}}_{di} + \boldsymbol{C}_{di}\dot{\boldsymbol{q}}_{di} + \boldsymbol{G}_{di} = \boldsymbol{M}_{di}\boldsymbol{u}, \qquad (4.4)$$

where subscript "di" denotes double-stance independent variable dynamics and $\boldsymbol{q}_{di} = [q_1 \ q_2 \ q_3 \ q_5 \ q_7]^T$ and $\boldsymbol{M}_{di} \in \mathbb{R}^{5 \times 6}$ maps the six joint torques into the five dimensional dynamics. To predict double-stance human gaits by (4.4), a Bézier polynomial is used to parameterize the desired trajectory of $\boldsymbol{q}_{di}^d$ [49]. The control input $\boldsymbol{u}$ is designed such that $\ddot{\boldsymbol{q}}_{di} = \boldsymbol{D}_{di}^{-1}(\boldsymbol{M}_{di}\boldsymbol{u} - \boldsymbol{C}_{di}\dot{\boldsymbol{q}}_{di} - \boldsymbol{G}_{di}) = \ddot{\boldsymbol{q}}_{di}^d - \boldsymbol{K}_p(\boldsymbol{q}_{di} - \boldsymbol{q}_{di}^d) - \boldsymbol{K}_d(\dot{\boldsymbol{q}}_{di} - \dot{\boldsymbol{q}}_{di}^d)$, where

$\boldsymbol{K}_p$ and $\boldsymbol{K}_d$ are constant gain matrices. To solve $\boldsymbol{u}$ in the above equation, we need an extra constraint because of the overactuation configuration. In our implementation, we take a simple linear constraint of the joint torques that is determined by the single-stance joint torque profiles.

To calculate the ground reaction forces $\boldsymbol{F}_e$, we take time derivative of the kinematic constraint $\boldsymbol{E}_e \dot{\boldsymbol{q}}_e = \boldsymbol{0}$. Stacking with the dynamics (4.3), we obtain (argument variables in the coefficient matrices are dropped for clarity)

$$\underbrace{\begin{bmatrix} \boldsymbol{D}_e & -\boldsymbol{E}_e^T \\ \boldsymbol{E}_e & \boldsymbol{0} \end{bmatrix}}_{\boldsymbol{D}_{\text{ext}}} \begin{bmatrix} \ddot{\boldsymbol{q}}_e \\ \boldsymbol{F}_e \end{bmatrix} = \begin{bmatrix} \boldsymbol{B}_e \\ \boldsymbol{0} \end{bmatrix} \boldsymbol{u} - \begin{bmatrix} \boldsymbol{C}_e \\ \dot{\boldsymbol{E}}_e \end{bmatrix} \dot{\boldsymbol{q}}_e - \begin{bmatrix} \boldsymbol{G}_e \\ \boldsymbol{0} \end{bmatrix}. \tag{4.5}$$

Since matrix $\boldsymbol{D}_{\text{ext}}$ is full rank, both $\ddot{\boldsymbol{q}}_e$ and forces $\boldsymbol{F}_e$ are obtained with the known joint torques $\boldsymbol{u}$ from the controller design discussed above.

4.2.3 Impacting model

We use the extended configuration coordinate $\boldsymbol{q}_e \in \mathbb{R}^9$ to describe the impact dynamics. After the impact, the swing leg sticks on the ground and thus, the velocity of the swing leg contact point is zero. We clearly express the impact mapping $\mathcal{H}_s^d$ as the pre-impact joint velocity $\dot{\boldsymbol{q}}_e^-$ of the single-stance phase to the post-impact joint velocity $\dot{\boldsymbol{q}}_e^+$ of the double-stance phase as

$$\mathcal{H}_s^d: \begin{bmatrix} \boldsymbol{D}_e(\boldsymbol{q}_e^-) & -\boldsymbol{E}_e^T \\ \boldsymbol{E}_e & \boldsymbol{0} \end{bmatrix} \begin{bmatrix} \dot{\boldsymbol{q}}_e^+ \\ \delta \boldsymbol{F}_e \end{bmatrix} = \begin{bmatrix} \boldsymbol{D}_e(\boldsymbol{q}_e^-) \dot{\boldsymbol{q}}_e^- \\ \boldsymbol{0} \end{bmatrix}. \tag{4.6}$$

In (4.6), superscripts "$+$" and "$-$" are used to indicate the instants just after and before the impact event, respectively. Also, we know that $\boldsymbol{q}_e^+ = \boldsymbol{q}_e^-$. Same as [49, 51], a relabeling process is applied to the joint angles and their velocities after the impact. For the transition from the double-stance to single-stance phases, the transition can be straightforward obtained as

$$\mathcal{H}_d^s: \quad \boldsymbol{q}_e^+ = \boldsymbol{q}_e^-, \ \dot{\boldsymbol{q}}_e^+ = \dot{\boldsymbol{q}}_e^-. \tag{4.7}$$

4.2.4 Model optimization for human walking gait

To apply the bipedal model to human gait, we need to tune the model parameters to fit the human walking data. During the human walking experiments, all joint angles and the GRF information are collected and obtained [32, 106].

For single-stance dynamics (4.1), we need to identify and match the virtual constraint $\boldsymbol{h}(\boldsymbol{q}_a)$ in (4.2) from the collected joint angles. We use $\boldsymbol{H}_0 = [\boldsymbol{0} \ \boldsymbol{I}_6]$, where $\boldsymbol{I}_N$ is the $N \times N$ identity matrix, to choose the active joints [49]. The desired trajectory $\boldsymbol{h}_d$ is parameterized by the Bézier polynomial. To fit the double-stance model (4.3), we choose to optimize the Bézier spline parameters α_d such that the desired trajectory $\boldsymbol{q}_{di}^d = \boldsymbol{q}_{di}^d(\alpha_d, t)$ approximates the human walking and also avoids unrealistic high joint-angular acceleration. We take the joint angular acceleration into the optimization process because the GRF matching is one of the targets besides matching the joint angles between the model prediction and the human gaits. To achieve such goal and obtain optimal α_d, we minimize the following objective function

$$J_d(\alpha_d) = \int_{t_0}^{t_f} \|\boldsymbol{q}_{di}^d(\alpha_d, t) - \boldsymbol{q}_{di}^e\|^2 + \gamma \|\ddot{\boldsymbol{q}}_{di}^d(\alpha_d, t)\|^2 dt, \tag{4.8}$$

where $\gamma > 0$ is a weighting factor and $[t_0, \ t_f]$ is the time interval in experiments and $\boldsymbol{q}_{di}^e$ is the measured joint angle profiles. By the property of the Bézier polynomials, we can analytically express both terms of $\boldsymbol{q}_{di}^d$ and $\ddot{\boldsymbol{q}}_{di}^d$ as functions of α_d and therefore, the optimal α_d can be obtained using a scaled conjugate gradient method. We will demonstrate the comparison results between the model prediction and the experiments in Section 4.4.

4.3 Bipedal walking model with foot-floor contact slip

In this section, we extend the bipedal model in the previous section to consider the foot-floor contact slip. We first present an overview of the extended hybrid model and then the detailed dynamics are discussed.

4.3.1 Hybrid model for walking with slips

Figure 4.2 shows the finite state diagram of the hybrid bipedal model for human walking with foot-floor contact slip. For the normal walking gait, the hybrid dynamics contain two states: non-slip single-stance and double-stance phases shown as $\mathcal{S}_1$ and $\mathcal{S}_2$, respectively. The heel-touch and toe-off events trigger the switching between $\mathcal{S}_1$ and $\mathcal{S}_2$ with the impact mappings $\mathcal{H}_s^d$ and $\mathcal{H}_d^s$, respectively.
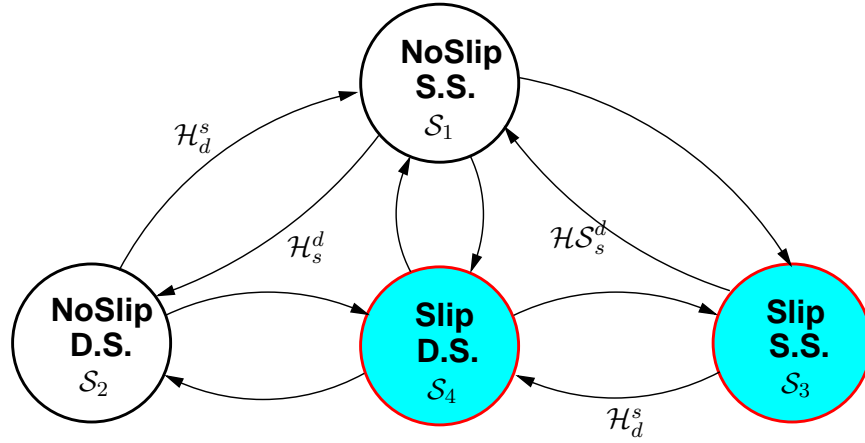
Figure 4.2: Finite state diagram of human walking gait with slips.

The foot slip can happen during the single- and double-stance phases. Therefore, two new states as shown in Fig. 4.2 are introduced for the gaits with slip: single-stance slip phase $\mathcal{S}_3$ and double-stance slip phase $\mathcal{S}_4$. State $\mathcal{S}_4$ includes the cases where slip happens on the stance leg only, the swing leg only, or both legs simultaneously. The transitions among $\mathcal{S}_1, \ldots, \mathcal{S}_4$ shown in the figure represent the human slip recovery strategies. For example, as we will show in the case study in Section 4.4, one slip recovery strategy can be represented in the sequence of $\mathcal{S}_1 \rightarrow \mathcal{S}_4 \rightarrow \mathcal{S}_3 \rightarrow \mathcal{S}_1$. The human starts with normal single-stance $\mathcal{S}_1$ without slip. Slip is initiated right after the swing leg touches on the ground, i.e., double-stance slip phase ($\mathcal{S}_4$). When slip evolves, the swing leg is lifted off the ground so the walking gait is in single-stance slip phase, i.e., $\mathcal{S}_3$. Then, the human detects the slip and the swing leg touches down on the ground

and becomes a non-slip stance leg. Meanwhile, the other slipping leg leaves the ground contact and the gait recovers to the non-slip single-stance phase, namely, $\mathcal{S}_1$.

The details of each transition in the finite state diagram are parts of the required human slip recovery strategies. These slip recovery strategies are out of the scope of this chapter and will be discussed in Chapter 6, thus we omit the discussion here. In the following, we describe the extension of the motion and impact dynamics of the single- and double-stance phases to include foot slips.

4.3.2   Single-stance slip model and gait controller

Due to the foot-floor contact slips, we need to use the extended configuration coordinate $\boldsymbol{q}_e = [\boldsymbol{q}_a^T \ \boldsymbol{q}_s^T]^T = [\boldsymbol{q}_a^T \ x_s \ y_s]^T$ to describe the motion. The dynamic model is obtained as

$$
\underbrace{\begin{bmatrix} \boldsymbol{D}_{es}^{11} \vdots \boldsymbol{D}_{es}^{12} \\ \boldsymbol{D}_{es}^{21} \vdots \boldsymbol{D}_{es}^{22} \\ \boldsymbol{D}_{es}^{31} \vdots \boldsymbol{D}_{es}^{32} \end{bmatrix}}_{\boldsymbol{D}_{es}} \begin{bmatrix} \ddot{\boldsymbol{q}}_a \\ \ddot{x}_s \\ \ddot{y}_s \end{bmatrix} + \underbrace{\begin{bmatrix} C_{es}^{11} \vdots C_{es}^{12} \\ \boldsymbol{C}_{es}^{21} \vdots \boldsymbol{C}_{es}^{22} \\ \boldsymbol{C}_{es}^{31} \vdots C_{es}^{32} \end{bmatrix}}_{\boldsymbol{C}_{es}} \begin{bmatrix} \dot{\boldsymbol{q}}_a \\ \dot{x}_s \\ \dot{y}_s \end{bmatrix} + \underbrace{\begin{bmatrix} \boldsymbol{G}_{es}^1 \\ G_{es}^2 \\ G_{es}^3 \end{bmatrix}}_{\boldsymbol{G}_{es}} = \begin{bmatrix} \boldsymbol{B}_{es}\boldsymbol{u} \\ F_x \\ F_n \end{bmatrix} = \begin{bmatrix} \boldsymbol{B}_{es}\boldsymbol{u} \\ \boldsymbol{F}_{es} \end{bmatrix}, \text{(4.9)}
$$

where $\boldsymbol{D}_{es} \in \mathbb{R}^{9\times9}$, $\boldsymbol{C}_{es} \in \mathbb{R}^{9\times9}$, $\boldsymbol{G}_{es} \in \mathbb{R}^9$ and $\boldsymbol{B}_{es} \in \mathbb{R}^{7\times6}$ are the inertia, Coriolis, gravity and input mapping matrices, respectively. External force $\boldsymbol{F}_{es} = [F_x \ F_n]^T$ is the frictional (tangential) and normal forces at the stance foot.

Note that the stance foot always lies in contact with the ground during slipping (i.e., $y_s = 0$) and therefore, we have constraint $\boldsymbol{q}_s = [x_s \ y_s]^T = [x_s \ 0]^T$. Also, we have $F_x = -\mu F_n$, where μ is the friction coefficient between the shoe sole and the ground floor. With these constraints, we further simplify (4.9) by defining new coordinate variable $\boldsymbol{q}_{es} = [\boldsymbol{q}_a \ x_s]^T \in \mathbb{R}^8$ and eliminating external force F_n and finally obtain

$$
\Sigma_s^s: \ \boldsymbol{D}_{es}^s \ddot{\boldsymbol{q}}_{es} + \boldsymbol{C}_{es}^s \dot{\boldsymbol{q}}_{es} + \boldsymbol{G}_{es}^s = \boldsymbol{B}_{es}^s \boldsymbol{u}, \tag{4.10}
$$

where

$$\boldsymbol{D}_{es}^s = \begin{bmatrix} \boldsymbol{D}_{es}^{11} \\ \boldsymbol{D}_{es}^{21} + \mu \boldsymbol{D}_{es}^{31} \end{bmatrix}, \, \boldsymbol{C}_{es}^s = \begin{bmatrix} \boldsymbol{C}_{es}^{11} \\ \boldsymbol{C}_{es}^{21} + \mu \boldsymbol{C}_{es}^{31} \end{bmatrix} \in \mathbb{R}^{8 \times 8},$$

$$\boldsymbol{G}_{es}^s = \begin{bmatrix} \boldsymbol{G}_{es}^1 \\ G_{es}^2 + \mu G_{es}^3 \end{bmatrix} \in \mathbb{R}^8, \, \boldsymbol{B}_{es}^s = \begin{bmatrix} \boldsymbol{B}_{es} \\ \boldsymbol{0} \end{bmatrix} \in \mathbb{R}^{8 \times 6}.$$

System (4.10) has eight state variables and six joint torques as inputs and therefore, it is underactuated. The absolute joint angle q_1 and the slipping distance x_s are underactuated variables. To use model (4.10) for human gait prediction, we adopt a similar controller as for non-slip case. A six-dimensional holonomic virtual constraint $\boldsymbol{y} = \boldsymbol{h}(\boldsymbol{q}_a) = \boldsymbol{H}_0 \boldsymbol{q}_a - \boldsymbol{h}_d(\theta_s)$ is used to design the control system, where $\theta_s = \boldsymbol{c}_s \boldsymbol{q}_a$ and $\boldsymbol{c}_s$ is chosen to insure $[\boldsymbol{H}_0^T \ \boldsymbol{c}_s^T]^T$ has full rank. Similar to the non-slip case, letting $\boldsymbol{\eta} = \boldsymbol{h}(\boldsymbol{q}_a)$, the control $\boldsymbol{u}$ is chosen to regulate $\boldsymbol{\eta} = \dot{\boldsymbol{\eta}} = \boldsymbol{0}$ and the zero dynamics can be obtained. Specifically, we define $\xi_s = \left(\boldsymbol{D}_{es}^{11} \right)_1 \dot{\boldsymbol{q}}_a$, where $\left(\boldsymbol{D}_{es}^{11} \right)_1$ is the first seven elements of the first row of matrix $\boldsymbol{D}_{es}^{11}$ and it corresponds to the unactuated variable q_1. The dynamics of ξ_s and $\dot{x}_s$ are indeed the zero dynamics of the system. Compared with the non-slip single-stance case, the zero dynamics of the slip walking model contain one additional variable $\dot{x}_s$.

4.3.3 Double-stance slip model and gait controller

During the double-stance slip gait, either (1) only one of two feet slips while the other foot purely rolls on the ground, or (2) both feet slide on the ground. These two situations share the same equations of motion given by (4.3) but with different governing constraints. For first case (1), we always define the non-slipping leg as the stance leg and from the stance leg, we define the absolute joint angle q_1, see Fig. 4.1(a). For second case (2), we take either leg as the stance leg.

By such arrangements, for case (1), without loss of generality, we assume that the

trailing leg is non-slip and is the stance leg. Therefore, we have kinematic constraints $\boldsymbol{g}_t(\boldsymbol{q}_e) = \boldsymbol{0}$ and $(\boldsymbol{g}_l(\boldsymbol{q}_e))_2 = 0$, where $(\boldsymbol{g}_i(\boldsymbol{q}_e))_j$, $i = l, t$, $j = 1, 2$, represents the jth coordinate of slipping vector $\boldsymbol{g}_i(\boldsymbol{q}_e)$. Moreover, we have the kinetic constraints $F_{xl} = -\mu F_{nl}$ for slipping foot. Similarly, for case (2), we have the kinematic constraints $(\boldsymbol{g}_t(\boldsymbol{q}_e))_2 = (\boldsymbol{g}_l(\boldsymbol{q}_e))_2 = 0$ and kinetic constraints $F_{xt} = -\mu F_{tn}$ and $F_{xl} = -\mu F_{nl}$. In the following, we only present the dynamics for case (1) and similar results can be obtained for case (2).

Because of constraints $\boldsymbol{g}_t(\boldsymbol{q}_e) = \boldsymbol{0}$ and $\boldsymbol{g}_l(\boldsymbol{q}_e)_2 = 0$, we obtain $\frac{\partial \boldsymbol{g}_t}{\partial \boldsymbol{q}_e}\dot{\boldsymbol{q}}_e = \boldsymbol{0}$ and $\frac{\partial(\boldsymbol{g}_l(\boldsymbol{q}_e))_2}{\partial \boldsymbol{q}_e}\dot{\boldsymbol{q}}_e = 0$. Using the definition of $\boldsymbol{E}_e$ in (4.3), these kinematic constraints can be written into compact form $\boldsymbol{E}_{es}\dot{\boldsymbol{q}}_e = \boldsymbol{0}$, where $\boldsymbol{E}_{es} := (\boldsymbol{E}_e)_{[1,2,4]} \in \mathbb{R}^{3\times 9}$ is a matrix formed by taking rows $1, 2$ and 4 of $\boldsymbol{E}_e$. Similarly, the kinetic constraint $F_{xl} = -\mu F_{nl}$ is used to re-write the external force vector in (4.3) as

$$
\boldsymbol{F}_e = \underbrace{\begin{bmatrix} 1 & 0 & 0 \\ 0 & 1 & 0 \\ 0 & 0 & -\mu \\ 0 & 0 & 1 \end{bmatrix}}_{\boldsymbol{C}_f} \underbrace{\begin{bmatrix} F_{xt} \\ F_{nt} \\ F_{nl} \end{bmatrix}}_{\boldsymbol{F}_{e3}} = \boldsymbol{C}_f \boldsymbol{F}_{e3}. \tag{4.11}
$$

Similar to the treatment to obtain (4.5), by taking derivative of velocity constraint $\boldsymbol{E}_{es}\dot{\boldsymbol{q}}_e = \boldsymbol{0}$ and stacking with the simplified (4.3) and (4.11), we obtain

$$
\underbrace{\begin{bmatrix} \boldsymbol{D}_e & -\boldsymbol{E}_e^T\boldsymbol{C}_f \\ \boldsymbol{E}_{es} & \boldsymbol{0} \end{bmatrix}}_{\boldsymbol{D}_{\text{ext}}^s} \begin{bmatrix} \ddot{\boldsymbol{q}}_e \\ \boldsymbol{F}_{e3} \end{bmatrix} = \underbrace{\begin{bmatrix} \boldsymbol{B}_e \\ \boldsymbol{0} \end{bmatrix}}_{\boldsymbol{B}_{\text{ext}}^s} \boldsymbol{u} - \underbrace{\begin{bmatrix} \boldsymbol{C}_e \\ \dot{\boldsymbol{E}}_{es} \end{bmatrix}}_{\boldsymbol{C}_{\text{ext}}^s} \dot{\boldsymbol{q}}_e - \begin{bmatrix} \boldsymbol{G}_e \\ \boldsymbol{0} \end{bmatrix}.
$$

Matrix $\boldsymbol{D}_{\text{ext}}^s$ has full rank and therefore $\ddot{\boldsymbol{q}}_e$ and $\boldsymbol{F}_{e3}$ are uniquely determined once the current state variables and joint torques $\boldsymbol{u}$ are given. Since the three dimensional constraints $\boldsymbol{E}_{es}\dot{\boldsymbol{q}}_e = \boldsymbol{0}$ are enforced, the degrees of freedom of the system are $9 - 3 = 6$. Therefore, the system is *fully actuated*.

Letting $\boldsymbol{q}_i = [q_1\, q_2\, q_3\, q_4\, q_5\, q_7]^T = \boldsymbol{S}\boldsymbol{q}_e$ be the independent variables, where $\boldsymbol{S} \in$

$\mathbb{R}^{6\times 9}$ is a constant transformation matrix from $\boldsymbol{q}_e$ to $\boldsymbol{q}_i$, we express $\ddot{\boldsymbol{q}}_i = \boldsymbol{S}(\boldsymbol{D}_{\text{ext}}^{s\ -1}\boldsymbol{B}_{\text{ext}}^s\boldsymbol{u} + \boldsymbol{D}_{\text{ext}}^{s\ -1}\boldsymbol{C}_{\text{ext}}^s)$, where $\boldsymbol{S}\boldsymbol{D}_{\text{ext}}^{s\ -1}\boldsymbol{B}_{\text{ext}}^s \in \mathbb{R}^{6\times 6}$ is a full rank matrix. To track a given trajectory $\boldsymbol{q}_i^d$, the controlled joint torque can be designed as $\boldsymbol{u} = (\boldsymbol{S}\boldsymbol{D}_{\text{ext}}^{s\ -1}\boldsymbol{B}_{\text{ext}}^s)^{-1}(\ddot{\boldsymbol{q}}_i^d - \boldsymbol{K}_p(\boldsymbol{q}_i - \boldsymbol{q}_i^d) - \boldsymbol{K}_d(\dot{\boldsymbol{q}}_i - \dot{\boldsymbol{q}}_i^d) - \boldsymbol{S}\boldsymbol{D}_{\text{ext}}^{s\ -1}\boldsymbol{C}_{\text{ext}}^s)$, where $\boldsymbol{K}_p$ and $\boldsymbol{K}_d$ are constant gain matrices.

4.3.4 Impact model for walking gait with foot slip

The impact model under slip can be obtained from the results presented in Section 4.2.3 for the non-slip case. The main difference is that the slip can happen right after the impact and therefore, the velocity of heel-touch contact point C_l is possibly nonzero after impact, unlike zero in non-slip case. From the discussion in the previous sections, we have the velocity constraint $\boldsymbol{E}_e\dot{\boldsymbol{q}}_e = \boldsymbol{v}_{\text{slip}} = [0\ 0\ v_{\text{slip}}\ 0]^T$, where v_{slip} is the slipping velocity of point C_l (along the x-axis direction) after the heel-touch impact. Therefore, we obtain

$$\mathcal{HS}_s^d : \begin{bmatrix} \boldsymbol{D}_e(\boldsymbol{q}_e^-) & -\boldsymbol{E}_e^T \\ \boldsymbol{E}_e & \boldsymbol{0} \end{bmatrix} \begin{bmatrix} \dot{\boldsymbol{q}}_e^+ \\ \delta\boldsymbol{F}_e \end{bmatrix} = \begin{bmatrix} \boldsymbol{D}_e(\boldsymbol{q}_e^-)\dot{\boldsymbol{q}}_e^- \\ \boldsymbol{v}_{\text{slip}} \end{bmatrix}. \tag{4.12}$$

4.4 Experiments

In this section, we present the experiments to validate the robotic bipedal models for human walking with slips. Figure 2.1 shows the experimental setup for this study. The human subjects walk on the wooden platform in the laboratory. The human subject is first asked to walk on the platform to become familiar with the testing environment before he is asked to repeat walking on the platform with reduced coefficients of friction to induce foot slip. The portion of the platform with the reduced coefficient of friction is not noticeable to the subject such that he still keeps the normal gait before slip starts on one touch-down foot.

The human walking gait is captured by the optical motion tracking system (8 Bonita

cameras from Vicon Inc.). A small wireless inertial measurement unit (from Motion Sense Inc.) is also attached to each shoe to obtain the kinematic information of the foot and potentially for slip detection. Two six degree-of-freedom (6-DOF) force/torque sensors (model SS-1 from INSENCO Co., Ltd) are located inside the shoe to measure the 3D GRF and torques of the foot-floor contact; see Fig. 2.1. These 6-DOF force sensors are thin (around 12-17 mm in thickness) and the human keep normal walking gait when wearing the shoes with embedded force sensors. The force and torque measurements are transmitted through wireless network to the host computer. The GRF sensors and the motion capture system are synchronized for data collection. The details of discussion about the experimental setup are reported in [32].

We test and validate the foot rolling geometry using the normal walking motion data. Figure 4.3(a) shows the foot center of pressure (COP) trajectory in the ankle frame. The data confirm the circular shape of the rolling model with radius $R = 0.22$ m with its center located at $(0.015, 0.096)$ m in the ankle frame. We use these estimated values in the bipedal model. Figure 4.3 shows the comparison results of the seven joint angles by the model prediction and the experiments of normal walking gait. We present these results over a normalized stance S due to the symmetry between the left and right legs. The stance is defined as the time duration from stance foot heel-touch to toe-off. The human subject walks at a speed of around 1.2 m/s and the double-stance consists of around 28% of the entire gait cycle. As shown in Fig. 4.3, the model predictions (blue solid lines) match the experiments (red dash lines) closely for both the single-stance and double-stance phases. Figure 4.4 further shows the comparison results of the GRF (i.e., F_n and F_x) of the stance leg. Unlike the diverge results in literature (e.g., [51]), the model prediction results follow the trend of the force measurements from the smart shoe sensors. The discontinuity of the predicted GRF takes place at the phase switching moments due to the calculation errors of the joint angle accelerations from the single-stance and the double-stance models.
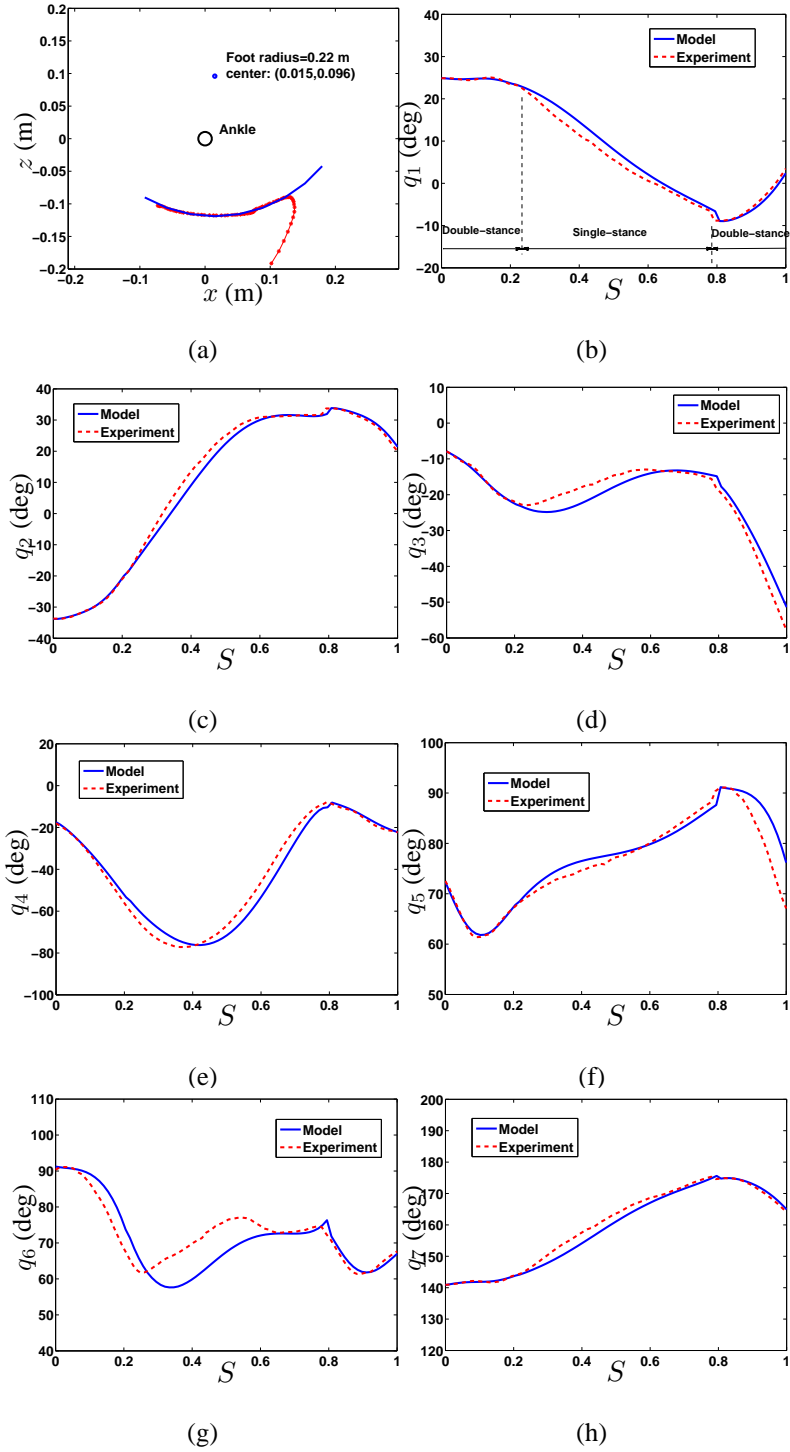
Figure 4.3: (a) Experimental data to calculate the foot-floor contact rolling geometry. The red stars indicate the center of the pressure (COP) trajectory in the ankle frame and the blue curve is the fitting circular rolling shape. (b)-(h): Joint angle (q_1 to q_7) comparison between the model prediction and the experiments during normal gait over one stance. The solid lines represent the model predictions and the dash lines show the experimental data.
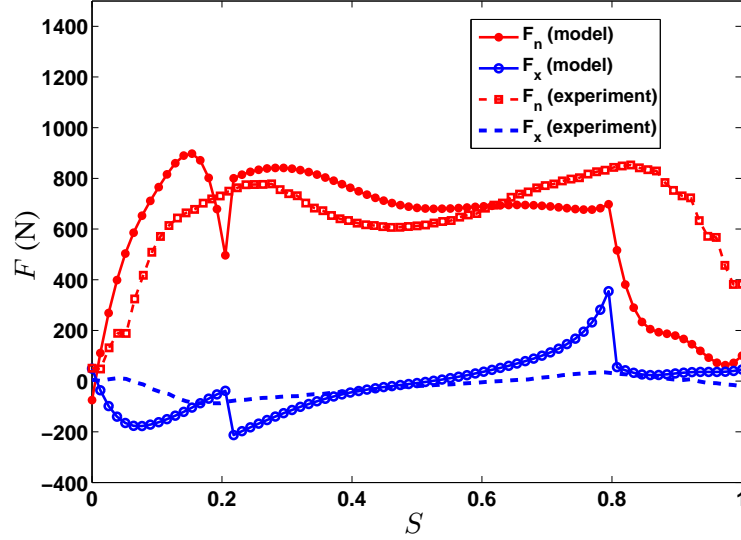
Figure 4.4: The GRF (F_n and F_x) of the stance leg during the walking gait without foot slip.

We next demonstrate the model prediction results for the slip recovery gait experiment. Figure 4.5(a) shows a video snapshot of the slip recovery gait. The human starts the normal gait with a single-stance phase (i.e., $\mathcal{S}_1$ in Fig. 4.2) at $t = 0$ s. At $t = 0.32$ s, the (left) swing leg touches down on the slippery floor and then starts slipping. At this moment, the (right) foot is still in touch with the floor without slip and the human gait lies in the double-stance slip phase ($\mathcal{S}_4$). Then at $t = 0.61$ s, the (right) swing foot leaves the ground (toe-off) and the (left) stance foot still slips. Therefore, the gait enters the single-stance slip phase ($\mathcal{S}_3$). The walker quickly realizes and reacts to slip event. At $t = 0.96$ s the (right) swing foot touches down, the (left) stance foot leaves the ground and the gait becomes a recovered single-stance phase without slipping ($\mathcal{S}_1$). Figure 4.5(b) shows the human skeleton data measured by the motion capture system and Fig. 4.5(c) demonstrates the skeleton constructed by the model predicted joint angles.

Figure 4.6 shows the seven joint-angle comparison results of the model prediction and the measurements by the motion capture system. The results clearly confirm that the model prediction follows the experiments closely in the entire gait recovery process.

(a)

(b)

(c)

$t = 0.01\text{s}$ $t = 0.16\text{s}$ $t = 0.28\text{s}$ $t = 0.35\text{s}$ $t = 0.56\text{s}$ $t = 0.60\text{s}$ $t = 0.69\text{s}$ $t = 0.78\text{s}$ $t = 0.87\text{s}$ $t = 0.96\text{s}$
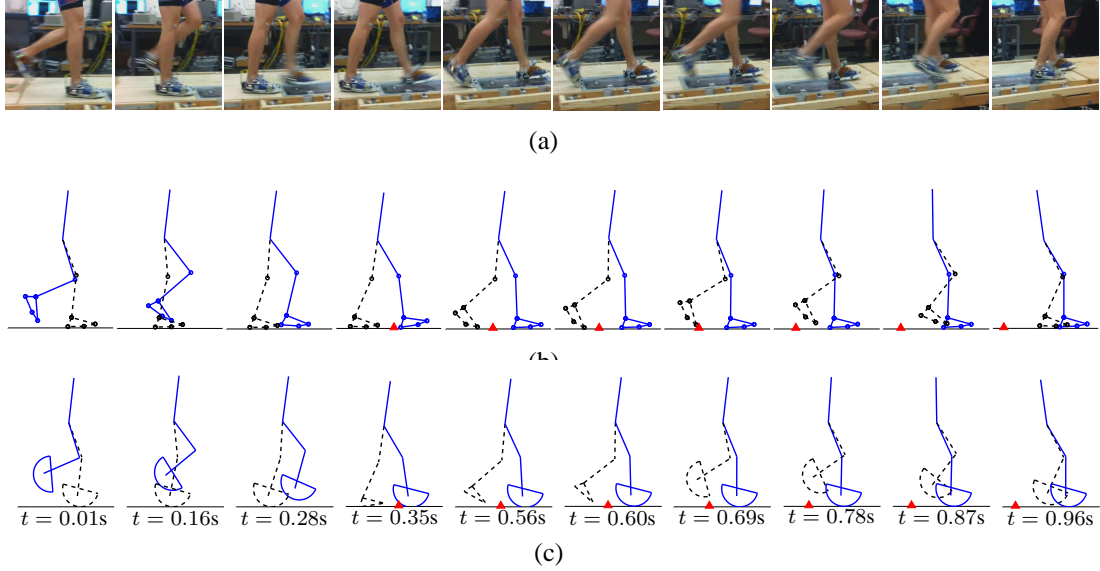
Figure 4.5: A snapshot of the recovery human gait from foot slip. (a) Video snapshot. (b) Human 7-link skeleton from the optical motion capture system. The empty-circle dots indicate the reflective optical marker locations. (c) Skeleton prediction by the bipedal model. In (b) and (c), a red triangle is plotted to indicate the location where the left leg starts slipping.

Figure 4.6(h) shows the slipping distance comparison and again, the model prediction follows the experiment. Figures 4.7(a) and 4.7(b) show the normal and tangential GRF for the both feet. The GRF comparison clearly show that except the double-stance slip case during $t = 0.32$ s to 0.61 s, the normal and tangential GRF predictions match the measurements. However, during the double-stance slip period, the force prediction are not accurate. We are currently working on improvement of these double-stance force calculations. Figure 4.7(c) shows the coefficient of friction (COF) of the stance-foot contact during the slip recovery process. Before slips start (around 0.32 s), the required (actual) COF lies in a range of $|\mu| < 0.2$, which is far less than the available foot-floor friction coefficient (measured as close to 1 of the dry rubber-wood contact [32]). At $t = 0.32$ s, the available COF is less than 0.05 due to the soap film on surface. As shown in Fig. 4.7(c), the required COF is nearly constant around $\mu = 0.05$, which is higher than the available COF. Therefore, slip starts when the foot touches down at that moment.
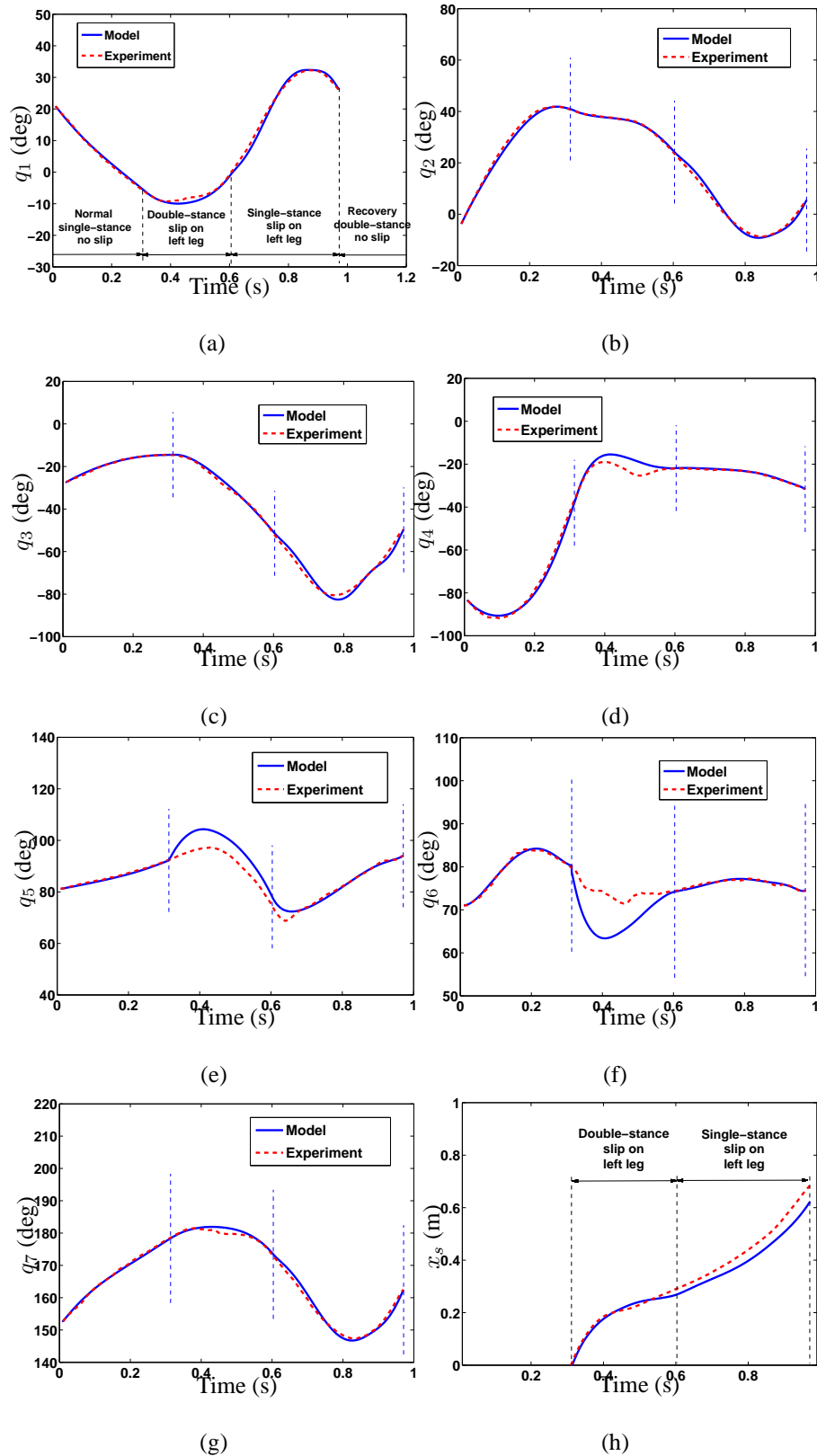
Figure 4.6: (a)-(g): Joint angle (q_1 to q_7) comparisons between the model prediction and the experiments during slip recovery gait. The solid lines represent the model predictions and the dash lines show the experimental data. (h) Slipping distance x_s of the (left) stance leg during the slip recovery experiment.
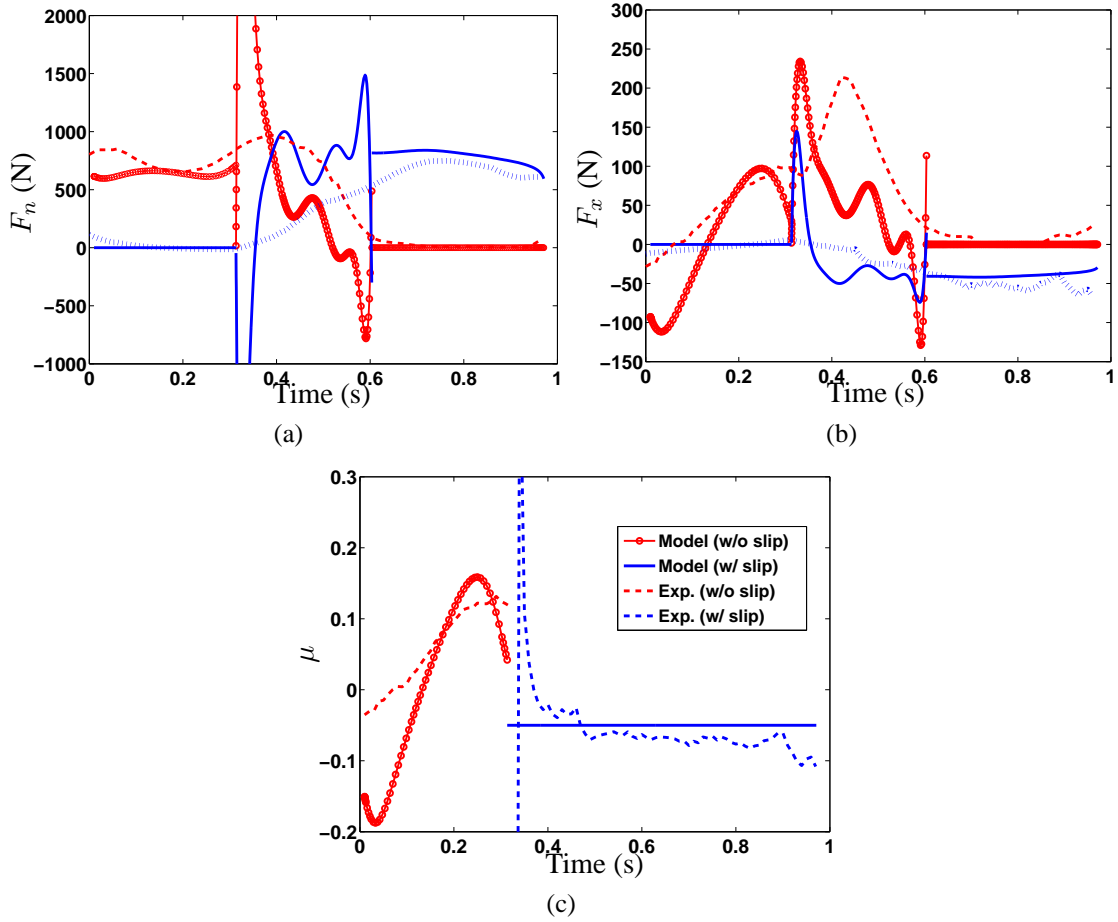
Figure 4.7: Comparison results of the GRF and friction coefficient during the slip recovery. (a) Normal GRF F_n. (b) Tangential GRF F_x. (c) Friction coefficient μ of the stance leg foot. In (a) and (b), the model prediction forces for the left- and right legs are plotted as the blue solid and red circle lines, respectively, and the experiments are plotted as the blue dotted and the red dash lines. In (c), the model predicted and experimental μ in non-slip phase is plotted by the red empty circle and the dash lines, respectively, and these in the slip phase by the blue solid and dash lines, respectively.

4.5 Conclusions

In this chapter, we presented a robotic bipedal dynamic model for human walking gait with foot slips. We relaxed the non-slip assumption used in the existing bipedal robotic models and consider the cases when the foot slips on the ground. A general hybrid bipedal model and the gait controllers were developed for human walking with

foot slips. Experiments were conducted using the wearable force sensors to capture the ground reaction forces during the normal no-slip walking and the slipping recovery gaits. The comparison results confirmed that the model prediction match the experiments for not only the joint angles but also the ground reaction forces, which has not been reported previously. The new bipedal model can be potentially used for developing assistive robotic systems to prevent human from falling due to slips.

Chapter 5

Slip Detection in Human Walking Using Wearable Sensors

5.1 Introduction

Slip detection during human walking is challenging because of the highly unpredictable, uncontrollable, and fast-evolving slip dynamics. Human's response and corrective reactions to unexpected slips create additional complications for slip detection and prediction.

Inertial sensors such as inertial measurements unit (IMU) have been extensively used to successfully detect features of the normal walking gait [107]. Detection and identification of many walking motion and gait events, such as heel strike and heel off, are often built based on the integration of the wearable gyroscope and accelerometer measurements [108–112]. These wearable devices are commonly attached on the shank, the thigh or at the foot. In a recent paper [113], wearable sensors are used for real-time gait event detection. However, these studies do not consider the foot slip in walking gait.

The goal of this chapter is to present an ambulatory slip detection sensing system and a slip detection and prediction algorithm. The proposed slip detection algorithm is built on a dynamic model of the foot slip and requires no knowledge about the subject's specific gait parameters a priori. The slip dynamic model is inspired and obtained from the bipedal walking model presented in [72]. The use of the slip dynamics model enables us to integrate the kinematic sensing measurements and the physical walking

constraints. Only a set of wearable IMUs attached to the lower limbs are used for slip detection and prediction. One attractive feature of the proposed approach is its instantaneous, accurate slip detection and prediction capability. The fast slip detection is also critical for design of assistive and rehabilitation devices used to assist human for balance recovery and to reduce and prevent the possibility of falls.

The remainder of the chapter is organized as follows. Section 5.2 describes the wearable sensing systems for slip detection. We present the slip dynamics in Section 5.3 and then the slip detection algorithm in Section 5.4. Section 5.5 presents the experimental results. Finally, we present the concluding summary in Section 5.6.

5.2 Slip detection using wearable sensing systems

Figure 5.1 shows the integrated sensing suite for slip detection and monitoring system [32]. The sensing suite consists of two sets of the sensors: (1) a set of lower-limb wearable motion sensors and (2) an insole force/torque sensor suite.

Five small IMU units (model slimAHRS from Motion Sense Inc.) are attached to each lower limb. Each IMU unit consists of a tri-axial gyroscope, a tri-axial accelerometer and three magnetometers to measure the three attitude angles. Each set of two rigid-mounted IMUs are attached to the thigh and the shank segments. The main reason to use two IMUs on one body segment is to directly obtain the real-time angular acceleration information from the accelerometer measurements without the need of numerical differentiation [114]. We designed and fabricated a wireless module for each IMU unit to transmit the motion data in real time. To provide ground truth of the human movements, an optical motion capture system (8 Bonita cameras from Vicon Inc.) is used in the experiments.

Two six degree-of-freedom (6-DOF) force/torque sensors (model SS-1 from INSENCO Co., Ltd) are used to measure the shoe-floor interactions. These sensors are located
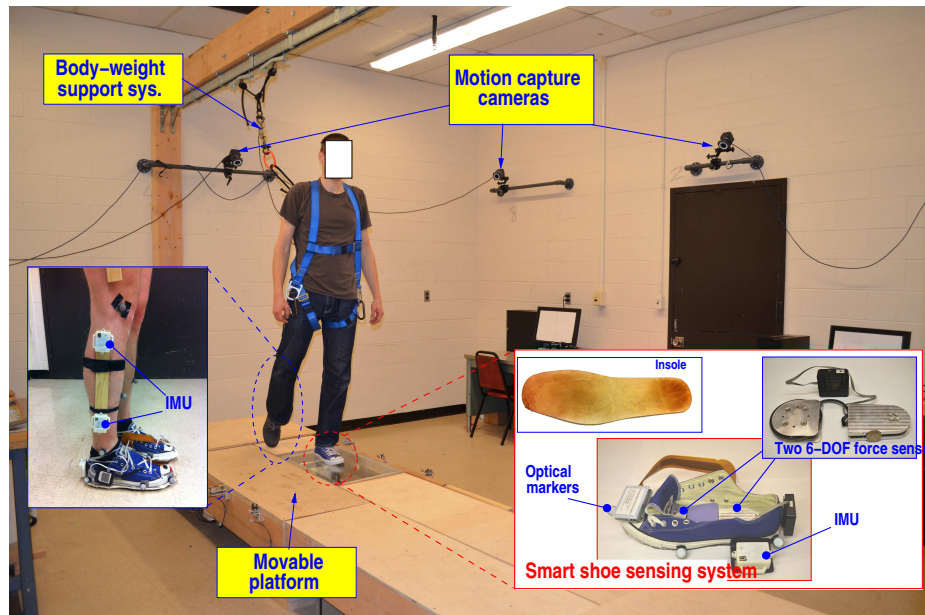
Figure 5.1: The slip detection and monitoring system with kinematics/kinetics/force sensors.

inside the shoes to measure the total 3D forces and torques at the forefoot and the hindfoot locations; see Fig. 5.1. The use of these force sensors is purely to provide validation of the model development, whereas the slip detection and prediction algorithms do not use any force measurements. A real-time embedded system (CompactRIO from National Instruments Inc.) is used to sample and process measurements from all force sensors and the wearable sensors at a frequency of 100 Hz. The data collections between the optical motion capture and the CompactRIO are synchronized through an analog signal triggering connection between them.

To help create slip during human walking, we build a wooden platform as shown in Fig. 5.1. The human subjects walk on the platform in the laboratory. The human subjects are first asked to perform normal walking on the platform to become familiar with the setup and then they repeat the experiments with reduced coefficients of friction on the platform by manually applying soap films on the surface at certain locations. These reduced-friction locations are not noticeable to the subjects and therefore, the walking styles in these tests are considered the same as the normal walking without

slip. More detailed discussions about the experimental protocols and results will be presented in Section 5.5.

5.3 Slip model and estimation

5.3.1 System configuration

A simplified bipedal model is used in this work to characterize human walking with slip. Due to the fact that slip is most commonly initiated from one foot, we herein present only single-foot slip dynamics.

The slip model describes the dynamic relationship among the slip variables, such as the slip displacement and other human gait parameters. Because of the symmetry and repetitive patterns in bipedal walking, we consider a two-link limb structure as shown in Fig. 5.2. The four-DOF limb structure is described by two (absolute) joint angles q_1 (shank) and q_2 (thigh) with a locked ankle joint. The clockwise direction of these angles are defined as positive values. The foot-floor contact point C_l of the leading stance leg is considered under slip with coordinate (x_s, y_s) in a local frame $\mathcal{B}$. Frame $\mathcal{B}$ is attached at the heel of the stance leg and the coordinates are reset to the location of the new stance leg's initial foot contact at each step. A ground-fixed inertial frame $\mathcal{I}(X, Y)$ is defined and axes of frames $\mathcal{B}$ and $\mathcal{I}$ are aligned.

Figure 5.2(a) shows the two-link double inverted pendulum for the slipping leg. Link 1 represents the shank and the foot together with mass M_1, length L_1, and mass moment of inertia J_1 about its mass center. The mass center is located at a distance of a_1 from C_l. Link 2 represents the thigh and the rest of the body with mass M_2, mass moment of inertia J_2 about its mass center, and length L_2. The mass center of link 2 is assumed at the hip, namely, close to the human's COM. The heel position (x_s, y_s) of the stance leg in $\mathcal{B}$ captures the slip displacement. The generalized coordinates of the slip dynamics is then defined as $\boldsymbol{q} = [\boldsymbol{q}_l^T \ x_s \ y_s]^T$, where $\boldsymbol{q}_l = [q_1 \ q_2]^T$. The contact
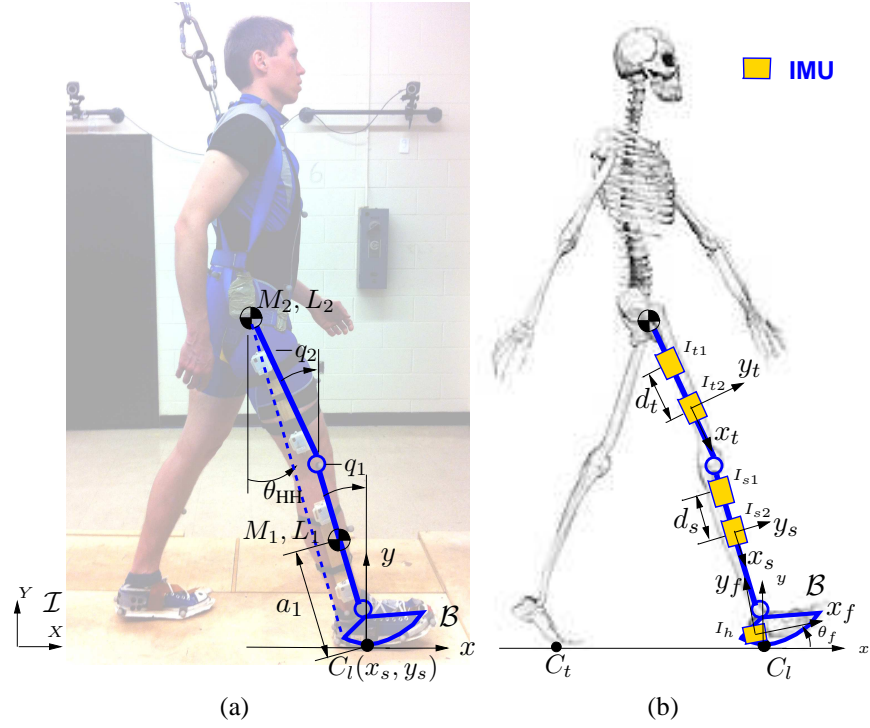
Figure 5.2: (a) Schematic of a 2-link, 4-DOF model for slip prediction. (b) The wearable IMU configuration.

force at C_l is denoted as vector $\boldsymbol{F} = [F_t \ \ F_n]^T$, where F_t and F_n are the friction and normal forces, respectively.

The positions of all IMUs are shown in Fig. 5.2(b). The x-axis of the IMUs attached to the thigh, the shank and the foot heel are aligned with the corresponding link segments, respectively. The y-axis of each IMU is perpendicular to its x-axis in the sagittal plane. We denote the IMUs attached to the thigh, the shank, and the heel as I_{t_i}, I_{s_i}, $i = 1, 2$, and I_h, respectively. The distances between the two IMUs attached to the thigh and the shank are denoted as d_t and d_s, respectively.

5.3.2 Slip dynamics

With the above configuration and setup, the position vectors for the two links are respectively obtained as

$$\boldsymbol{r}_1 = \begin{bmatrix} x_s + a_1 \, \mathrm{s}_{q_1} \\ y_s + a_1 \, \mathrm{c}_{q_1} \end{bmatrix}, \ \boldsymbol{r}_2 = \begin{bmatrix} x_s + L_1 \, \mathrm{s}_{q_1} + L_2 \, \mathrm{s}_{q_2} \\ y_s + L_1 \, \mathrm{c}_{q_1} + L_2 \, \mathrm{c}_{q_2} \end{bmatrix},$$

where $\mathrm{s}_{q_1} := \sin q_1$, $\mathrm{c}_{q_1} := \cos q_1$ for q_1 and other angles. The kinetic energy of the 2-link limb is then

$$T = \frac{1}{2} \sum_{i=1}^{2} M_i \dot{\boldsymbol{r}}_i^T \dot{\boldsymbol{r}}_i + \frac{1}{2} \sum_{i=1}^{2} J_i \dot{q}_i^2.$$

The potential energy V is expressed as

$$V = g \left[M_1 (y_s + a_1 \, \mathrm{c}_{q_1}) + M_2 (y_s + L_1 \, \mathrm{c}_{q_1} + L_2 \, \mathrm{c}_{q_2}) \right],$$

where g is the gravitational constant. Using Lagrangian equation, we obtain the equations of motion as

$$\boldsymbol{D}_d(\boldsymbol{q}_l)\ddot{\boldsymbol{q}} + \boldsymbol{C}_d(\boldsymbol{q}_l, \dot{\boldsymbol{q}}_l)\dot{\boldsymbol{q}} + \boldsymbol{G}_d(\boldsymbol{q}_l) = \boldsymbol{B}_d u + \boldsymbol{E}_d^T \boldsymbol{F}, \tag{5.1}$$

where $\boldsymbol{D}_d(\boldsymbol{q}_l)$, $\boldsymbol{C}_d(\boldsymbol{q}_l, \dot{\boldsymbol{q}}_l)$, $\boldsymbol{G}_d(\boldsymbol{q}_l)$ and $\boldsymbol{B}_d$ are the inertia, Coriolis, gravity and input mapping matrices, respectively, $u = \tau_k$ as the knee joint torque, and matrix $\boldsymbol{E}_d = [\frac{\partial \boldsymbol{p}_2(\boldsymbol{q})}{\partial \boldsymbol{q}}]^T \in \mathbb{R}^{2 \times 4}$ describes the contact constraints [72], with $\boldsymbol{p}_2(\boldsymbol{q}) \in \mathbb{R}^2$ being defined as a slip vector of a contact point C_l in frame $\mathcal{B}$. Only the knee joint is assumed to be actuated. The details of these matrices are given in (5.2) on the top of the next page.

Taking the third equation from (5.1), we obtain

$$\ddot{x}_s = \frac{M_a \left(\mathrm{s}_{q_1} \, \dot{q}_1^2 - \ddot{q}_1 \, \mathrm{c}_{q_1} \right) + M_2 L_2 (\mathrm{s}_{q_2} \, \dot{q}_2^2 - \ddot{q}_2 \, \mathrm{c}_{q_2}) + F_t}{M}, \tag{5.3}$$

where $M = M_1 + M_2$ and $M_a = M_1 a_1 + L_1 M_2$. The result in (5.3) implies that the slip acceleration is obtained directly using the measurements of the kinematic and kinetic data. Slip velocity $\dot{x}_s$ and displacement x_s can then be obtained by direct integration of (5.3). The results by direct integration however require precise knowledge of the initial slip displacement and velocity. Obtaining these initial values is not straightforward and instead, we present a filter-based estimation scheme.

$$\boldsymbol{D}_d(\boldsymbol{q}_l) = \begin{bmatrix} M_2L_1^2 + M_1a_1^2 + J_1 & M_2L_1L_2\,\mathrm{c}_{q_1-q_2} & (M_2L_+M_1a_1)\,\mathrm{c}_{q_1} & -(M_2L_1+M_1a_1)\,\mathrm{s}_{q_1} \\ M_2L_1L_2\,\mathrm{c}_{q_1-q_2} & M_2a_2^2 + J_2 & M_2L_2\,\mathrm{c}_{q_2} & -M_2L_2\,\mathrm{s}_{q_2} \\ (M_1a_1 + M_2L_1)\,\mathrm{c}_{q_1} & M_2L_2\,\mathrm{c}_{q_2} & M_1 + M_2 & 0 \\ -(M_1a_1 + M_2L_1)\,\mathrm{s}_{q_1} & -M_2L_2\,\mathrm{s}_{q_2} & 0 & M_1 + M_2 \end{bmatrix},$$

$$\tag{5.2a}$$

$$\boldsymbol{C}_d(\boldsymbol{q}_l,\dot{\boldsymbol{q}}_l) = \begin{bmatrix} 0 & \dot{q}_2M_2L_1L_2\,\mathrm{s}_{q_1-q_2} & 0 & 0 \\ -\dot{q}_1M_2L_1L_2\,\mathrm{s}_{q_1-q_2} & 0 & 0 & 0 \\ -\dot{q}_1(M_1a_1 + M_2L_1)\,\mathrm{s}_{q_1} & -\dot{q}_2M_2L_2\,\mathrm{s}_{q_2} & 0 & 0 \\ -\dot{q}_1(M_1a_1 + M_2L_1)\,\mathrm{c}_{q_1} & -\dot{q}_2M_2L_2\,\mathrm{c}_{q_2} & 0 & 0 \end{bmatrix},$$

$$\tag{5.2b}$$

$$\boldsymbol{G}_d(\boldsymbol{q}_l) = \begin{bmatrix} -g(M_1a_1 + M_2L_1)\,\mathrm{s}_{q_1} \\ -gM_2L_2\,\mathrm{s}_{q_2} \\ 0 \\ g(M_1 + M_2) \end{bmatrix}, \quad \boldsymbol{E}_d = \begin{bmatrix} 0 & 0 \\ 0 & 0 \\ 1 & 0 \\ 0 & 1 \end{bmatrix}, \quad \boldsymbol{B}_d = \begin{bmatrix} -1 \\ 1 \\ 0 \\ 0 \end{bmatrix}, \tag{5.2c}$$

5.3.3 Extended Kalman Filter (EKF)-based slip estimation

From the system configuration, we obtain the kinematic models for the IMU gyroscopes attached to the thigh and the shank as [106, 115]

$$\dot{q}_1 = \begin{bmatrix} 0 & 0 & 1 \end{bmatrix} \boldsymbol{\omega}_s =: \omega_{sz}, \ \dot{q}_2 = \begin{bmatrix} 0 & 0 & 1 \end{bmatrix} \boldsymbol{\omega}_t =: \omega_{tz}, \tag{5.4}$$

where $\boldsymbol{\omega}_s$ (ω_{sz}) and $\boldsymbol{\omega}_t$ (ω_{tz}) are the IMU gyroscope (z-axis component) measurements attached to the shank and the thigh, respectively. We define the EKF state variables $\boldsymbol{x} = [x_1\ x_2\ x_3\ x_4]^T = [x_s\ \dot{x}_s\ q_1\ q_2]^T$ and write the state dynamics from (5.3) and (5.4) as follows.

$$\dot{\boldsymbol{x}} = \boldsymbol{f}(\boldsymbol{x}, \boldsymbol{w}) = \begin{bmatrix} x_2 \\ f_s(\boldsymbol{x}, \boldsymbol{w}) \\ \omega_{sz} \\ \omega_{tz} \end{bmatrix}, \tag{5.5}$$

where

$$f_s(\boldsymbol{x}, \boldsymbol{w}) = \frac{M_a\big(\mathrm{s}_{x_3}\,\omega_{sz}^2 - \alpha_s\,\mathrm{c}_{x_3}\big) + M_2L_2\big(\mathrm{s}_{x_4}\,\omega_{tz}^2 - \alpha_t\,\mathrm{c}_{x_4}\big)}{M}, \tag{5.6}$$

$\boldsymbol{w} = [\omega_{sz}\ \omega_{tz}\ a_{s_1y}\ a_{s_2y}\ a_{t_1y}\ a_{t_2y}\ a_{hx}]^T$, a_{s_iy} and a_{t_iy}, $i = 1, 2$, are the y-axis component of the ith IMU accelerometer measurements attached to the shank and the thigh,

respectively, and a_{hx} is the x-axis component of the heel IMU accelerometer measurement. Inclusion of a_{hx} into $\boldsymbol{w}$ is mainly due to the EKF output construction discussed later in this section. In (5.6), α_s and α_t are the angular accelerations of the shank and the thigh, respectively and are calculated by using the linear accelerations, namely,

$$\alpha_i = \frac{a_{i_2 y} - a_{i_1 y}}{d_i}, i = s, t. \tag{5.7}$$

Remark 5.1. *Compared with the slip dynamics (5.3), EKF dynamics equation $\dot{x}_2 = \ddot{x}_s = f_s(\boldsymbol{x}, \boldsymbol{w})$ in (5.5) drops the friction force F_t term. The rationale for such approximation are two-folds. First, as demonstrated through experimental results in Section 5.5, the magnitude of force F_t during foot slip is small and can be neglected without sacrificing estimation accuracy. Second, obtaining F_t needs wearable force sensors and it is desirable to avoid using these expensive sensors for slip detection applications.*

Three outputs are considered in the EKF design. First, the accelerometer at the heel directly provides the acceleration measurement along the x-axis in $\mathcal{B}$. Once the heel touches down, the foot is almost aligned with the floor and therefore, we approximate the heel acceleration as

$$y_1 = \ddot{x}_s = \begin{bmatrix} 1 & 0 & 0 \end{bmatrix} \boldsymbol{a}_h =: a_{hx}, \tag{5.8}$$

where $\boldsymbol{a}_h \in \mathbb{R}^3$ is the heel accelerometer measurement. The second output of the EKF design is obtained by the kinematic constraint given by the 2-link lower-limb model. As shown in Fig. 5.2(b), we express the heel velocity along the x-axis of $\mathcal{B}$ as

$$y_2 = h_s(\boldsymbol{x}, \boldsymbol{w}) = \dot{x}_s - v_x^{\text{Hip}} + L_1 \dot{q}_1 \, \mathrm{c}_{q_1} + L_2 \dot{q}_2 \, \mathrm{c}_{q_2} = 0, \tag{5.9}$$

where v_x^{Hip} is the velocity of the hip along the x-axis of $\mathcal{B}$. The direct measurement of v_x^{Hip} is not available and we estimate its value by considering the entire walking stance prior to the slip heel strike. During a non-slip stance phase, the horizontal

velocity of the heel is almost zero. Considering the fact that the hip horizontal velocity during normal walking is almost constant, we reversely compute v_x^{Hip} during the non-slip stance phase by setting $\dot{x}_s = 0$ and using the relationship in (5.9). The third output uses the kinematic relationship between the position of the hip and the heel along the x-axis of $\mathcal{B}$ as

$$y_3 \quad = \quad g_s(\boldsymbol{x}, \boldsymbol{w}) = x_s - v_x^{\text{Hip}} \Delta t + L_1 \left(\mathrm{s}_{q_1} - \mathrm{s}_{q_1^0} \right) + L_2 \left(\mathrm{s}_{q_2} - \mathrm{s}_{q_2^0} \right) = 0, \quad (5.10)$$

where Δt is the time elapsed from the heel-strike moment and initial joint angles q_1^0 and q_2^0 at the time of the heel strike can be approximated by using the wearable IMUs [116]. With the above three output equations we confirm that the observability matrix of the system is full rank and thus observable.

With the above discussion, we write the EKF output equation as

$$\boldsymbol{y} = \boldsymbol{h}(\boldsymbol{x}, \boldsymbol{w}) + \boldsymbol{n}_y = \begin{bmatrix} f_s(\boldsymbol{x}, \boldsymbol{w}) \\ h_s(\boldsymbol{x}, \boldsymbol{w}) \\ g_s(\boldsymbol{x}, \boldsymbol{w}) \end{bmatrix} + \boldsymbol{n}_y, \quad (5.11)$$

where $\boldsymbol{n}_y \sim \mathcal{N}(\boldsymbol{0}, \Sigma_y)$ is the white noise with variance matrix Σ_y. Given system equation (5.5) and output equation (5.11), we calculate Jacobian matrices $\boldsymbol{F}_{EKF} = \frac{\partial \boldsymbol{f}}{\partial \boldsymbol{x}}\big|_{\boldsymbol{x}, \boldsymbol{u}}$ for the state dynamics and $\boldsymbol{H}_{EKF} = \frac{\partial \boldsymbol{h}}{\partial \boldsymbol{x}}\big|_{\boldsymbol{x}, \boldsymbol{u}}$ for the outputs at each iterative step. The EKF design is similar to that in [117] and we here omit the details.

5.4 Slip detection algorithm

The estimates of the slip displacement in the previous section are accurate only once the foot slip starts. To use these estimates, we need to detect foot slip in real time. Since foot slip commonly happens at the beginning of the heel-strike, we here focus on the slip detection algorithm that determines the slipping status right after the heel strike.

5.4.1 Slip indicator

An important indication about the foot slip can be assessed by the movement of the human COM in the sagittal plane. The COM movement is indirectly related to hip-heel angle θ_{HH}, which is the (absolute) angle of the vector formed by connecting the human COM and the stance leg heel position in the sagittal plane; see Fig. 5.2(a). To approximate θ_{HH}, we use the measurements of the wearable IMUs attached to the upper thigh (I_{t1}) and the heel (I_h).

Considering that slip acceleration $\ddot{x}_s$ directly indicates the foot slip, we propose a slip indicator $S_I(t)$

$$S_I(t) = \frac{\ddot{x}_s}{\beta^{(\ddot{\theta}_{\mathrm{HH}} - \gamma)}}, \tag{5.12}$$

where β and γ are constants. The use of the exponential function form in (5.12) primarily enhances the distinction of the ratio of $\ddot{x}_s$ and $\ddot{\theta}_{\mathrm{HH}}$ for the slip and non-slip cases. Moreover, it helps to avoid the division of potentially tiny or near-zero value of $(\ddot{\theta}_{\mathrm{HH}} - \gamma)$. The slip detection algorithm relies on setting a threshold for $S_I(t)$. As suggested in [118], using the threshold technique can minimize the computational load and the number of used sensor components.

A threshold S_s for $S_I(t)$ is used to determine the foot slip: slip is declared whenever $S_I(t)$ exceeds the threshold value S_s (i.e., $S_I(t) \geq S_s$); otherwise no slip is identified (i.e., $S_I(t) < S_s$). The value of the threshold S_s is determined by experiments and will be discussed in details in Section 5.5.3. The calculation of $S_I(t)$ requires knowledge of instantaneous $\ddot{\theta}_{\mathrm{HH}}$ and $\ddot{x}_s$. The estimates of $\ddot{x}_s$ are directly measured by using the heel accelerometer I_h. To compute $\ddot{\theta}_{\mathrm{HH}}$, we adopt a similar approach as in (5.7) and use the accelerometers attached at the upper thigh (close to the hip) and at the heel, that is,

$$\ddot{\theta}_{\mathrm{HH}} = \frac{a_{t_1 y} - a_{hx}}{l_{\mathrm{HH}}}, \tag{5.13}$$

where $a_{t_1 y}$ and a_{hx} are the y-axis and x-axis acceleration measurements of I_{t1} and I_h, respectively, and l_{HH} is the distance between I_{t1} and I_h. In (5.13), we approximate the

calculation with the small angle and constant l_{HH} assumptions.

5.4.2 Slip detection and estimation algorithm

The flowchart of the slip detection and estimation algorithm is illustrated in Fig. 5.3. The slip detection and monitoring begins at the heel-strike moment. We adopt a similar approach as in [111] for detecting the heel-strike event by checking the first peak of the shank angular velocity. The calculation of $S_I(t)$ and the EKF prediction algorithm starts simultaneously. When $S_I(t) \geq S_s$, foot slip is detected (i.e., `flag= 1`) and the information of the slip is obtained from the EKF prediction. It is expected that the human sensory and voluntary reactive slip recovery response takes place after at least 200 ms [119] and therefore, we use a time period of 400 ms (twice of the voluntary recovery time) to terminate the EKF prediction.
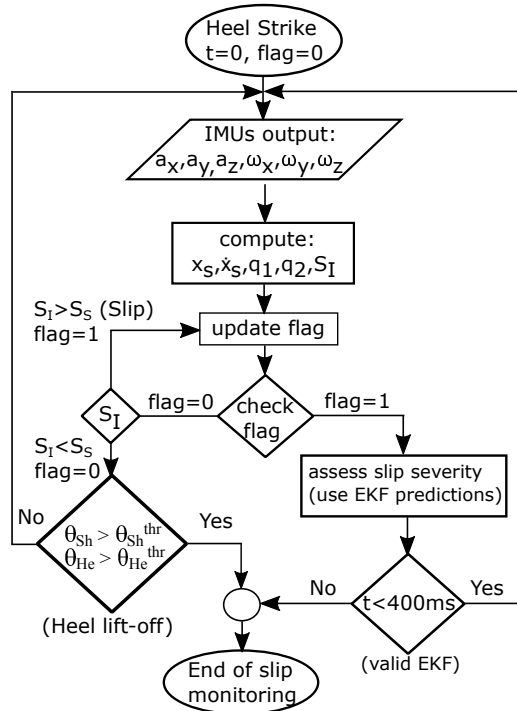
Figure 5.3: Block diagram of the schematics of slip detection algorithm.

If the value of the slip indicator is less than the threshold, namely, $S_I(t) < S_s$,

no slip is detected (i.e., `flag= 0`) and in this case, the detection process is repeated until the detection of the heel-off event. Heel angle θ_{He} and shank angle θ_{Sh} are used to determine the foot heel-off event. The threshold value $\theta_{\mathrm{Sh}}^{\mathrm{thr}}$ is chosen as the mean value of the relative shank angle at 50% of stance of all subjects in the experiments. The threshold value $\theta_{\mathrm{He}}^{\mathrm{thr}}$ of the heel angle is taken the same as that in [108]. The details of how to obtain these angles and their threshold values will be presented in the next section.

5.5 Experiments

In this section, we first describe the experimental protocol, then present the experimental results to validate and demonstrate the slip detection algorithms and at the end we provide the discussions about the results.

5.5.1 Experimental protocols

Eight subjects (4 males and 4 females with ages: 26.3 ± 2.1 years, heights 1.73 ± 0.04 m, and weights 62.8 ± 7.8 kg) were recruited for the slip detection experiments and studies. All of the participants were reported to be in a good health condition. An informed consent form was signed by all the subjects and the testing protocol was approved by the Institutional Review Board (IRB) at Rutgers University.

In the experiments, the subjects were asked to walk on the wooden platform with their normal walking speeds (within a range of 1.0 to 1.7 m/s) and to look straight ahead. The subjects in the experiments wore the slip detection wearable sensing system shown in Fig. 5.1 and the Vicon motion capture system provided the ground truth movement information. The subjects were asked to walk several minutes on the platform before the soap film was manually applied on the acrylic surface on the platform

to create slippery, low friction coefficient surface conditions. The subjects were wearing a headset with a loud music of their choices and a pair of special glasses such that the lower half of the view was dimmed to prevent the subject from noticing the soap film on the acrylic plate. A safety harness was used to catch and protect the subjects in case of a fall.

All eight subjects managed to recover from the unexpected slips and return to the normal walking gait during the first experiment run. The results and analyses presented in the following sections only use the unexpected slip recovery data from all eight subjects.

5.5.2   Experimental results

Figure 5.4 shows a snapshot of the recovery gait during a severe slip [72] for one representative subject S1. The subject starts the normal gait with a single-stance phase. When touching down on the slippery floor (heel-strike), the right foot starts slipping ($t = 0$). At this moment, the left foot is still on the floor but about to swing up. The subject detects and reacts to the foot slip and the left foot quickly touches down on the floor ($t = 0.27$ s). The (right) slipping foot leaves the floor at around $t = 0.4$ s and then quickly touches down again at around $t = 0.46$ s. Finally, a following compensatory step recovers the subject to the normal walking gait. The bottom plots in Fig. 5.4 show the representation of the human skeleton generated from the motion capture data. The slipping distance is also marked in the figure.

The EKF prediction results for subject S1 are shown in Fig. 5.5. The estimated slip displacement (Fig. 5.5(a)) match the ground truth closely. The estimates of the lower-limb joint angles (Figs. 5.5(b) and 5.5(c)) also follow the ground truth. In the EKF implementation, we use one set of biomechanics parameters (e.g., limb lengths, masses etc.) for all subjects, rather than the measured values for each individual. This simplifies the implementation and also leads to the satisfactory prediction results.
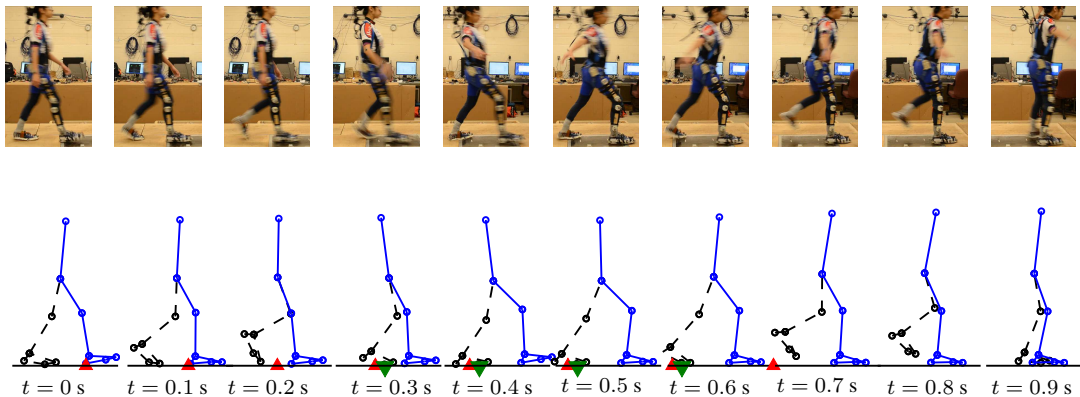
Figure 5.4: A snapshot of the recovery human gait from slip. The top figure shows the video snapshot and the bottom figure shows the human 7-link skeleton from the optical motion capture system. The "$\triangle$" and "∇" markers indicate respectively the locations where the right leg starts slipping and the left leg touches down the floor.

(a)

(b)

(c)
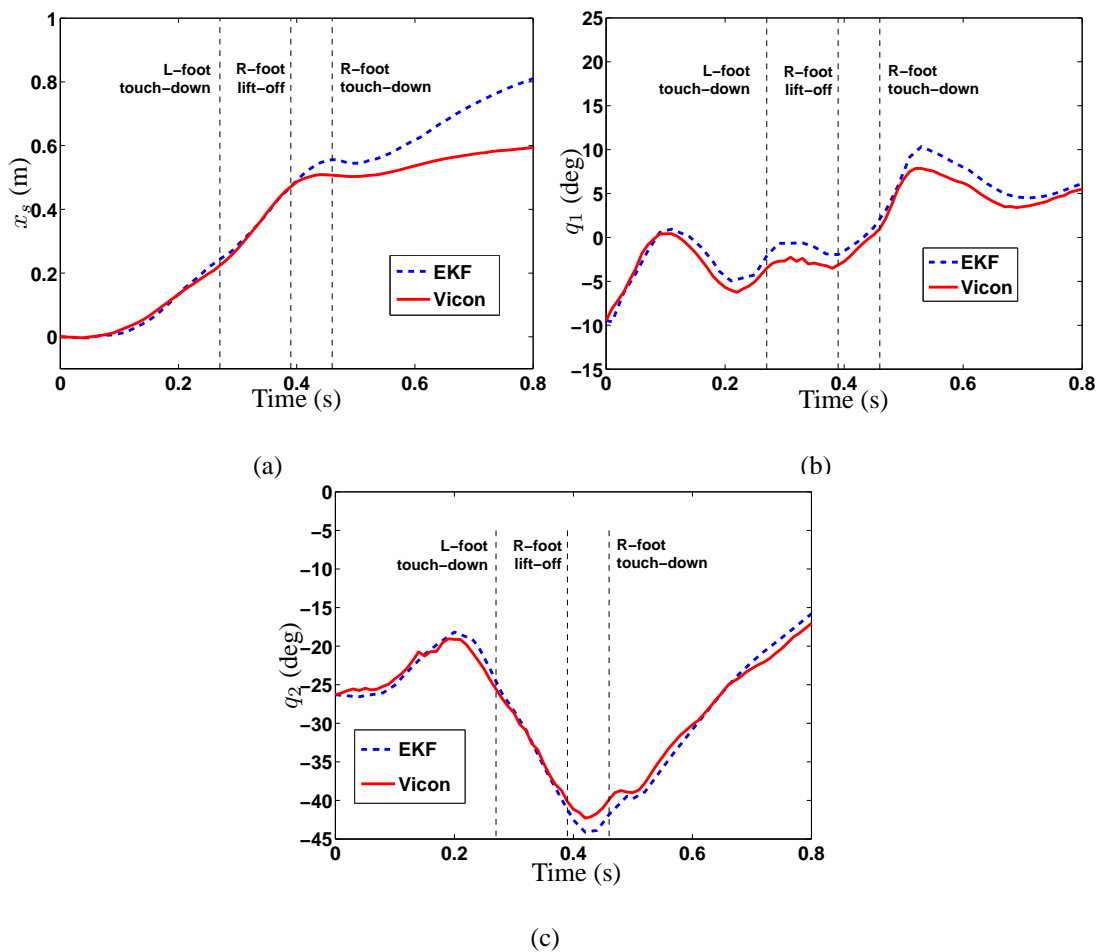
Figure 5.5: Comparison results of the EKF estimation and the ground truth under large foot slipping of subject S1. (a) Heel displacement x_s. (b) Shank joint angle q_1. (c) Thigh joint angle q_2.
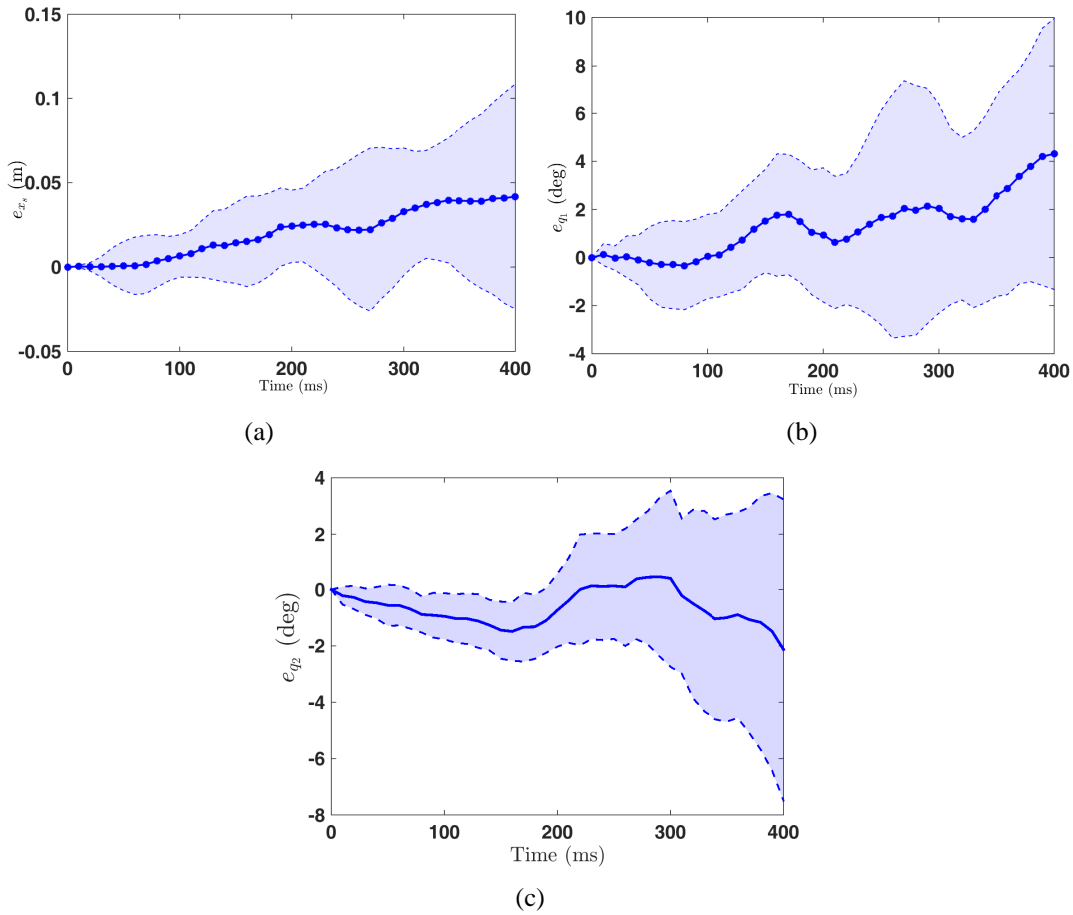
Figure 5.6: The EKF prediction errors for all eight subjects. The plots includes the error mean values (solid line) and the one standard deviation (dash lines). (a) Heel slip distance error e_{x_s}. (b) Shank angle error e_{q_1}. (c) Thigh angle error e_{q_2}.

The errors between the EKF predictions and the motion capture data for all eight subjects are shown in Fig. 5.6. The predicted slip displacements in Fig. 5.6(a) closely match the ground truth for the first 100 ms after the heel strike, with a mean error less than 2 cm. During the same period, the estimates of the lower-limb poses (Figs. 5.6(b) and 5.6(c)) also follow the ground truth. Discrepancies between the predicted and the ground truth values start to increase after 100 ms from the heel-strike event. The possible reasons for these discrepancies lie in the assumption of constant hip velocity and neglecting the friction force in the slip dynamics model.

The EKF-based heel displacement prediction for the normal walking without foot
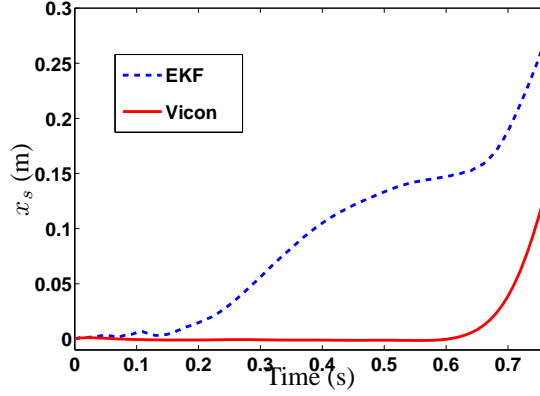
Figure 5.7: Comparison results of the EKF estimation and the ground truth of the heel displacement x_s under normal walking for subject S1.

slip for subject S1 is shown in Fig. 5.7. The prediction of the slip displacement x_s has a large discrepancy with the ground truth. The discrepancy possibly results from the neglection of the large friction force F_t in the slip model. Therefore, it is not appropriate to use the EKF predicted slip displacement x_s to determine the slip status and instead, the algorithm uses the slip indicator $S_I(t)$.

Figure 5.8 shows the slip indicator $S_I(t)$ over time for all eight subjects for both the normal walking (Fig. 5.8(a)) and the walking with foot slips (Fig. 5.8(c)). We also plot $S_I(t)$ over the gait stance in Fig. 5.8(b) to clearly observe the variations among all subjects. The calculation of $S_I(t)$ are based on only the IMU measurements. The choices of the values of parameters β and γ and threshold S_s will be discussed in Section 5.5.3. For comparison purpose, Fig. 5.9 shows the plots of $S_I(t)$ calculated from the Vicon motion capture measurements for all subjects. To compute $\ddot{\theta}_{\mathrm{HH}}$ and $\ddot{x}_s$ profiles, the motion capture marker position data were filtered using a 4th order low-pass Butterworth filter with a cutoff frequency of 6 Hz. Double numerical differentiation were then used to compute $\ddot{\theta}_{\mathrm{HH}}$ and $\ddot{x}_s$.

The results of normal walking in Figs. 5.9(a) and 5.8(a) show no detected slips (i.e., $S_I(t) < S_s$) and the values of $S_I(t)$ are close to zero until the heel-off event. The small values for $S_I(t)$ is mainly due to the fact that $\ddot{\theta}_{\mathrm{HH}}$ values are less than γ and the values
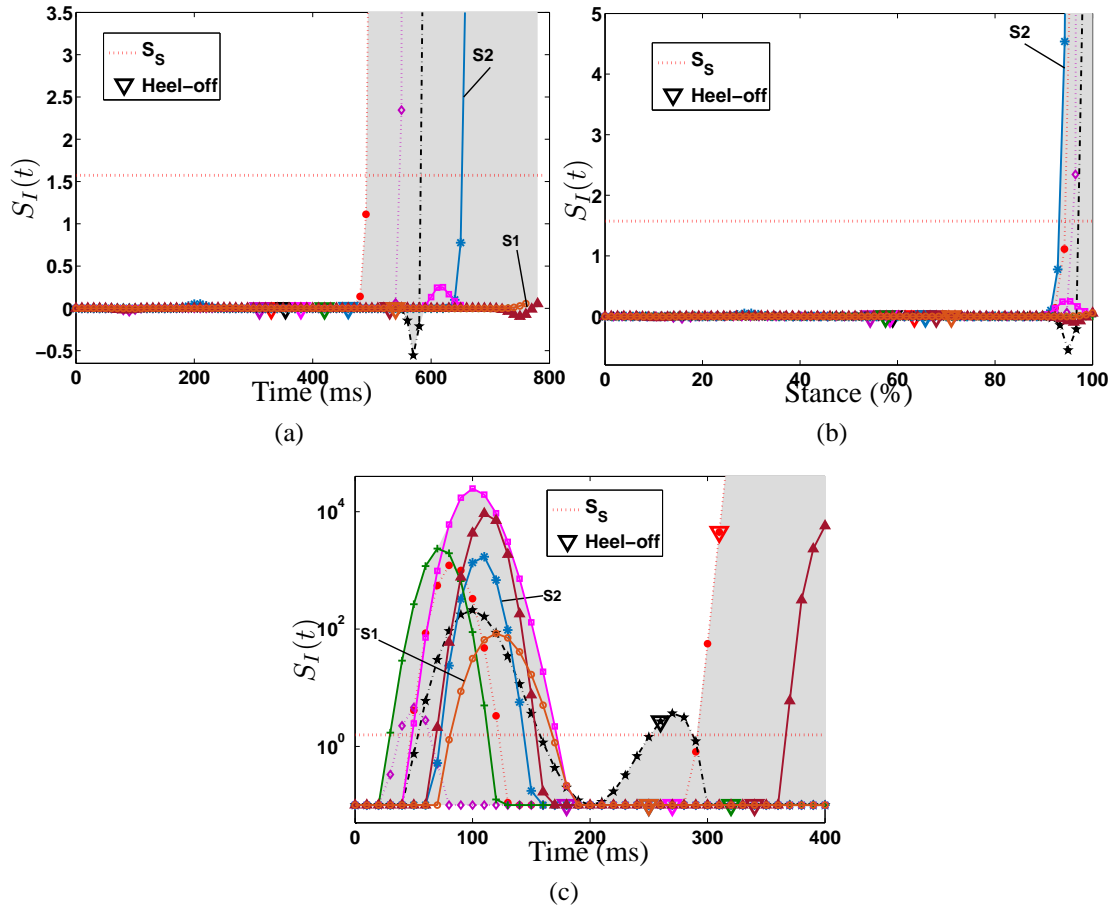
Figure 5.8: The slip indicator $S_I(t)$ calculated from the IMU data for all subjects. (a) Normal walking with gait progression time. (b) Normal walking normalized with the stance period. (c) Walking with slip. The horizontal dotted line in each figure indicates the threshold value $S_s = 1.57$. The marker "∇" in the normal working indicates the heel-off and in the slip walking indicates that the other foot touches down on the floor.

of $\ddot{x}_s$ are equal or smaller than zero. In Fig. 5.9(a), one subject has a high value of $S_I(t)$ (peak value close to 0.7) around $t = 50$ ms. This is due to a relatively small movement of the wooden platform and the foot (as observed and validated by the Vicon data). The plots of $S_I(t)$ over stance for normal walking in Figs. 5.8(b) and 5.9(b) clearly demonstrate the consistent performance of the slip indicator.

For walking with foot slip (Figs. 5.9(c) and 5.8(c)), the values of $S_I(t)$ exceed the threshold S_s shortly (less than 100 ms) after the heel strike, indicating the slip is detected. In the figure, we also plot the moment of the non-slip foot touch-down under
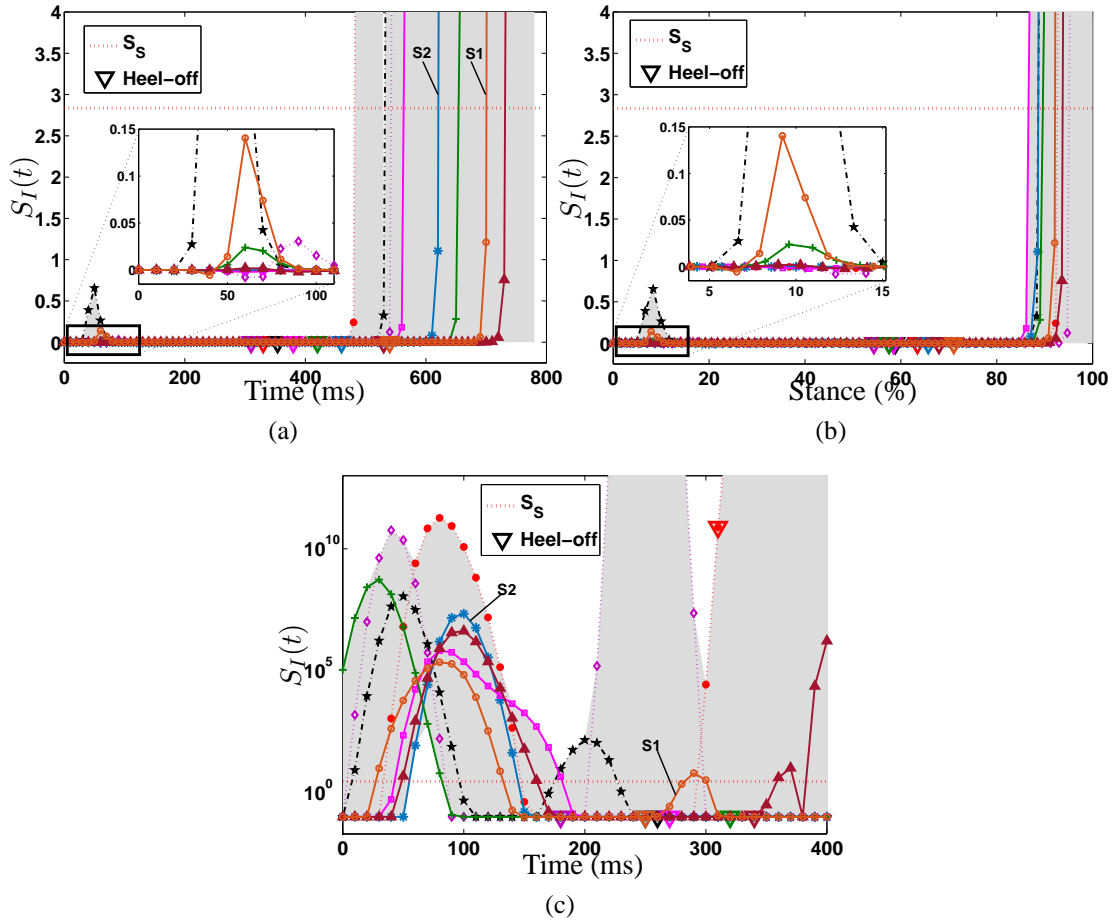
Figure 5.9: The slip indicator $S_I(t)$ calculated from the Vicon data for all subjects. (a) Normal walking with gait progression time. (b) Normal walking normalized with the stance period. (c) Walking with slip. The horizontal dotted line in each figure indicates the threshold value $S_s = 2.83$. The marker "$\bigtriangledown$" in the normal working indicates the heel-off and in the walking with slip indicates that the other foot touches down on the floor.

human recovery reaction. It is interesting to observe that it takes at least 180 ms after the slip starts and before the swing foot touches the floor. Figure 5.10 shows an inter-subject comparison of the slipping distances and the time durations from the heel strike until slip is detected by the algorithm. The results include the calculations using both the motion capture system and the IMU measurements. It is interesting to observe that the slipping distances using the motion capture data are almost all within 12 mm except for one at 50 mm. The detection times using the motion capture data are on or before 60 ms after the heel strike, while using the IMU data all slips were detected on
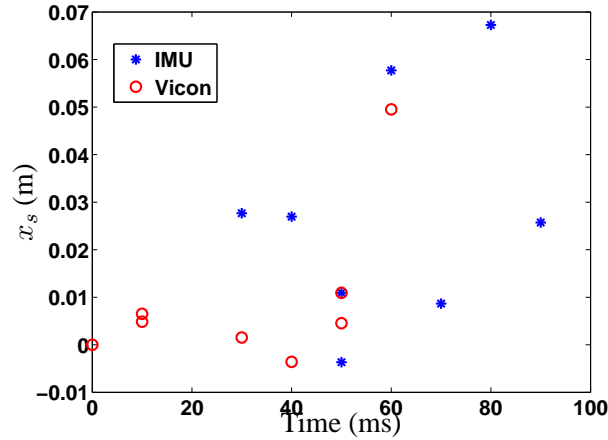
Figure 5.10: Comparison of the slip distance and the slip detection time after heel strike by the motion capture data and the IMU measurements.

or before 90 ms after the heel strike. Even using the IMU-based calculation, the slip detection time is several times faster than human voluntary reaction (around 200 ms after slip detection) [119]. The IMU-based slipping distances are under 30 mm except for two subjects at around 65 mm. Despite of the possible errors due to numerical approximations, the results obtained by the motion capture measurements show a highly consistent trend among all subjects and therefore, are taken as the benchmark.

To further illustrate the above-discussed gait differences, Fig. 5.11 shows the GRFs of the normal walking and the walking with slips. The plot includes the experiments from two subjects S1 and S2 and the slip indicators for these two subjects are also marked in Figs. 5.8 and 5.9. Figure 5.11(a) shows the normal force F_n and the friction force F_t for normal walking and Fig. 5.11(b) for walking with foot slip. The main motion difference for S1 and S2 lies in the fact that for S1, the subject's right foot slipped and then left the floor, while for S2, the slipping foot came to stop before it left the floor. The results in Fig. 5.11(a) show that the GRF profiles of both subjects follow the regular walking pattern. In contrast, for walking with foot slip, the friction forces F_t for both subjects are much smaller than those in the normal walking. This confirms that the friction force is indeed a key factor to determine the slip. The results in Fig. 5.11(b) also show the force profile differences between S1 and S2. When the
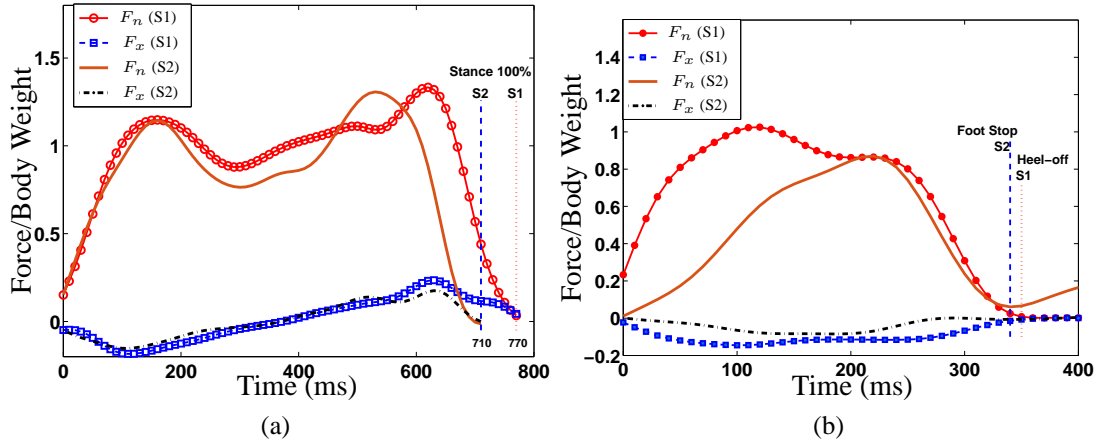
Figure 5.11: Comparison of the GRFs between normal and slip walking experiments. (a) Normal walking. (b) Walking with foot slip.

slipping foot does not stop before it leaves the ground (i.e., S1), both F_n and F_x come to zero at heel-off, while for the case where the slipping foot stops first, the friction force is near zero but with non-zero normal force (i.e., S2).

5.5.3 Discussions

Compared with the constructed $S_I(t)$ by the integration of the shank angular acceleration [120], the slip indicator in this dissertation demonstrates more robust and reliable results due to several improvements. The new slip indicator combines two highly-correlated variables ($\ddot{\theta}_{\text{HH}}$ and $\ddot{x}_s$) rather than one in [120]. The slip indicator in this dissertation uses instantaneous values of linear and angular accelerations rather than the integration and as a consequence, it results in significant differences between the normal walking and walking with slip. Moreover, we enhance the differences in $S_I(t)$ calculation by introducing the exponential function in (5.12).

The differences of the calculated $S_I(t)$ by using the IMU and motion capture measurements result from the different $\ddot{\theta}_{\text{HH}}$ and $\ddot{x}_s$ profiles. Figure 5.12 shows the comparison of the mean and standard deviation profiles of $\ddot{\theta}_{\text{HH}}$ and $\ddot{x}_s$ by these two sets
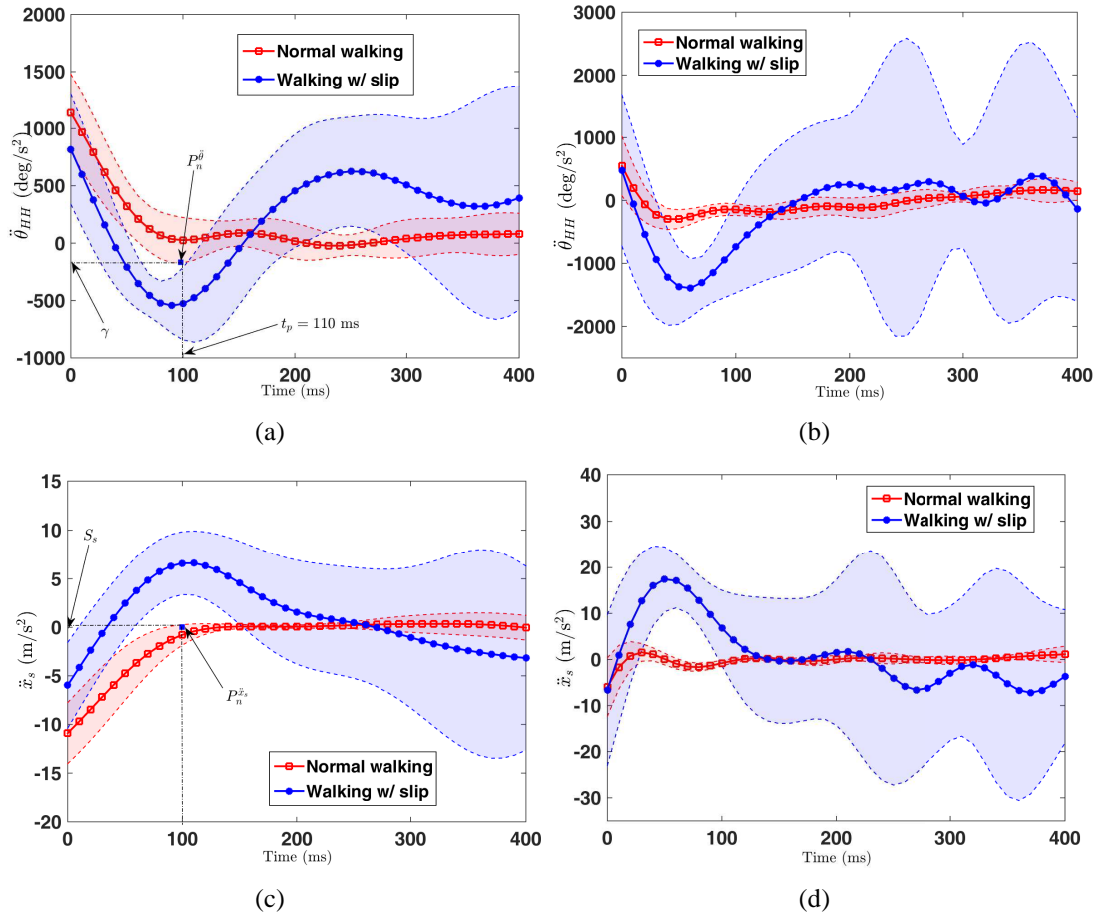
Figure 5.12: Comparison of the IMU-based and Vicon-based computations of angular accelerations $\ddot{\theta}_{HH}$ and heel acceleration $\ddot{x}_s$. (a) $\ddot{\theta}_{HH}$ profiles from the IMU measurements. (b) $\ddot{\theta}_{HH}$ profiles from the Vicon data. (c) $\ddot{x}_s$ profiles by the IMU measurements. (d) $\ddot{x}_s$ profiles by the Vicon data.

of measurements. The profiles of both the normal walking and walking with foot slip are also plotted in the figure for comparison. For the Vicon-based $\ddot{\theta}_{HH}$ profiles shown in Fig. 5.12(b), a significant distinction of the minimum values of $\ddot{\theta}_{HH}$ is observed between the normal walking and the walking with foot slip in the first 150 ms period after the heel strike. Similar difference has also been observed in the calculated values from the IMU measurements shown in Fig. 5.12(a). During normal walking, the hip-heel angular accelerations $\ddot{\theta}_{HH}$ experience a decreasing trend after the heel strike and then a slowly increasing and flat trend until the heel-off event. Consequently, due to an initial high COM pivoting angular velocity and a near-zero angular acceleration, an almost

constant angular velocity is maintained, resulting in a steady pivoting of the hip (and COM) with respect to the heel.

When slip is initiated after the heel-strike, $\ddot{\theta}_{\mathrm{HH}}$ starts at the similar values compared to those of the normal walking case but afterwards rapidly decreases and reaches a significantly lower values. The rapid decrease causes a negative hip-heel angular velocity and also reduction of the angle θ_{HH}. This clearly indicates that the hip (and COM) is not pivoting around the heel, but is indeed actually swinging backwards relatively to the foot. This observation implies the presence of a foot slip. After the initial rapid decrease, the values of $\ddot{\theta}_{\mathrm{HH}}$ quickly increase to near-zero values after around 150 ms mainly due to the push-off with the trailing leg. The profiles then oscillate around the zero value because of the human slip-recovery reactions.

The differences of the $\ddot{\theta}_{\mathrm{HH}}$ profile by the motion capture and the IMU measurements primarily result from the possibly different locations of the optical markers and the accelerometer and the numerical differentiation approximations. However, despite of the above-mentioned differences, a clear distinction of the $\ddot{\theta}_{\mathrm{HH}}$ profiles between the normal walking and walking with slips is observed shortly after the heel strike. The comparison also confirms the validity of the approach of real-time calculation of $\ddot{\theta}_{\mathrm{HH}}$ using the IMU measurements for the slip detection algorithm.

As shown in Figs. 5.12(c) and 5.12(d), the heel acceleration $\ddot{x}_s$ under the normal walking quickly increases to and stays around the zero value until the heel-off. For the walking with slip case, the $\ddot{x}_s$ profile first increases similarly as in normal walking but after the foot-floor contact, the heel does not stop but keeps accelerating (between 20-100 ms). Similar trend of the heel acceleration curves was also reported in [16, 69]. The $\ddot{x}_s$ profiles also show a large variation after around 150 ms and this could result from the start of the human recovery reactions.

The choices of the values of the model parameters β, γ and the threshold S_s are

determined by the $\ddot{\theta}_{HH}$ and $\ddot{x}_s$ profiles shown in Figs. 5.12(a) and 5.12(c), respectively. For simplicity, the value of parameter β is chosen as the Euler's number, that is, $\beta = e = 2.718$. To determine the value of parameter γ, we use the profile of $\ddot{\theta}_{HH}$ as shown in Fig. 5.12(a). The profiles of $\ddot{\theta}_{HH}$ under normal walking show a consistently small variation across all subjects and therefore, we use the first lowest peak point of $\ddot{\theta}_{HH}$ profile of normal walking, marked $P_n^{\ddot{\theta}}$ in the figure, to determine the value of γ. Using such a choice, we differentiate the values of slip indicator $S_I(t)$ between the normal walking and walking with foot slip. In the experiments, we obtain $\gamma = -562$ and $\gamma = -377$ deg/s for the motion capture system and the wearable IMU sensor measurements[2], respectively. Similarly, we use the slipping acceleration profile $\ddot{x}_s$ to determine the threshold value S_s. As shown in Fig. 5.12(c), the peak point $P_n^{\ddot{x}_s}$ of the $\ddot{x}_s$ profile is collocated with $P_n^{\ddot{\theta}}$. The corresponding value of $\ddot{x}_s$ is the same as S_s because at this point, $\ddot{\theta}_{HH} = \gamma$ and by (5.12), $S_s = \ddot{x}_s$. We obtain $S_s = 2.83$ for the motion capture data and $S_s = 1.57$ for the IMU measurements.

The slip detection algorithm also needs the detection of the heel-off event to terminate the algorithm and prevent false slip detection during the swing phase. We first estimate the shank angle θ_{Sh} by integrating the measurements of the gyroscope attached on the shank with a zero initial condition starting from the moment of the heel-strike event. Once the value of the estimated θ_{Sh} reaches threshold $\theta_{Sh}^{thr} = 22°$ (taken as the mean at the 50% stance of all subjects), the integration of the heel gyroscope measurement starts (with a zero initial condition) to obtain the θ_{He}. Figure 5.13 shows the estimates of the heel-off angle θ_{He} and the detection time for all subjects using the IMU measurements and the ground truth from the vertical motion of the heel marker positions. Similar to [108], a threshold $\theta_{He}^{thr} = 3°$ is used to detect the heel-off event. From the results in Fig. 5.13, the IMU-based heel-off events match closely with the ground

---

[2]These values of parameter γ are actually obtained from two standard deviations of $\ddot{\theta}_{HH}$ profiles. Similarly, the following S_s values are obtained from two standard deviations of $\ddot{x}_s$ profiles.

truth.
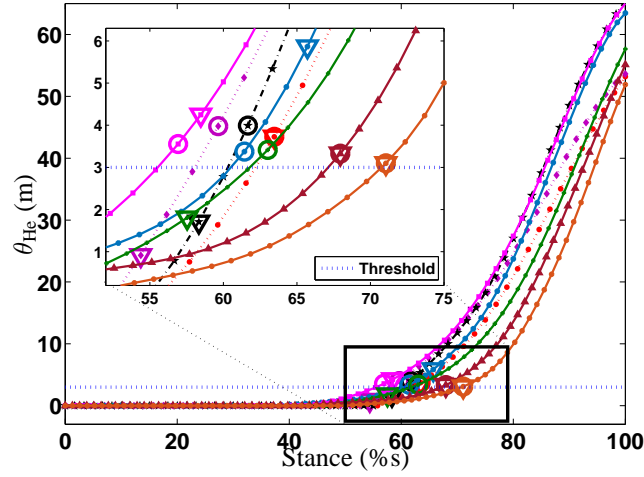
Figure 5.13: The estimation of the heel-off angle θ_{He} and heel-off event detection for all subjects. The "∘" and the "▽" markers indicate the heel-off instances detected by the IMU measurement and the Vicon motion capture system.

The use of kinematic constraints (5.9) and (5.10) is important for the convergence of the EKF design. The relationship in (5.9) is an approximation and Fig. 5.14(a) illustrates the values of y_2 that are calculated with the ground truth for both the normal walking and the walking with slip for all subjects. It is clear that the values of constraints (5.9) are around zero and have smaller variations for the normal walking than those under walking with slip. For walking with slip, a large variation exists and this variation is captured through the noise model in (5.9). Similarly, Figs. 5.14(b) and 5.14(c) show the values of estimated hip velocity v_x^{Hip} and output y_3 in constraint (5.10) for both the normal walking and walking with slip. The same conclusions are obtained for the hip velocity estimation and constraint (5.10) as those of constraint (5.9).

The slip detection and prediction results in this dissertation focus on the first slip, that is, the unexpected and novel to the subjects. Therefore, these results are limited to detect the unexpected slip in human walking. As reported and analyzed in [121, 122], the walking gaits on slippery surfaces are different if the human subjects are aware of the surface conditions and have prior slip experience. The slip detection and prediction
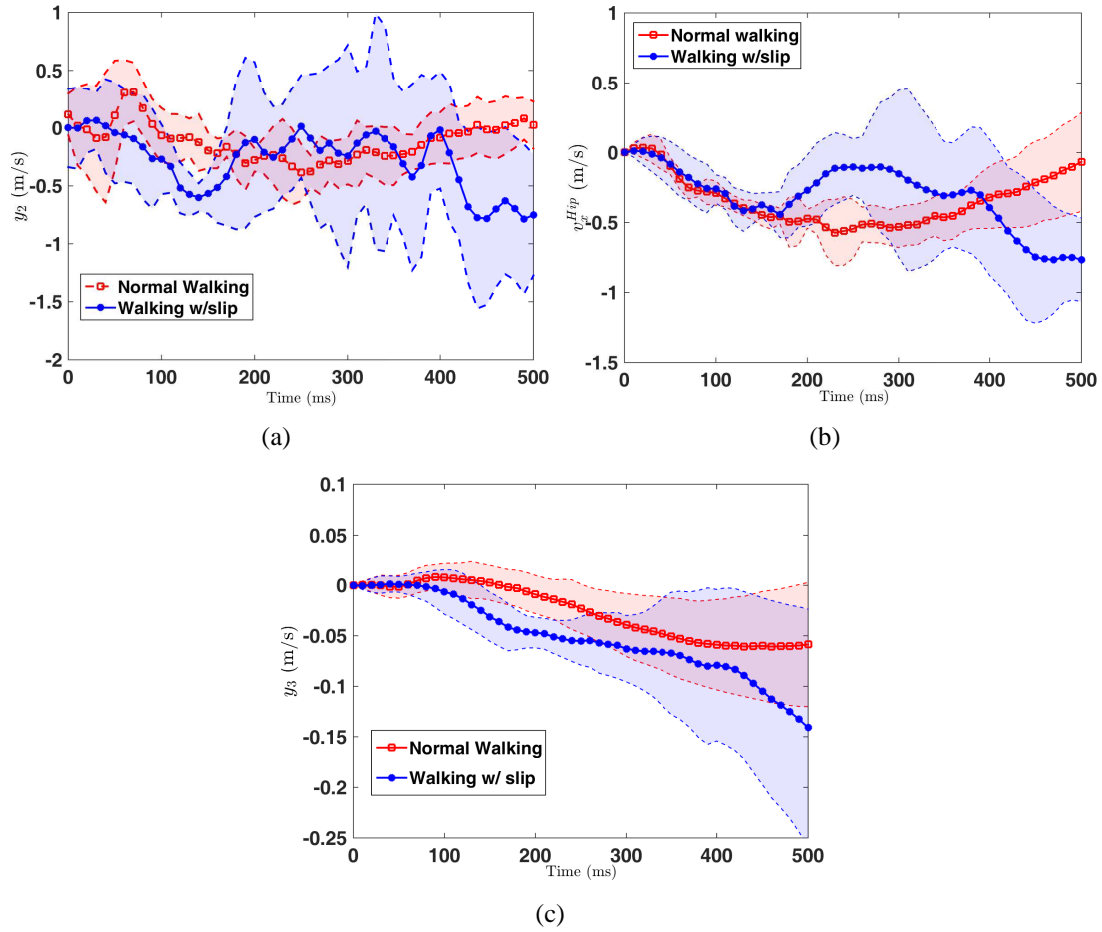
Figure 5.14: Comparison results of (a) the EKF output y_2, (b) the estimated hip velocity v_x^{hip}, and (c) the EKF output y_3 with the mean value and the one-standard deviation curves from all subject experiments.

for human walking with prior slip experience and knowledge are out of the scope of this study.

5.6 Conclusion

We presented a novel real-time foot slip detection and prediction method for human walking. The proposed slip detection and prediction method used only the measurements from a set of wearable inertial sensors attached to the lower-limbs and therefore, the approach is convenient, low-cost, non-intrusive for personal daily activities. The slip prediction algorithm was built on the slip dynamics model with the integration of

the physical and walking movement constraints through an EKF design. A slip indicator was also introduced to detect the initiation of the foot slip after heel strike. The slip indicator used the hip-heel angular acceleration and the heel slip acceleration information that were both obtained from the wearable inertial sensors. The extensive experimental results confirmed that the detection algorithm can effectively detect the foot slip events and also demonstrated the accurate slip predictions.

Chapter 6

Human Balance Control and Slip-Induced Fall Prevention

Human balance control is important to maintain equilibrium during walking and unexpected perturbations, such as foot slip. In the first part of this chapter we present a LIP-based dynamics model and control that can capture human balance recovery in normal walking and walking with foot slips. This is an extension of the modeling approach presented in Chapter 4 that cannot be used for walking balance control due to its complexity of full-body dynamics. In the second part of this chapter, we present a design of a robotic knee assistive device as a new paradigm to examine an active slip-induced fall prevention possibilities by providing to human an assistive knee torque during foot slip recovery. Balance recovery control of the first part of this chapter lies as a foundation for the control of the robotic knee assistive device that remains our future work and is out of the scope of this dissertation.

6.1   Introduction

Slip-and-fall is a complex human locomotion and it is challenging to model human reaction and control to foot slips due to fast slip dynamics and high-dimensional human movements. Further challenges arise as few real-time sensing and actuation technologies are currently available for reliably detect and predict the foot slips and assist human balance recovery after foot slips.

Robotic bipedal dynamic models, LIP and spring linear inverted pendulum (SLIP)

models are used to capture human walking and running [51,52,54,55]. However, all of these models assume non-slip conditions of the foot contact and cannot be directly used to design human balance control under foot slip. Furthermore, in [63], a simulation optimization-based model is used to obtain and compare the stability results of the dynamic balance analyses using a simple invented pendulum model. In the clinical studies of balance recovery, comparison of the joint torque and joint angle profiles are reported between the normal and slip walking [84, 85]. Moreover, the compensatory stepping for slip recovery is also discussed in [123], but no clear gait control strategies are presented.

In this chapter, we present the LIP-based balance recovery control of human walking with slips. A two-mass LIP model is first introduced to produce the human gaits in normal walking and walking with slips. This model extends the results in [60] by separately capturing the ZMP control and the walking pivoting point. The balance recovery control is then designed using the two-mass LIP model and the extended capture point design for foot slip. Because of non-periodic gaits, we discuss the recovery CP profiles that are built on the human experiments. The balance recovery control has hybrid features due to the different strategies taken in the single- and double-stance phases. We illustrate and demonstrate the control performance through human experiments. To the authors' best knowledge, this work is the first attempt to present the human-inspired balance recovery control under foot slips[3].

In the second part of this chapter, we present a design and fabrication of a wearable robotic knee assistive device for active slip-induced fall prevention. A prevention of human slip-induced falls is a challenging task, due to slip being a fast evolving and complex process requiring fast corrective reactions for successful slip recovery. In the literature, several different approaches are reported to address or suggest fall prevention

---

[3]The presented work in the first part of this chapter is a joint work that resulted in publication [124]. It is presented here for completeness of this dissertation.

actions. A proactive approach was reported in [125], where a repeated slip induced training during sit-to-stand task was shown to effectively reduce falls among older adults during sit-to-stand task. A similar approach, using a movable platform for slip training, was performed for personnel delivering mail in [81], where it was shown that such training improves recovery reactions and reduce fall frequency in older adults. A fall prevention program was suggested in [87] with strength training focusing on improving maximum strength and explosive strength measure. The subjects in the study mainly trained their cognitive reaction skills to train and improve their reactions to slip occurrence.

Studies of slip biomechanics have shown that compared to the normal gait the knee and ankle joints have the highest torque variations during a successful slip recovery [84, 85]. In [87], it was suggested that higher knee extension strength, such as greater knee peak torque and greater rate of torque development (RTD), are critical for slip balance recovery. These findings imply that for successful fall prevention it would be the most beneficial to provide assistive torques at the knee and ankle joints. From these studies we hypothesize that the additional assistive knee torque could contribute towards successful slip recovery and prevent slip-induced falls. The goal of the second part of this chapter is to design and fabricate a robotic device to enable investigate this hypothesis.

Exoskeletons, orthoses and walking assistive devices are commonly used existing devices providing additional torques at human joints [126–128]. A short overview of such existing human walking assistive devices reported in the literature is described below, with aim to explore their designs concepts and to inspire the design of the slip-induced fall prevention device.

All of the mentioned devices in [126–128] have been primarily designed towards providing long-time continuous support to the human body, such as carrying heavy weights or increasing walking endurance/range capabilities. The methods of joint

actuation used in those devices were comprised of passive actuation, such as elastic knee exoskeleton [129, 130] or active support, utilized through the electric motors using either gears [131] or Bowden cables [77, 79, 132, 133], hydraulic actuators [134], pneumatic artificial muscles (PMA) [135] and electro-rheological fluid based actuators [136–138]. There is further distinction among the exoskeletons that transfer load directly to the ground, as compared for instance to the HAL exoskeleton system [139, 140] that augments torques directly at human joints. These devices operate in direct contact with the human and over the last two decades, the improvements towards direct human-robot interactions in those devices have been achieved by the implementation of the series-elastic actuators (SEA) [141–144]. One of the first examples of exoskeleton using SEA was the RoboKnee reported in [145]. Further development of the actuation of those devices involved implementation of a clutch between the motor and the mechanism, allowing joint free movement during gait or actuation of the human joints when desired. An example of clutched parallel-elastic actuators have been introduced in [146–148].

Assistive devices for slip-induced fall prevention require specific performances, such as providing instantaneous high peak torques and high RTD for a short time. For example, the duration of a slip in [67] was less than 0.4 sec (defined from the time of a heel strike until foot stopped or was lifted of the ground). Other desired features for the device include lightweight and compact design and a clutch mechanics that implies low energy consumption of the device, when no actuation is needed. To minimize the weight on the knee, it is desirable to dislocate the heaviest parts of the device away from the knee. A similar approach was reported in [79] for the lightest series elastic remote knee actuator (SERKA) developed to investigate gait in stroke. Although probably sharing a similar main structure, the performance requirements for the fall prevention device are quite different from the aforementioned exoskeletons and robotic assistive devices and, indeed, are similar to the reported ankle and knee gait

perturbator devices [76–78].

Figure 6.1 shows an example of a knee perturbators [77, 78]. The purpose of the gait perturbator devices is not to provide continuous assistive torque for a long time, but to induce fast perturbations during human gait. Such devices have been used in a clinical study of characterizing the stretch reflex response of the human thigh muscles to an unexpected knee flexion at the transition from stance to swing during walking gait [149]. These knee and ankle perturbators have short actuation times and can exert high torques at large angular velocities. Those performance characteristics are also highly desirable for slip-and-fall prevention device.

(a)   (b)
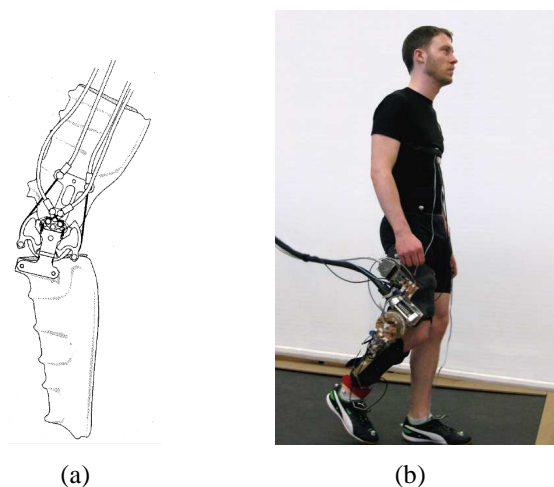
Figure 6.1: Knee perturbators reported in literature (a) [77] and (b) [78].

The second goal of this chapter is to present a preliminary design and fabrication of a new robotic knee assistive device for slip-induced fall prevention. The design requirements for this device are based on the comparison of the computed knee torques and angular velocities during normal walking and walking with slip obtained from our slip testing experiments. The designed robotic assistive system will be used to conduct further testing on human subjects.

The rest of this chapter is organized as follows. We e first present the two-mass LIP model in Section 6.2. The balance recovery control is discussed in Section 6.3. Design of the desired recovery profiles is presented in Section 6.4. We present the

experimental results of balance recovery control in Section 6.5. We then present the design of a robotic knee assistive device (ROKAD) in Section 6.6. We present the prototype of ROKAD and possible recovery control strategy for ROKAD in 6.7.

6.2 Two-mass linear inverted pendulum model

In this section, we present a new two-mass LIP model to capture the human walking with slips. Figure 6.2(a) shows the human walking with wearable inertial sensors on lower-limbs and Fig. 6.2(b) illustrates the schematic of the two-mass LIP model.

(a)   (b)
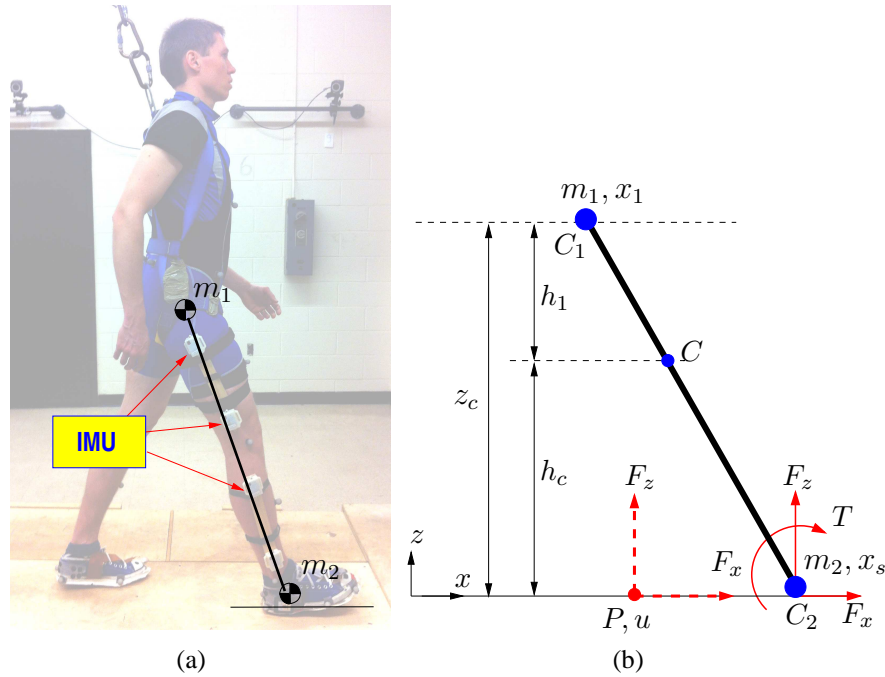
Figure 6.2: A schematic of the two-mass LIP model.

We model the human motion as a linear inverted pendulum with two points C_1 and C_2 with masses m_1 and m_2 at the two ends, respectively. Mass m_1 may represent the human body and m_2 for the lower-limb. Similar to most LIP literature, we assume that the height of mass m_1 is located at a constant vertical z_c and the other mass m_2 contacts with the ground. The introduction of the bottom mass m_2 into the model is primarily to capture the ankle actuation effect during foot slip by having mass moment of inertia

around the center of mass C. The horizontal positions of the two masses and the center of mass C in the ground-fixed frame xoz are denoted as x_1, x_s and x_c, respectively. It is straightforward to obtain

$$x_c = \frac{m_1 x_1 + m_2 x_s}{m_1 + m_2}.$$

We denote the normal and friction forces at the contact limb C_2 as F_z and F_x, respectively. Due to slipping at C_2, an ankle-like torque T is modeled at C_2. We also denote the ZMP location at P with x-axis coordinate u. At this point we can move the forces from C_2 without any additional moments if $T = F_z(x_s - u)$. Taking the forces at P without any additional moments, the rotational equation around C is obtained as

$$m_1 h_1(\ddot{x}_1 - \ddot{x}_c) - m_2 h_c(\ddot{x}_s - \ddot{x}_c) = -F_x h_2 + F_z(x_s - u), \qquad (6.1)$$

where $h_c = \frac{m_1 z_c}{m_1 + m_2}$ and $h_1 = \frac{m_2 z_c}{m_1 + m_2}$ are the vertical distance from C to C_2 and C_1 to C, respectively; see Fig. 6.2(b). Noting that $F_z = (m_1 + m_2)g$ due to no vertical acceleration of C, (6.1) is reduced to

$$\ddot{x}_1 - \ddot{x}_s = \frac{(m_1 + m_2)g}{m_2 z_c}(x_1 - u) + \frac{(m_1 + m_2)g}{m_1 z_c}(x_s - u) - \frac{F_x}{m_2}.$$

Along the horizontal direction, we obtain the governing equation of motion as

$$m_1 \ddot{x}_1 + m_2 \ddot{x}_s = F_x.$$

Combining the above two equations, we obtain the governing equation of motion for the two-mass LIP as

$$m_1 \ddot{x}_1 = \frac{m_1 g}{z_c}(x_1 - u) + \frac{m_2 g}{z_c}(x_s - u), \qquad (6.2a)$$

$$m_2 \ddot{x}_s = -\frac{m_1 g}{z_c}(x_1 - u) - \frac{m_2 g}{z_c}(x_s - u) + F_x. \qquad (6.2b)$$

For normal walking without foot slip, the friction force is enough to keep the stance foot stick to the ground. In this case, nonslip constraint $\dot{x}_s = \ddot{x}_s = 0$ is enforced. The

capture point (CP) describes the relative motion of COM with respect to the walking stance point [58], that is, point x_s. Therefore, denoting $\delta = x_1 - x_s$, the CP for the two-mass LIP model is given by

$$\xi = \delta + \frac{\dot{\delta}}{\omega}, \tag{6.3}$$

where constant ω is determined later in this section. The human body has the tendency to fall forward if $\xi > 0$ and backward if $\xi < 0$. For normal walking without slip, differentiating ξ and using $\dot{x}_s = \ddot{x}_s = 0$, we obtain

$$\dot{\xi} = \omega \left\{ \xi - \delta + \frac{1}{\omega^2} \left[\frac{g}{z_c} \delta + \frac{g}{z_c} \frac{m_1 + m_2}{m_1} (x_s - u) \right] \right\}. \tag{6.4}$$

By choosing $\omega = \omega_w = \sqrt{\frac{g}{z_c}}$ and combining δ dynamics with (6.4), we obtain the motion dynamics

$$\Sigma_{ns} : \begin{cases} \dot{\delta} = \omega_w(\xi - \delta), \\ \dot{\xi} = \omega_w \left[\xi - \frac{m_1 + m_2}{m_1}(u - x_s) \right]. \end{cases} \tag{6.5}$$

From (6.5), it is straightforward to show that δ converges to ξ while ξ dynamics is divergent.

For walking with foot slip, the friction force is assumed to be proportional to normal force, namely, $F_x = -\operatorname{sgn}(v_s)\mu(m_1 + m_2)g$, where μ is the friction coefficient and $v_s = \dot{x}_s$ is the foot slipping velocity. In this case, $\dot{x}_s \neq 0$, $\ddot{x}_s \neq 0$, similar to the above nonslip case and denoting $\omega_s = \sqrt{\frac{m_1 + m_2}{m_2} \frac{g}{z_c}}$, we obtain the human locomotion dynamics in state variables $\boldsymbol{x} = [\delta \ \xi]^T$ as

$$\Sigma_s : \begin{cases} \dot{\delta} = \omega_s(\xi - \delta), \\ \dot{\xi} = \omega_s \left[\xi - \frac{m_1 + m_2}{m_1}(u - x_s) + \mu z_c \right] \end{cases} \tag{6.6}$$

and the center of mass C satisfies

$$\dot{x}_c = v_c, \ \dot{v}_c = \frac{F_x}{m_1 + m_2} \tag{6.7}$$

where $v_c = \dot{x}_c$ is the center of mass velocity. Note that we choose $\omega_s = \sqrt{\frac{m_1+m_2}{m_2}\frac{g}{z_c}}$ such that δ does not appear in ξ dynamics in (6.6). We also assume that during the entire slipping period, v_s is positive and never changes directions.

Unlike the multi-link bipedal models [49], the above two-mass LIP model does not explicitly differentiate the single- and double-stance phases of human walking. The LIP model mainly captures the motion relationship among the COM, ZMP and CP and its simplicity is attractive for control systems design for human locomotion. In the two-mass LIP model, the human COM motion is captured by variable x_1 and the other variable x_s represents the ankle position of the (leading) stance leg (non-slip or slipping cases.) The switching of the single- and double-stance phases is captured through the changing value of ZMP position u, which can be discontinuous as shown in experiments. Similar to the multi-link bipedal models [49], variable x_s is relabelled once the next heel strike happens or slip stops.

6.3 Balance recovery control with foot slip

6.3.1 Hybrid dynamics with foot slips

As discussed in Chapter 4, human walking dynamics are captured by both the discrete events (e.g., heel strike and slipping) and continuous time systems. In Section 4.3, we showed the finite state diagram of the hybrid model for human walking with foot slip, see Fig. 4.2, and we described the finite states and transition between them.

The dynamic model Σ_{ns} in (6.5) represents the continuous-time dynamics in $\mathcal{S}_1$ and $\mathcal{S}_2$, while model Σ_s in (6.6) for $\mathcal{S}_3$ and $\mathcal{S}_4$. The transitions between $\mathcal{S}_1$ and $\mathcal{S}_2$ and $\mathcal{S}_3$ and $\mathcal{S}_4$ result in the possible discontinuous changes for ZMP position u in the model. Moreover, the human walker tries to control the ZMP position u to prevent the body from falling when foot slips happen. The triggering events between single- and double-stance phases are the heel-strike and toe-off and these events can be detected by

wearable sensors, such as shoe pressure sensors. The real-time detection and prediction of foot slips can also be accomplished using the wearable inertial sensors [120]. The end of the foot slipping event is considered to be determined by the external conditions (e.g., floor surface conditions), rather than by the balance recovery control.

Due to the complexity of the walking and slip dynamics, the balance recovery control strategies change for different phases. We consider the case when foot slip happens after the heel strike. During the single-stance slip phase, the COM position lags behind the ZMP and the control strategy is to recover the relative position between COM and ZMP through fast, small, compensatory step to reach double-stance phase. This is achieved by designing the swing time duration and the targeted CP. During the double-stance slip phase, if both legs slips, the control strategy is designed to regulate the COM position to a quasi-static equilibrium such that the gait can transit to the recovery steps once the slip stops. For non-slip recovery steps, the control strategy mainly deals with how to re-position the ZMP within the foot supporting polygon.

In the following sections, we describe the above-mentioned recovery control for each phase and apply these control strategies to a balance recovery in the sequence of $\mathcal{S}_1 \rightarrow \mathcal{S}_3 \rightarrow \mathcal{S}_4 \rightarrow \mathcal{S}_2 \rightarrow \mathcal{S}_1$. The description of this recovery example will be discussed in details in Section 6.5.

6.3.2 Balance recovery control

6.3.2.1 Single-stance slip control

In this phase, foot slips once it touches down on the floor and at that time, the trailing support leg is still in contact with the ground but is about to swing off the ground. We treat this stage as a single-stance phase. It takes a short time (around hundreds msec.) for human to detect slipping while still keeping normal walking gait. Due to slipping, the COM lags behind the ZMP and the body tends to fall backward.

The control goal in this phase is to adjust the relative COM and ZMP position by controlled CP. The CP controller computes the input at time t such that at the end of step time t_s, the CP reaches ξ_d. Assuming a constant input from t to t_s, the CP position is explicitly calculated by solving (6.6) as

$$\xi(t_s) = e^{\omega_s \Delta t} \xi(t) + (1 - e^{\omega_s \Delta t}) \Delta u, \tag{6.8}$$

where $\Delta t = t_s - t$ and $\Delta u = \frac{m_1 + m_2}{m_1}(u(t) - x_s(t)) - \mu z$. Letting $\xi(t_s) = \xi_d$ and solving for input u, from (6.8) we obtain

$$u = x_s + \frac{m_1}{m_1 + m_2} \left(\frac{\xi_d - b\xi(t)}{1 - b} + \mu z_c \right), \tag{6.9}$$

where $b = e^{\omega_s \Delta t}$.

Plugging (6.9) into (6.6), the closed-loop dynamics is obtained as

$$\dot{\boldsymbol{x}} = \begin{bmatrix} \dot{\delta} \\ \dot{\xi} \end{bmatrix} = \begin{bmatrix} -\omega_s & \omega_s \\ 0 & \frac{\omega_s}{1-b} \end{bmatrix} \boldsymbol{x} + \begin{bmatrix} 0 \\ -\frac{\omega_s}{1-b} \end{bmatrix} \xi_d. \tag{6.10}$$

The system has the eigenvalues $\lambda_1 = -\omega_s$, $\lambda_2 = \frac{\omega_s}{1-b}$. When $\Delta t > 0$, $1 - b < 0$ and therefore, both eigenvalues are negative and the system is stable. Moreover, if $F_x = -\mu(m_1 + m_2)g$, from (6.7), $\dot{v}_c = -\mu g < 0$, and then v_c is decelerating until slipping stops.

6.3.2.2 Double-stance slip control

Once the swing leg touches the floor, both feet are slipping. The human walker tries to adjust the ZMP position to support the body movement and keep balancing until the slip ends. Therefore, we consider a state feedback controller to regulate the gait to the equilibrium point.

Similar to the previous case, we write (6.6) as

$$\dot{\xi} = \omega_s(\xi - \Delta u)$$

We propose to use the state-feedback control

$$\Delta u = k_1 \xi + k_2, \tag{6.11}$$

where parameters k_1 and k_2 are obtained empirically from fitting the experimental data of double-stance recovery steps; see Fig. 6.3 for $k_1 = 1.9$ and $k_2 = 0.11$. The controller is stable if $k_1 > 1$. Ideally, this controller can drive $\boldsymbol{x}$ to the equilibrium at origin $\boldsymbol{x}_e = [0\ 0]^T$, that is, $x_1 = x_s$ and $\dot{x}_1 = \dot{x}_s$ such that the model maintains the slipping without falling. However, for a short time and short CP range, an aggressive ZMP control could also work to drive CP from a negative towards positive values and therefore to move COM ahead relative to the ZMP point.
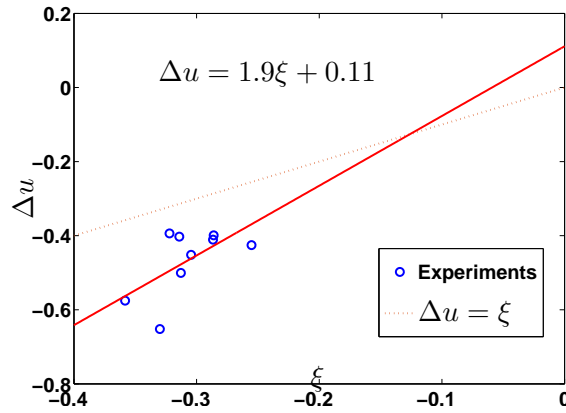
Figure 6.3: Relationship of the ZMP control and the CP during the double-stance slip recovery.

6.3.2.3 Double-stance nonslip control

When the foot stops slipping, the human upper body is still moving forward. Human walker recovers either by a complete stop or normal gait of walking, depending on the initial condition right after the nonslip phase begins.

In the double-stance nonslip phase, a linear quadratic regulator (LQR) is applied to

perform the recovery. The CP dynamics Σ_{ns} (6.6) is augmented to

$$\dot{\boldsymbol{\xi}}_r := \begin{bmatrix} \dot{\xi} \\ \dot{u}_r \end{bmatrix} = \underbrace{\begin{bmatrix} \omega_w & -\omega_w \frac{m_1+m_2}{m_1} \\ 0 & 0 \end{bmatrix}}_{\boldsymbol{A_r}} \boldsymbol{\xi}_r + \underbrace{\begin{bmatrix} 0 \\ 1 \end{bmatrix}}_{\boldsymbol{B_r}} a_r, \tag{6.12}$$

where $u_r = u - x_s$ and input $a_r = \dot{u}_r$ is the ZMP velocity. The objective function is

$$J = \int_0^\infty \left(\frac{1}{2}\boldsymbol{\xi}_r^T \boldsymbol{Q} \boldsymbol{\xi}_r + \frac{1}{2} a_r R a_r \right) dt,$$

where $\boldsymbol{Q} \in \mathbb{R}^{2\times 2}, R > 0$ are weighting constants. Since pair $(\boldsymbol{A}_r, \boldsymbol{B}_r)$ is controllable, the LQR control is given as $a_r = -\boldsymbol{K}\boldsymbol{\xi}_r$, where $\boldsymbol{K} = R^{-1}\boldsymbol{B}_r^T \boldsymbol{S}$ and $\boldsymbol{S}$ is the solution of the algebraic Riccati equation $\boldsymbol{A}_r^T \boldsymbol{S} + \boldsymbol{S}\boldsymbol{A}_r - \boldsymbol{S}\boldsymbol{B}_r R^{-1}\boldsymbol{B}_r^T \boldsymbol{S} + \boldsymbol{Q} = \boldsymbol{0}$. The ZMP position also needs to satisfy constraint $|u_r| \leq \beta$, where β is the supporting polygon length. When $|u_r| = \beta$, the ZMP stays at the edge of support polygon and immediately one foot should swing to initiate a compensatory step. The normal walking single-stance control should be initiated.

6.3.2.4 Single-stance nonslip control

In this last phase, the human gait is recovered to normal walking. We apply the CP-based normal walking control. The solution of Σ_{ns} in (6.5) is obtained as

$$\xi(t_s) = b\xi(t) + (1 - b)\frac{m_1 + m_2}{m_1}(u(t) - x_s(t)) \tag{6.13}$$

where $\Delta t = t_s - t$ and $b = e^{\omega_w \Delta t}$. Letting $\xi(t_s) = \xi_d$, the control input u is obtained as

$$u = x_s + \frac{m_1}{m_1 + m_2}\frac{\xi_d - b\xi(t)}{1 - b}. \tag{6.14}$$

Control input (6.14) is similar to the single-stance slipping control (6.9) and the closed-loop stability is obtained similarly.

6.4   Design of balance recovery profiles

In this section, we present the recovery profile design that are used in the balance recovery control discussed in the previous section. For the four cases of the recovery control, the planned single-stance duration $\Delta t = t_s - t$ and desired CP ξ_d at t_s are the primarily profiles that need to be carefully computed. For double-stance slipping control, the empirical profile is given from the experimental data as shown in Fig. 6.3.

During single-stance normal walking, the ZMP position is preferred to be close to pivoting point x_s for robust disturbance rejection. Assuming $u - x_s = 0$ during the entire phase, from (6.13) we have $\xi_d = \xi(t_s) = e^{\omega_w \Delta t} \xi(t)$. Typically we choose $\xi_d = d_{sl}$, where d_{sl} is the step length, then the single-stance duration is $\Delta t = \frac{1}{\omega_w} \ln \frac{d_{sl}}{\xi(t)}$.

During the single-stance slip phase, the subject has the tendency to fall backward. It is desirable to move ZMP backward as much as possible though its position is constrained by the length of the slipping foot support polygon (i.e., β). Meanwhile, the swing leg needs to touch down on the ground as soon as possible to initiate a recovery double-stance double phase. From (6.8), we note that the end of step CP position $\xi(t_s)$ is decreasing with an increase of $u - x_s$. To prevent the body from falling backward, the value of term $u - x_s$ should be as small as possible, i.e., $u - x_s = -\beta$. Then we have

$$\xi(t_s) = b\xi_s(t) + (1 - b)\left(-\frac{m_1 + m_2}{m_1}\beta - \mu z_c\right). \tag{6.15}$$

Therefore, if the single-stance slip duration Δt is determined by the shortest time the swing foot touches on the ground, the ξ_d is set at $\xi_d = \xi(t_s)$ by (6.15), where $t_s = t + \Delta t$. In the following, we present how to compute smallest Δt.

By observing the transition from $\mathcal{S}_4$ to $\mathcal{S}_3$, we further divide this transition into two sub-phases. The first sub-phase represents a small time duration Δt_1 when both feet are still in contact with the ground and the front leg is slipping after heel-strike. The second sub-phase, with duration Δt_2, starts from the swing leg leaving the ground until

it touches again after performing a compensatory recovery step.

To compute Δt_1, we use a pendulum model with rotating joint at the COM. As shown in Fig. 6.4, we denote the absolute angle $\theta_1(t)$ in the COM frame as the angle between the vertical line and the swing foot. The pendulum motion represents the "back-swing" of the trailing leg. At the beginning, angle $\theta_1(t)$ is negative and is further decreasing until $\dot{\theta}_1(t)$ reaches zero and at that moment, the first sub-phase ends, namely, the trailing foot lifts-off and starts to swing forward.
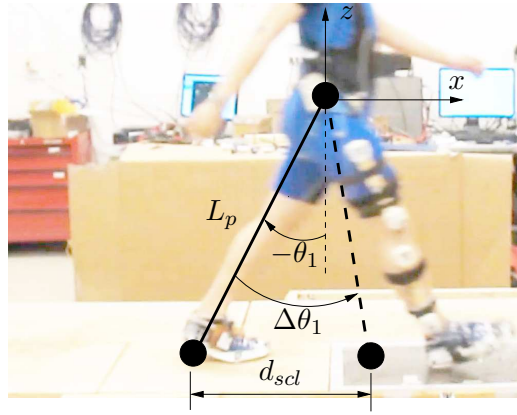
Figure 6.4: Schematic to compute the recovery time duration of the single-stance slipping phase.

The governing equation of motion for the pendulum is $\ddot{\theta}_1(t) + \omega_s^2 \theta_1(t) = 0$ and its solution is $\theta_1(t) = A \sin(\omega_s t) + B \cos(\omega_s t)$. Two initial conditions are used to obtain constants A and B: the initial angle $\theta_1(t)$ and the initial angular velocity $\dot{\theta}_1(t)$ at time t. The initial position $\theta_1(t)$ can be obtained by wearable gait sensor (e.g., inertial sensors) and we use the COM velocity $\dot{x}_1(t)$ to approximate $\dot{\theta}_1(t) = -\dot{x}_1(t)/L_p$, where L_p is the distance between the heel of the trailing leg and the COM. With known A and B, we obtain Δt_1 by setting $\dot{\theta}_1(t + \Delta t_1) = 0$ as

$$\Delta t_1 = \frac{1}{\omega_s} \tan^{-1} \left(\frac{\dot{x}_1(t)}{L_p \omega_s \theta_1(t)} \right).$$

The second sub-phase starts with the toe-off of the swinging leg and performing a compensatory step. This observation is true for normal and fast walking speed [123].

The response and reaction time vary among subjects, due to different capabilities of musculoskeletal system and slip sensory systems. The time duration Δt_2 of the second sub-phase is estimated using the length of the compensatory step length d_{csl} performed by the swing leg. We use the empirical results between the human walking speed and d_{csl} reported in [123], that is,

$$d_{csl} = h_h \left(0.9003 \frac{\dot{x}_1}{\sqrt{gh_h}} - 0.0622 \right),$$

where h_h is the human height and $\dot{x}_1$ is the COM horizontal velocity. We use the same pendulum model with a natural frequency $\omega_p = \sqrt{\frac{g}{L_p}}$ as shown in Fig. 6.4. The initial angle is obtained from the previous sub-phase as $\theta_1(t + \Delta t_1) =: \theta_1(t_1^f)$. Due to the heel pivoting effect around the toe, a non-zero initial angular velocity $\dot{\theta}_1(t + \Delta t_1) = \dot{x}_h/L_p$, where the heel velocity $\dot{x}_h$ is obtained from the previous step during the toe-off phase. The final pendulum position at the swinging leg touch-down is then obtained as $\theta_1(t + \Delta t_2) = \theta_1(t_1^f) + \Delta\theta_1$, where $\Delta\theta_1 = d_{csl}/L_p$ for small angle $\Delta\theta_1$. Solving the equation

$$\theta_1(t_1^f) + \frac{d_{csl}}{L_p} = \frac{\dot{x}_h}{L_p\omega_p} \sin(\omega_p t) + \theta_1(t_1^f) \cos(\omega_p t)$$

for time $t_s = t_1^f + \Delta t_2$, we obtain

$$\Delta t_2 = \frac{1}{\omega_p} \left(\sin^{-1} \frac{L_p\theta_1(t_1^f) + d_{csl}}{L_pC} - \tan^{-1} \frac{\dot{x}_1\omega_p}{L_p\theta_1(t_1^f)} \right),$$

where $C = \sqrt{\frac{\dot{x}_1^2}{L_p^2\omega_p^2} + \theta_1^2(t_1^f)}$. With the estimated Δt_1 and Δt_2, we compute $\Delta t = \Delta t_1 + \Delta t_2$.

6.5   Experimental results

In this section, we use experimental data to validate the proposed model and demonstrate the control design. The experiments are conducted in indoor setup and several subjects are recruited to conduct slip-and-fall walking. The subjects' gaits are captured
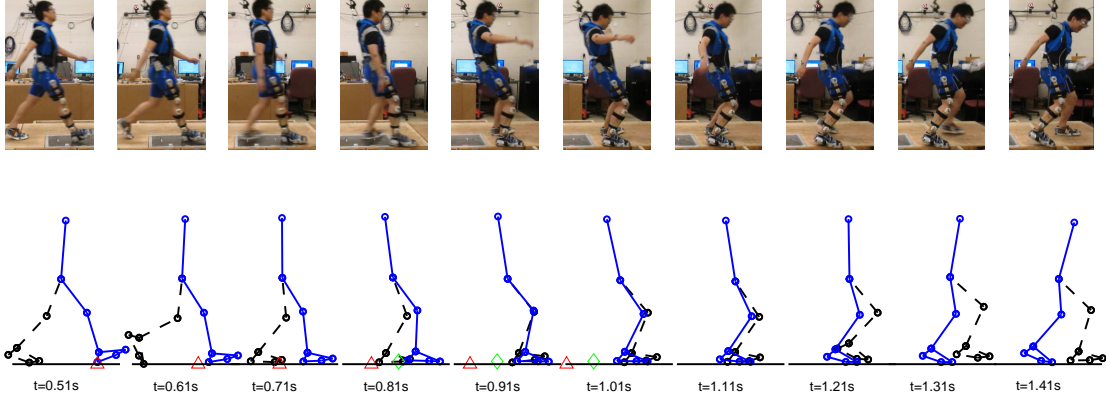
Figure 6.5: The snapshot sequences that show a successful balance recovery control of walking with foot slips.

by the motion capture system (from Vicon Inc.) and wearable force/torque sensors are embedded in the shoes. Wearable inertial sensors are also attached to the subjects' limbs to detect the foot slips. More details of the experimental setup are presented in [32, 120]. The subjects are asked to walk on a wooden platform and soap fluids are used to create slippery surface condition on some portions of the platform. Subjects are not informed about the location of these low friction portions. The friction coefficient of the slippery ground is measured as $\mu = 0.05$.

We present a balance recovery control experiment with snapshots shown in Fig. 6.5. As mentioned in Section 6.3, the entire balance recovery control is described as the sequence of $\mathcal{S}_1 \rightarrow \mathcal{S}_3 \rightarrow \mathcal{S}_4 \rightarrow \mathcal{S}_2 \rightarrow \mathcal{S}_1$ as follows. The subject conducts normal single-stance walking (i.e., $\mathcal{S}_1$) before foot slips starts. At $t = 0.51$ s, the slip happens when the right leg touches down on the floor. We refer this phase as the single-stance slip, i.e., $\mathcal{S}_3$. Meanwhile, the trailing leg is almost about to leave the ground and then swings in the air. The subject detects the right foot slip and tries to move the swing leg to touch on the ground as soon as possible and to place the ZMP backward to counteract the gravity torque. At $t = 0.77$ s, the swing leg touches on the ground and two feet support the body. From $t = 0.77$ to 0.97 s, both feet are slipping on the ground and this period is the double-stance slipping phase, i.e., $\mathcal{S}_4$. During this period, the ZMP
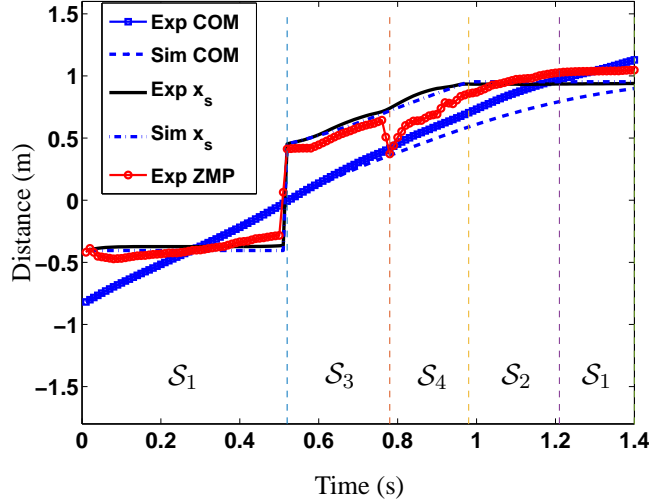
Figure 6.6: Simulation and validation of the two-mass LIP model with the experimental data.

location is manipulated to prevent body from falling. At $t = 0.97$ s, both slipping feet hit on the high-friction surface and slipping stops. From $t = 0.97$ to 1.21 s, both feet stand on the ground without slip. We refer this period as a double-stance nonslip phase, that is, $\mathcal{S}_2$. At $t = 1.21$ s, the left foot begins to leave the ground and takes one compensatory step. At $t = 1.39$ s, the foot contacts the ground before the swing leg contacts and this is a single-stance normal walking phase, i.e., $\mathcal{S}_1$.

We first demonstrate the validation of the proposed two-mass LIP model. Figure 6.6 shows the model prediction results with the experimental results comparison. The model prediction results are obtained by using the calculated ZMP profile in the experiments as inputs to Σ_{ns} and Σ_s. For comparison purpose, we use the same human subject experiments shown in Fig. 6.5. In the plot, five vertical lines at $t = 0.51$, 0.77, 0.97, 1.21, and 1.39 s separate the balance recovery duration into different phases as described previously. The prediction results of both the COM (x_1) and the slipping foot position (x_s) match the experimental results closely throughout all five phases. These results confirm that the two-mass LIP model captures the human balance recovery motion.

We next show the proposed recovery control design. Figure 6.7 demonstrates the
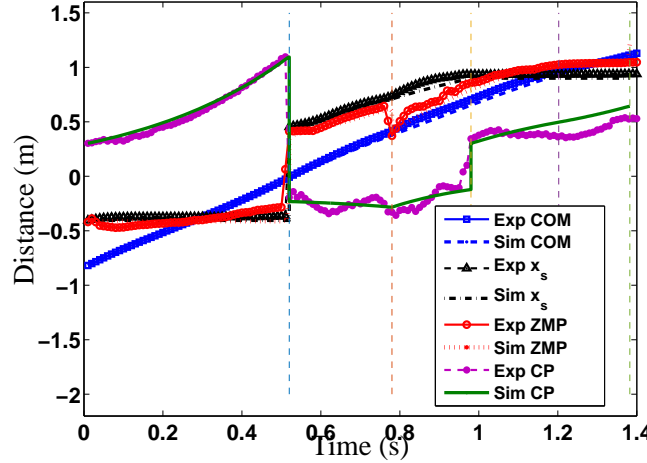
Figure 6.7: Simulation results of the control design and comparison with the experimental data.

performance of the hybrid control design for the same recovery experiment shown in Fig. 6.5. The simulation results in the figure are under the proposed hybrid control design. During the first phase ($\mathcal{S}_1$), the two-mass LIP model with $\dot{x}_s = 0$ constraint is simulated with the single-stance nonslip control. At $t = 0.51$ s, the single-stance slip control is initiated with the initial conditions of x_s and $\dot{x}_s$ matching the experiment data (in $\mathcal{S}_3$). The recovery profile, that is, t_s (= $0.51 + \Delta t$) and ξ_d, are calculated by the design presented in Section 6.4. For example, the experimental and predicted time durations of the first sub-phase are $\Delta t_1 = 0.1$ and 0.101 s, respectively, and for the second sub-phase these values are $\Delta t_2 = 0.16$ and 0.152 s, respectively. The prediction of the total time duration of the single-stance slip phase is $\Delta t = 0.253$ s and the actual duration in experiments is 0.26 s. These results confirm the correctness of the desired profile design.

During $\mathcal{S}_3$, the CP value decreases and the subject has great tendency to fall backward. From $t = 0.77$ s, the double-stance double slip control is applied to control the phase $\mathcal{S}_4$. The double-stance slip lasts for 0.2 s and then both feet stop slipping. After this incidence, the CP value jumps and becomes positive because the feet stick to ground and the COM velocity is moving forward. The human now has tendency to
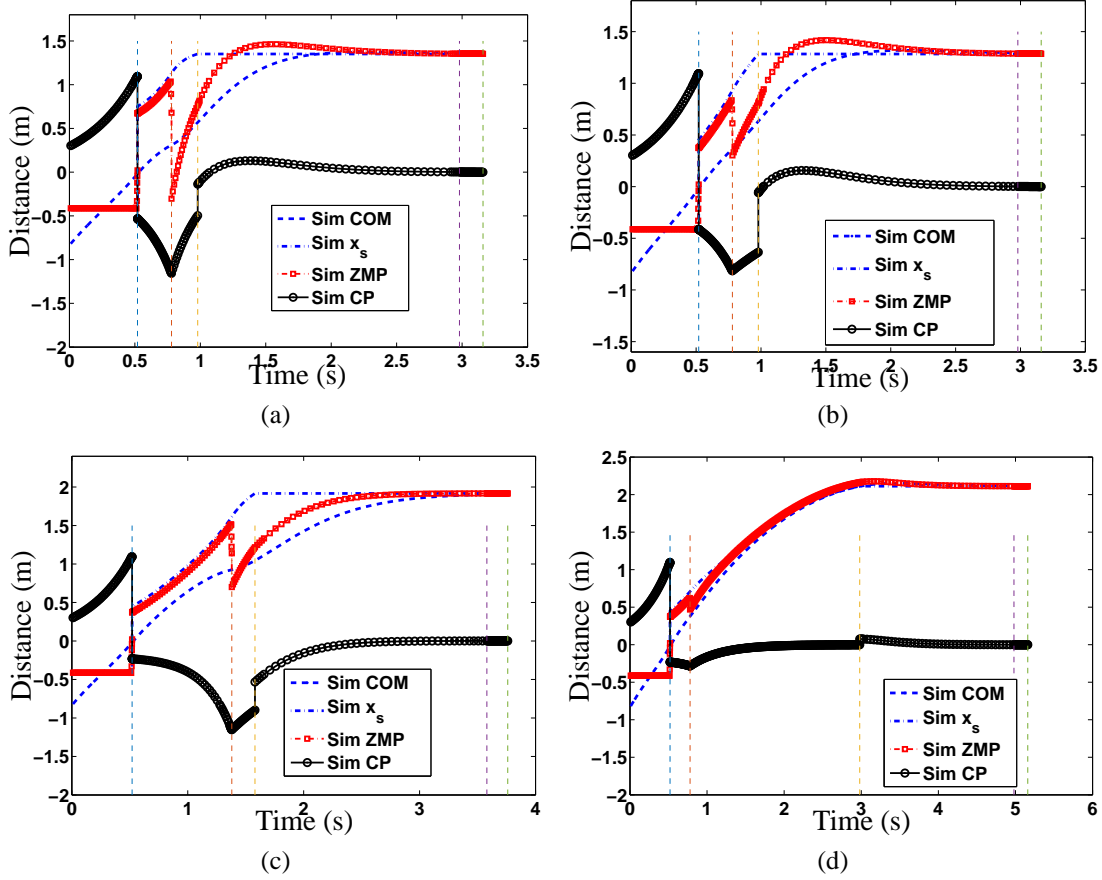
Figure 6.8: The balance recovery performance under various perturbed conditions. (a) Reduced heel-strike contact angle. (b) Increased initial slipping velocity. (c) Longer single-stance slipping duration. (d) Longer double-stance slipping duration.

fall forward. During this recovery step $\mathcal{S}_2$, the LQR is used to stabilize the motion. If the ZMP position reaches the edge of the support polygon, the control strategy immediately switches to the single-stance normal walking phase and recovers to normal walking. The controlled recovery gaits shown in Fig. 6.7 clearly confirm the consistent performance with the experiments.

We further apply the proposed balance recovery control to the above example with several variations. We perturb the initial state values and the timings of critical discrete events to explore how the recovery results change with respect to these perturbations. The perturbed variables include the initial heel-strike angle, initial slipping velocity, and the durations of the single-stance slip phase and the double-stance slip phase. We

only change one parameter at a time and keep all other variables the same as in the experiments. The simulation results of the controlled gaits under these perturbations are shown in Fig. 6.8.

To capture the heel-strike angle, we change the initial value of $x_s - x_c$, i.e., the distance between the foot and the LIP mass center. Figure 6.8(a) shows the simulation results with increased $x_s - x_c$, that is, decreased heel-strike touchdown angle. Compared to the experimental data in Fig. 6.7, the CP is further negative and decreases rapidly, which implies greater tendency to fall backward. Consequently, at the beginning of double-stance nonslip phase, the capture point is still negative. The simulated motion does not have the tendency to fall forward. The human walker comes to stop within the double-stance nonslip phase.

Simulation results shown in Fig. 6.8(b) uses the doubled value of the initial slipping velocity $\dot{x}_s$ as that in the experiment. The resulting recovery behavior is similar to that of increasing initial value of $x_s - x_c$ discussed above. It is understandable that the effect of the increasing initial slipping velocity on balance recovery would be similar to that of an decreased heel-strike angle.

A longer single-stance slipping duration happens when the subject has a larger delay time to detect the slip or react to the slipping event. Figure 6.8(c) shows the simulation results with a 0.6 s longer duration of the single-stance slip phase than that in experiments. As shown in the figure, both slipping distance x_s and the COM diverge during the single-stance slipping phase and indeed, the human falls quickly before the foot slip stops. In this case, the recovery control fails to keep the human balance. Therefore, it is critical for human sensorimotor mechanism to react quickly to the slip event to prevent falling consequence.

We now consider a longer duration in the double-stance slip phase. Having a long double-stance slip duration might not generate falling risk for human walkers who can handle the situation when both feet slip simultaneously. An extreme example is the

skilled ice skating players who can balance well while both feet slip for long time or long distance. Figure 6.8(d) shows the simulation results under a long duration of the double-stance slip phase. Clearly, the results show that the human achieves a stable configuration that keeps x_s close to the COM, that is, ξ_s close to zero. This implies no tendency to fall down and the human walker finally recovers to stop due to the increased friction force.

All of the above simulation results under perturbed conditions have demonstrated that the two-mass LIP model and the balance recovery control are capable to capture the key features and characteristics in slip-and-fall dynamics.

6.6   Design of a robotic knee assistive device (ROKAD)

The design of the robotic assistive device is built upon the results of a preceding analysis of the maximum human knee torques, angular velocities and power requirements during successful slip recovery. Figure. 6.9(a) shows the comparison of the knee joint moments in the sagittal plane of a representative subject in the experiments during normal walking and walking with recovered slip. The experimental data are taken from our initial study [120] and the subject was a young healthy male. The torques were computed in the OpenSim software [150] through the inverse dynamics using the motion capture kinematic data and the GRF measurements from the wearable force plates. The kinematic data was filtered using a second order low-pass filter with a cutoff frequency of 6 Hz [151].

The difference between the magnitude of the peak torques during normal walking and walking with foot slip shown in Fig. 6.9(a) is taken as the reference to determine the torque requirement of the knee assistive device. From the figure, the maximum difference of body weight normalized knee torques is $0.9 \ Nm/kg$. Considering the maximum weight of the subject as $100 \ kg$, the maximum assistive torque would be
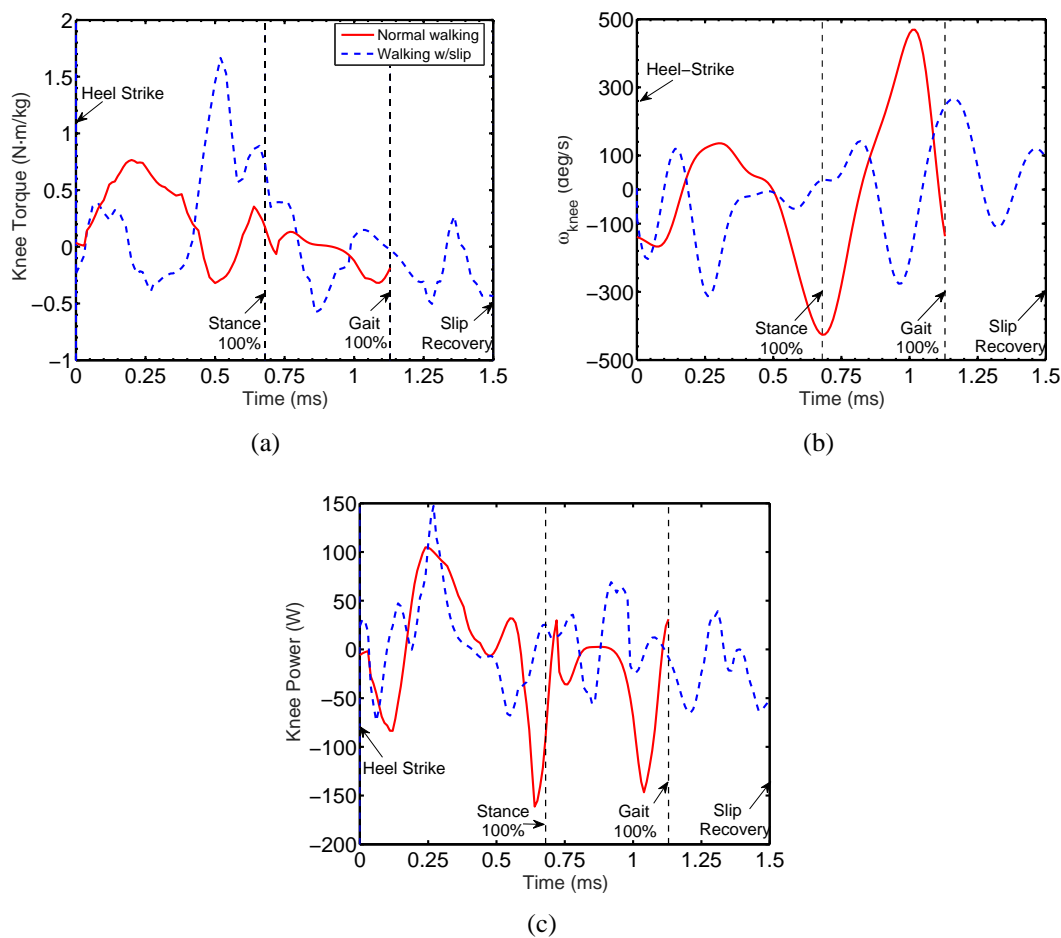
Figure 6.9: Right leg knee (a) torque, (b) angular velocity, and (c) power during normal walking (one step before slip) and during foot slip starting at the heel strike.

approximately $90\ Nm$.

Figure 6.9(b) shows the knee angular velocity profiles during the normal walking and walking with foot slip. The maximum absolute value of the maximum or minimum angular velocity peaks during slip was $313\ deg/s$. Figure 6.9(c) shows the computed knee power during the normal walking and the walking with foot slip. From the estimated torque and joint angle velocity we obtain the estimated maximum power during slip recovery control around $150\ W$.

Based on the above analysis of the desired maximum angular velocity and maximum torque specifications, we select the appropriate motor and gears (i.e., gear ratio),

and design other components of the assistive device. Similar specifications were reported for the knee perturbator in [78] with the characteristics of angular perturbation speed $360 \ deg/s$, maximum torque $80 \ Nm$ and holding torque of a clutch $115 \ Nm$. Other desired requirements of the device include lightweight (mass $< 3 \ kg$), low power consumption, unconstrained full range of motion of the knee joint ($0 - 120 \ deg$), compliance at human-device interface (similar to SEA), minimally intrusive during regular walking and to allow normal unconstrained motion of individuals wearing the device. To incorporate these features, we integrate a torsional spring and a clutch-type mechanism into the design of the robotic knee assistive device.

6.7   ROKAD prototype

Figure 6.10 shows the prototype of the robotic assistive device. The actuators, battery and the embedded systems are dislocated from the knee to minimize the weight on the knee joint to allow natural walking pattern, see Fig. 6.10. Figure 6.11 shows the cross-section of the wearable part of the device with marked notations of the individual parts.

The device is driven by an electric motor (Magmotor Inc., $150 \ W$ brushed servo motor, model $S23-150$, with a $500 \ cpr$ encoder). The motor control board (Sabertooth Inc., model 2×60) is powered by a $30 \ V$ battery and used to control the main motor. The main load is transferred from the motor through a bi-directional flexible shaft (C) (S.S. White Inc, model Ready-Flex $187L$, 30" long), which is connected to the extension shaft (D) supported by the bearings. Spiral miter gears (E) are used to transfer the axis of rotation for 90 degree along the main axis of the device, where the other pair of the miter gear is rigidly connected to the input side of the harmonic drive (F) (Cone Drive Operations Inc., model CBC20) with $80 : 1$ gear ratio. This is the maximum suggested gear ratio to be used for biomimetic joint actuation [152]. The fixed part of
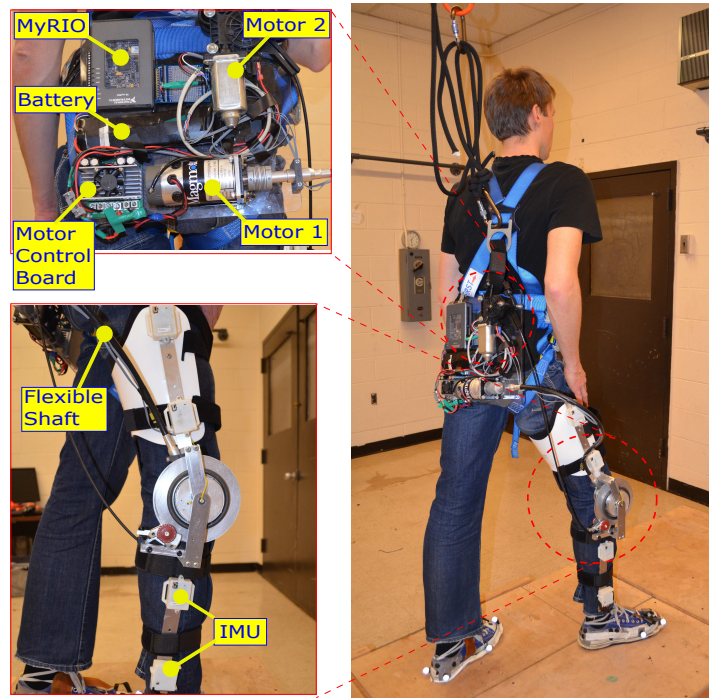
Figure 6.10: The robotic knee assistive device prototype.

the harmonic gear is mounted to the upper link (A) by using standoffs (P). The upper link of the device is attached to the thigh using a thigh brace (Alimed Inc.). The output side of the harmonic drive is rigidly mounted to the main shaft (H), supporting plate (I), thin cylinder (J) and one end of the torsional spring (K). A needle roller bearing (N) (INA Inc., model K70×76×20A) is used to allow smooth rotation of the cylinder around the fixed part of the gear. Such configuration also reduces load on the main shaft and constrains tilting motions and allows only the pure rotation of the harmonic gear output. The other end of the torsional spring is attached to the brake disc (L) that is fixed to a flange (M) and can rotate around the cylinder (J) through another roller bearing (N) (INA Inc., model K80×86×20A). Disc brake calipers (O) are mounted on the lower link (B) that is attached to the shank using the straps. Based on the desired maximum torque and using the recommendations from [153, 154], we have chosen a torsional spring with the approximate stiffness of $150\ Nm/rad$. The actual stiffness of the coil torsional spring (Peterson Spring Inc., OD=$104.41\ mm$, wire diam.=$8.41\ mm$)

is 166 Nm/rad.
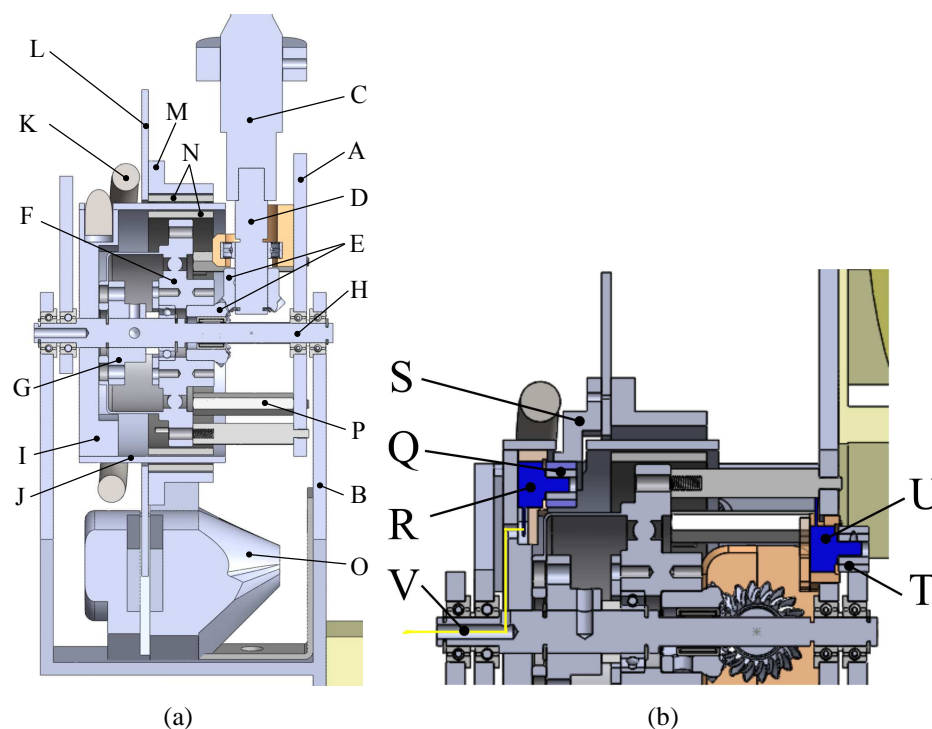
Figure 6.11: CAD model render of the device: (a) a lateral cross-section along the axis of the flexible shaft attachment, (b) cross-section showing the placement of the two rotary potentiometers.

To measure the knee angle we use a rotary potentiometer sensor (U) between the thigh (A) and the shank (B) link, see Fig 6.11(b) and Fig. 6.12. Two stoppers on the side of the thigh link are used to limit the motion of the brace within a regular knee range motion $0 - 120$ degrees. An additional rotary potentiometer (R) is used to measure the torsional spring deformation by measuring the displacements between the cylinder (J) and the disc brake (L). Contact between the friction wheel (Q) on the potentiometer and slider (S) attached to the disc brake rotates the potentiometer. Due to a large diameter ratio ($\sim 7 : 1$) of both elements in contact, the small spring deformation results in a large rotation of the potentiometer.

The clutch-type mechanism consists of a bicycles disk brakes providing high braking/friction force ($\sim 775\ N$) [155] and is therefore capable of holding a large torque. Brakes (Sram Inc., model Avid BB7) allow precise adjustments of each side of the pad
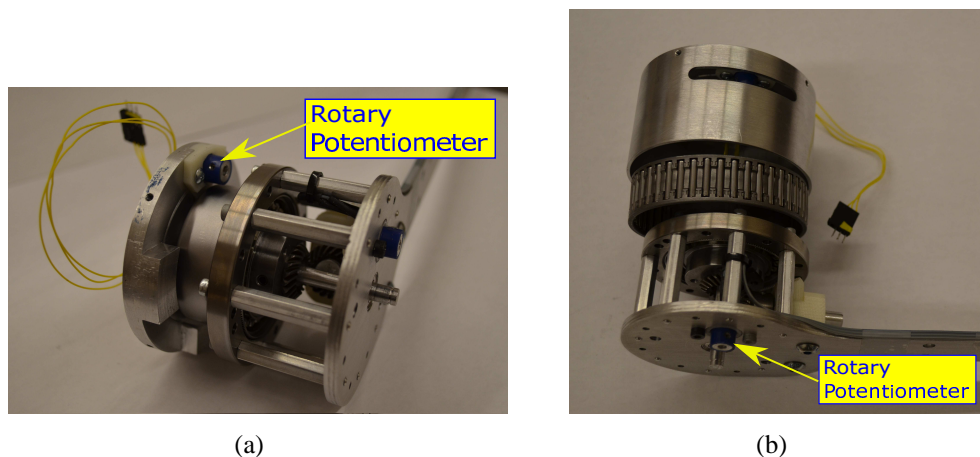
Figure 6.12: Gear assembly of the device with (a) rotary potentiometer to measure spring deflection and (b) rotary potentiometer to measure the knee angle.

on the calipers against the disk rotor and also minimizes clutch activation time. Such simple design guarantees the functionality and satisfies design requirements, although the design has not been optimized to minimize the weight.

For the purpose of onboard measurements and control, we use a real-time embedded system (MyRIO from National Instruments Inc.) to sample and process all the sensors and the wearable motion sensors measurements at $1kHz$. The characteristics and specifications of the knee assistive device are listed in Table 6.1.

Table 6.1: Specifications of the assistive device prototype

Max Torque	$90\ Nm$
Max Ang. Vel.	$360\ deg/s$
Gear ratio	$80:1$
Spring stiffness	$166\ Nm/rad$
Motor power	$150\ W$
Mass (knee part)	$2.5\ kg$
Mass (backpack)	$4.2\ kg$

Following the observations from the previous sections, we propose the slip recovery control strategy of the robotic knee assistive device to follow the human recovery reactions during slip that are obtained in experiments. Similar approach was proposed

in a recent paper [156] for the design of the lower limb prosthetics controller. Measuring of the muscle activity using electromyography (EMG) during walking with foot slips and walking on a slippery surfaces was reported in [86, 156]. Indeed, muscle response during slip was reported to be similar for young and older adults [86], starting with the activation of the Medial Hamstring at $\sim 175\ ms$, and followed by the onset of the Vastus Lateralis at $\sim 240\ ms$ after the heel contact. These findings match well with the onset of slip recovery reactions reported in [119]. In [84] the reaction time is defined as the occurrence of corrective moments at the knee and hip joint as an attempt to recover from slip. The onset of such corrective reactions was reported to start between 25% and 45% into stance, corresponding to approximately 190 ms and 350 ms after heel contact, respectively.

It was suggested in [84, 86] that the human reaction strategies to foot slip consist of the primary and secondary responses. In the primary response, the human tries to first bring the slipping foot closer back under to the COM. This is performed by initiating the knee flexion and hip extension moments at approximately 200 ms after the heel contact. Immediately after follows the secondary response when the human tries to stabilize itself by generating knee extension and hip flexion moments on a slipping leg as a support during slip [84]. Similar observations and conclusion were also reported in a study to investigate the earliest deviations of gait parameters during slip [157]. These reported timings of the corrective reactions match well with our experiments of the knee moment profiles shown in Fig. 6.9(a).

Typical series elastic actuators use the measured spring deflection to compute the actuator torques in the controller design [141, 158, 159]. Contrary to this approach, a PID-based torque control was implemented using the difference between a desired and the actual knee angle in [79]. We will choose the impedance control between the subject and the knee assistive device, which is suggested to be used for compliant actuators in exoskeletons [132, 160].

6.8   Conclusion

We presented a new dynamic model and control strategy for balance recovery in slip-and-fall human walking. The simple linear inverted pendulum cannot capture the key features such as non-periodic gait motion when foot slips and therefore, we presented a new two-mass LIP model for slip-and-fall human locomotion. Based on the new model, a hybrid control design was presented to drive the capture point along certain profiles for balance recovery during various slipping phases. Some key parameters such as slipping phase duration and the targeted CP were obtained by using the biomechanics models. Experiments and simulation results were presented to illustrate and demonstrate the model and the controller design. We also presented the performance of the balance recovery control under various perturbed conditions and compared these performance with the experiments.

In the second part of the chapter, we presented the preliminary design of a novel robotic knee assistive device (ROKAD) for slip-induced fall prevention. The advantages of ROKAD lie in its unique capabilities of generating a high torque ($\sim 90Nm$) and high angular velocity ($\sim 360deg/s$). The embedded torsional spring allowed desired compliance for human-device interactions [141, 158, 161]. The use of a clutch mechanism allows the device to be actuated only after the slip is detected and allows free motion during normal walking. All these features aim at minimally invasive to human natural gait during regular walking.

Chapter 7

Conclusions and Future Work

7.1 Conclusions

In this dissertation we presented a modelling, sensing and control framework for human slip-and-fall application. We thoroughly investigated and analysed three main aspects of human slip-and-fall: (i) slip generation and evolution, (ii) slip detection and prediction, and (iii) slip recovery control strategy using bipedal dynamics model. We also developed a robotic assistive device for slip-induced fall prevention.

Prediction of human foot slip during walking was achieved by analysing the shoe-ground interactions. The shoe-ground interactions provide the traction and braking forces and torques to support human walking. By understanding the friction force distribution and local slips detections within the shoe-floor contact area [32], we can predict the slip evolution in human walking. We proposed the model for the normal load distribution and the quasistatic model for the friction force and deformation distribution during normal walking and slip gaits. Detection of slip occurrence was in good agreement with the traditional slip prediction method using the RCOF. The advantage of using deformation measurements over using RCOF for slip prediction is that no information about the actual coefficient of friction is required. Along the same general framework of investigation of the shoe-ground interaction for slip prediction, we proposed a novel dynamic friction force model with applications to a general soft-solid contact application. We integrated the LuGre friction model with the beam-spring

network model to compute the friction force and deformation distributions on the soft-solid contact interface. The advantages of this dynamic model lie in its ability to capture the friction dynamics of the soft-solid contact and to simplify the calculation of the friction force and deformation distributions on the contact patch. The modelling scheme was validated using the fingertip-like contact application. The model prediction results of the friction forces and deformation distributions matched the experimental results.

For slip detection and monitoring during normal human walking, we proposed a novel real-time foot slip detection method. The method is based on the dynamics of the slipping leg, measured by the IMUs attached on the slipping leg, and integrated sensor measurements fusion through an EKF design. The method used inexpensive, lightweight and non-intrusive sensors for human mobility. The results showed that the method successfully predicted slipping distance with an accuracy of a few centimeters. Furthermore, we proposed a novel slip indication variable to determine whether the foot slip occurred. The slip indicator was based on a physical behavior of the COM movement about the heel and the acceleration of the stance leg heel itself during normal walking and walking with foot slip. Successful detection of unexpected slip events was validated through extensive multi-subject experiments.

For the slip recovery control during human walking locomotion, we first built an analytical 7-link planar bipedal dynamic model with a relaxed non-slip foot assumption used in the existing bipedal models. We developed hybrid bipedal slip dynamics model and the hybrid zero dynamic controller to match the the human gait profiles. The simulation results of the joint angles and the ground reaction forces (GRF) matched the experimental data. These analytical tools will be used as a foundation to propose a controller for successful slip recovery controller in our future work.

Control and prevention of slip-induced falls would be a natural extension of the work presented in previous chapters. To study a human balance control, we proposed

a new two-mass LIP model and control strategy to capture balance recovery during normal and slip-and-fall human walking. CP-based hybrid control was used to design and drive the recovery CP profiles along those from the experiments. Experimental and simulation results were presented to validate the model and controller design. Lastly, to examine slip-induced fall prevention possibilities, we designed and fabricated a prototype of robotic knee assistive device. We hypothesized that the assistive knee torque could contribute to successful slip recovery and prevent fall. Our robotic knee device was designed to meet the maximum torque ($90 \; Nm$) and angular velocity ($360 \; deg/s$) requirements, as observed from the slip experiments. The controller design and extensive human subject testing of the robotic knee device remain as our future work and are out of the scope of this dissertation.

7.2   Future work

As the future extension of this dissertation and our slip-and-fall study, we plan to conduct bench testing of our wearable robotic knee assistive device to guarantee the optimal and safe operation of the device. Next, we plan to implement the impedance control for the human-device interaction and test the device on human subjects. Further control strategies based on the human responses to the device actuation might be considered and evaluated as an ongoing research development. At the last stage, we will implement and test the device for prevention of falls for healthy subjects under foot slip.

Note that the fall prevention device developed in this dissertation is a preliminary version and will not have the capabilities to prevent all possible slip-induced falls. The presented device is designed for fall prevention of only one specific slip case, more particularly, a slip starting shortly after the heel strike, because of its common occurrence in personal daily activities. Indeed, depending on the severity of the slip, the control

strategies may vary quite significantly. Additional extension of the proposed work and also an alternative to our proposed recovery control strategy approach is to actuate also the swing leg during slip and therefore shorten the compensatory step length. Compensatory stepping was suggested to be the key factor to maintain stability during balance loss [123]. The advantage of such an approach would be to instantaneously increase the base of support during slip and chances of recovery. Moreover, due to the presence of potential high interaction forces at the human-device interface, special care and consideration will have to be taken during human subject testing. For subject testing and evaluation of the functionality of the device, we plan to discuss and work with our partners at Kessler Institute of Rehabilitation. We will evaluate the proposed control and robotic devices on multiple subjects under the clinicians guidance and use the existing balance criteria and scales to determine the successful rate under the support of our assistive devices.

Further future direction of our research lies in an additional extension of our theoretical and simulation-based approach of foot slip analysis. We are currently working on integration of the two-mass LIP model and balance control with the multi-link bipedal model to investigate the optimal control laws to recover stability during walking with foot slip. Along this research avenue, another research approach is to integrate the two-mass LIP model and balance controllers of the wearable robotic knee assistive device for slip-and-fall prevention. Optimization based full-body control frame work can be one solution to design the balance controller.

Another ongoing research task, is the integration of the slip detection algorithm with the wearable robotic assistive devices to prevent slip-and-fall. Further improvement of the accuracy of the proposed slip detection algorithm can be investigated through the extensive human subject experiments. We plan to further investigate the shoe-floor interactions by applying the presented dynamic soft-solid contact model for slip prediction. Applying the soft-solid contact model to other robotic and mechatronic

systems such as tire-road interactions and robotic grasping is also among the future research directions.

References

[1] A. D. Kuo, "The six determinants of gait and the inverted pendulum analogy: A dynamic walking perspective," *Human movement science*, vol. 26, no. 4, pp. 617–656, 2007.

[2] J. M. Hausdorff, D. A. Rios, and H. K. Edelberg, "Gait variability and fall risk in community-living older adults: a 1-year prospective study," *Arch. Phys. Med. Rehabil.*, vol. 82, no. 8, pp. 1050–1056, 2001.

[3] B. S. Roudsari, B. E. Ebel, P. S. Corso, N. M. Molinari, and T. D. Koepsell, "The acute medical care costs of fall-related injuries among the us older adults," *Injury*, vol. 36, no. 11, pp. 1316–1322, 2005.

[4] T. Bentley and R. Haslam, "Slip, trip and fall accidents occurring during the delivery of mail," *Ergonomics*, vol. 41, no. 12, pp. 1859–1872, 1998.

[5] J. L. Bell, J. W. Collins, L. Wolf, R. R. Grönqvist, S. Chiou, W.-R. Chang, G. S. Sorock, T. K. Courtney, D. A. Lombardi, and B. Evanoff, "Evaluation of a comprehensive slip, trip and fall prevention programme for hospital employees," *Ergonomics*, vol. 51, no. 12, pp. 1906–1925, 2008.

[6] T. K. Courtney, G. S. Sorock, D. P. Manning, J. W. Collins, and M. A. Holbein-Jenny, "Occupational slip, trip, and fall-related injuries-can the contribution of slipperiness be isolated?" *Ergonomics*, vol. 44, no. 13, pp. 1118–1137, 2001.

[7] J. A. Stevens, P. S. Corso, E. A. Finkelstein, and T. R. Miller, "The costs of fatal and non-fatal falls among older adults," *Inj. Prev.*, vol. 12, pp. 290–295, 2006.

[8] F. Englander, T. J. Hodson, and R. A. Terregrossa, "Economic dimensions of slip and fall injuries," *J. Forensic Sci.*, vol. 41, no. 5, pp. 733–746, 1996.

[9] http://www.libertymutualgroup.com.

[10] M. S. Redfern, R. Cham, K. Gielo-Perczak, R. Grönqvist, M. Hirvonen, H. Lanshammar, C. Y.-C. Pai, and C. Power, "Biomechanics of slips," *Ergonomics*, vol. 44, no. 13, pp. 1138–1166, 2001.

[11] F. Yang and Y.-C. Pai, "Reactive control and its operation limits in responding to a novel slip in gait," *Ann. Biomed. Eng.*, vol. 38, no. 10, pp. 3246–3256, 2010.

[12] W.-R. Chang, R. Grönqvist, S. Leclercq, R. Myung, L. Makkonen, L. Strandberg, R. J. Brungraber, U. Mattke, and S. C. Thorpe, "The role of friction in the

measurement of slipperness, Part 1: Friction mechanisms and definition of test conditions," *Ergonomics*, vol. 44, no. 13, pp. 1217–1232, 2001.

[13] W.-R. Chang, C.-C. Chang, and S. Matz, "The effect of transverse shear force on the required coefficient of friction for level walking," *Human Factors*, vol. 53, no. 5, pp. 461–473, 2011.

[14] R. Grönqvist, W.-R. Chang, , T. K. Courtney, T. B. Leamon, M. S. Redfern, and L. Strandberg, "Measurement of slipperiness: Fundamental concept and definitions," *Ergonomics*, vol. 44, no. 13, pp. 1102–1117, 2001.

[15] W.-R. Chang, R. Grönqvist, S. Leclercq, R. J. Brungraber, U. Mattke, L. Strandberg, S. C. Thorpe, R. Myung, L. Makkonen, and T. K. Courtney, "The role of friction in the measurement of slipperness, Part 2: Survey of friction measurement devices," *Ergonomics*, vol. 44, no. 13, pp. 1233–1261, 2001.

[16] R. Cham and M. S. Redfern, "Heel contact dynamics during slip events on level and inclined surfaces," *Safety Sci.*, vol. 40, pp. 559–576, 2002.

[17] J. M. Burnfield and C. M. Power, "The role of center of mass kinematics in predicting peak utilized coefficent of friction during walking," *J. Forensic Sci.*, vol. 52, no. 6, pp. 1328–1333, 2007.

[18] T. Yamaguchi, M. Yano, H. Onodera, and K. Hokkorogawa, "Kinematics of center of mass and center of pressure predict friction requirement at shoe-floor interface during walking," *Gait & Posture*, vol. 38, pp. 209–214, 2013.

[19] S. T. Osis, J. T. Worobets, and D. J. Stefanyshyn, "Early heelstrike kinetics are indicative of slip potential during walking over a contaminated surface," *Human Factors*, vol. 54, no. 1, pp. 5–13, 2012.

[20] J. Bae, K. Kong, N. Byl, and M. Tomizuka, "A mobile gait monitoring system for abnormal gait diagnosis and rehabilitation: A pilot study for Parkinson disease patients," *ASME J. Biomech. Eng.*, vol. 133, 2011, paper #041005.

[21] D. Rosenbaum and H.-P. Becker, "Plantar pressure distribution measurement: Technical background and clinical applications," *Foot Ankle Surg.*, vol. 3, pp. 1–14, 1997.

[22] Z. Sawacha, G. Guarneri, G. Cristoferi, A. Guiotto, A. Avogaro, and C. Cobelli, "Integrated kinematics-kinetics-plantar pressure data analysis: A useful tool for characterizing diabetic foot biomechanics," *Gait & Posture*, vol. 36, pp. 20–36, 2012.

[23] A. F. Cordero, H. J. F. M. Koopman, and F. C. T. van der Helm, "Use of pressure insoles to calculate the complete ground reaction forces," *J. Biomech.*, vol. 37, pp. 1427–1432, 2004.

[24] S. Stucke, D. McFarland, L. Goss, S. Fonov, G. R. McMillan, A. Tucker, N. Berme, H. C. Guler, C. Bigelow, and B. L. Davis, "Spatial relationships between shearing stresses and pressure on the plantar skin surface during gait," *J. Biomech.*, vol. 45, pp. 619–622, 2012.

[25] S. Bamberg, A. Y. Benbasat, D. M. Scarborough, D. E. Krebs, and J. A. Paradiso, "Gait analysis using a shoe-integrated wireless sensor system," *IEEE Trans. Inform. Technol. Biomed.*, vol. 12, no. 4, pp. 413–423, 2008.

[26] C. Giacomozzi and V. Macellari, "Piezo-dynamometric platform for a more complete analysis of foot-to-floor interaction," *IEEE Trans. Rehab. Eng.*, vol. 5, no. 4, pp. 322–330, 1997.

[27] P. H. Veltink, C. Liedtke, E. Droog, and H. van der Kooij, "Ambulatory measurement of ground reaction forces," *IEEE Trans. Neural Syst. Rehab. Eng.*, vol. 13, no. 3, pp. 423–427, 2005.

[28] H. Rouhani, J. Favre, X. Crevoisier, and K. Aminian, "Ambulatory measurement of 3d ground reaction force using plantar pressure distribution," *Gait & Posture*, vol. 32, pp. 311–316, 2010.

[29] T. Liu, Y. Inoue, K. Shibata, and K. Shiojima, "A mobile force plate and three-dimensional motion analysis system for three-dimensional gait assessment," *IEEE Sensors J.*, vol. 12, no. 5, pp. 1461–1467, 2012.

[30] H. Liu, K. Wu, P. Meusel, N. Seitz, G. Hirzinger, M. H. Jin, Y. W. Liu, S. W. Fan, T. Lan, and Z. P. Chen, "Multisensory five-finger dexterous hand: The DLR/HIT hand II," in *Proc. IEEE/RSJ Int. Conf. Intell. Robot. Syst.*, Nice, France, 2008, pp. 3692–3697.

[31] L. Beccai, S. Roccella, L. Ascari, P. Valdastri, A. Sieber, M. C. Carrozza, and P. Dario, "Development and experimental analysis of a soft compliant tactile microsensor for anthropomorphic artificial hand," *IEEE/ASME Trans. Mechatronics*, vol. 13, no. 2, pp. 158–168, 2008.

[32] M. Trkov, J. Yi, T. Liu, and K. Li, "Shoe-floor interactions during human slip and fall: Modeling and experiments," in *Proc. ASME Dyn. Syst. Control Conf.*, San Antonio, TX, 2014, Paper DSCC2014-6184.

[33] Y. Zhang and J. Yi, "Static tire/road stick-slip interactions: Analysis and experiments," *IEEE/ASME Trans. Mechatronics*, vol. 19, no. 6, pp. 1940–1950, 2014.

[34] R. S. Dahiya, G. Metta, M. Valle, and G. Sandini, "Tactile sensing – From humans to humanoids," *IEEE Trans. Robotics*, vol. 26, no. 1, pp. 1–20, 2010.

[35] R. Fearing and J. Hollerbach, "Basic solid mechanics for tactile sensing," *Int. J. Robot. Res.*, vol. 4, no. 3, pp. 40–54, 1985.

[36] P. Tiezzi and I. Kao, "Modeling of viscoelastic contacts and evolution of limit surface for robotic contact interface," *IEEE Trans. Robotics*, vol. 23, no. 2, pp. 206–217, 2007.

[37] V.-A. Ho, D. V. Dao, and S. Hirai, "Development and analysis of a sliding tactile soft fingertip embedded with a microforce/moment sensor," *IEEE Trans. Robotics*, vol. 27, no. 3, pp. 411–424, 2011.

[38] V. A. Ho and S. Hirai, "Understanding slip perception of soft fingertips by modeling and simulating stick-slip phenomenon," in *Proc. Robotics: Sci. Syst.*, Los Angles, CA, 2011.

[39] T. Maeno, T. Kawamura, and S.-C. Cheng, "Friction estimation by pressing an elastic finger-shaped sensor against a surface," *IEEE Trans. Robot. Automat.*, vol. 20, no. 2, pp. 222–228, 2004.

[40] J. Ueda, A. Ikeda, and T. Ogagawara, "Grip-force control of an elastic object by vision-based slip-margin feedback during the incipient slip," *IEEE Trans. Robotics*, vol. 21, no. 6, pp. 1139–1147, 2005.

[41] K. Åström and C. Canudas-de-Wit, "Revisiting the LuGre friction model," *IEEE Control Syst. Mag.*, vol. 28, no. 6, pp. 101–114, 2008.

[42] J. Yi, L. Alvarez, X. Claeys, and R. Horowitz, "Tire/road friction estimation and emergency braking control using a dynamic friction model," *Veh. Syst. Dyn.*, vol. 39, no. 2, pp. 81–97, 2003.

[43] C. Canudas-de-Wit, P. Tsiotras, E. Velenis, M. Basset, and G. Gissinger, "Dynamic friction models for road/tire longitudinal interaction," *Veh. Syst. Dyn.*, vol. 39, no. 3, pp. 189–226, 2003.

[44] J. Deur, J. Asgari, and D. Hrovat, "A 3D brush-type dynamic tire friction model," *Veh. Syst. Dyn.*, vol. 42, no. 3, pp. 133–173, 2004.

[45] W. Liang, J. Medanic, and R. Ruhl, "Analytical dynamic tire model," *Veh. Syst. Dyn.*, vol. 46, no. 3, pp. 197–227, 2008.

[46] J. Li, Y. Zhang, and J. Yi, "A hybrid physical-dynamic tire/road friction model," *ASME J. Dyn. Syst., Meas., Control*, vol. 135, no. 1, pp. 011 007–1–011 007–11, 2013.

[47] Y. Zhang, J. Yi, and T. Liu, "An embedded local force sensor for *in-situ* tire-road interaction measurements," *IEEE Sensors J.*, vol. 13, no. 5, pp. 1756–1765, 2013.

[48] Y. Zhang, A. W. Allen, J. Yi, and T. Liu, "Understanding tire/road stick-slip interactions with embedded rubber force sensors," in *Proc. IEEE/ASME Int. Conf. Adv. Intelli. Mechatronics*, Kaohsiung, Taiwan, 2012, pp. 550–555.

[49] E. R. Westervelt, J. W. Grizzle, C. Chevallereau, J. H. Choi, and B. Morris, *Feedback control of dynamic bipedal robot locomotion*. Boca Raton, FL: CRC Press, 2007.

[50] E. R. Westervelt, J. W. Grizzle, and D. E. Koditschek, "Hybrid zero dynamics of planar biped walkers," *IEEE Trans. Automat. Contr.*, vol. 48, no. 1, pp. 42–56, 2003.

[51] S. Srinivasan, "Low-dimensional modeling and analysis of human gait with application to the gait of transtibial prosthesis users," Ph.D. dissertation, Dept. Mech. Eng., Ohio State Univ., Columbus, OH, 2007.

[52] A. E. Martin and J. P. Schmiedeler, "Predicting human walking gaits with a simple planar model," *J. Biomech.*, vol. 47, pp. 1416–1421, 2014.

[53] A. H. Hansen, D. S. Childress, and E. H. Knox, "Roll-over shapes of human locomotor systems: Effects of walking speed," *Clin. Biomech.*, vol. 19, no. 4, pp. 407–414, 2004.

[54] T. Sugihara, Y. Nakamura, and H. Inoue, "Real-time humanoid motion generation through zmp manipulation based on inverted pendulum control," in *Robotics and Automation, 2002. Proceedings. ICRA'02. IEEE International Conference on*, vol. 2. IEEE, 2002, pp. 1404–1409.

[55] H. Geyer, A. Seyfarth, and R. Blickhan, "Compliant leg behaviour explains basic dynamics of walking and running," *Proceedings of the Royal Society of London B: Biological Sciences*, vol. 273, no. 1603, pp. 2861–2867, 2006.

[56] A. Hereid, M. J. Powell, and A. D. Ames, "Embedding of slip dynamics on underactuated bipedal robots through multi-objective quadratic program based control," in *Decision and Control (CDC), 2014 IEEE 53rd Annual Conference on*. IEEE, 2014, pp. 2950–2957.

[57] A. L. Hof, "The extrapolated center of mass concept suggests a simple control of balance in walking," *Human movement science*, vol. 27, no. 1, pp. 112–125, 2008.

[58] J. Pratt, J. Carff, S. Drakunov, and A. Goswami, "Capture point: A step toward humanoid push recovery," in *Humanoid Robots, 2006 6th IEEE-RAS International Conference on*. IEEE, 2006, pp. 200–207.

[59] T. Takenaka, T. Matsumoto, and T. Yoshiike, "Real time motion generation and control for biped robot-1 st report: Walking gait pattern generation," in *Proc. IEEE/RSJ Int. Conf. Intell. Robot. Syst.* IEEE, 2009, pp. 1084–1091.

[60] J. Englsberger, C. Ott, M. A. Roa, A. Albu-Schäffer, and G. Hirzinger, "Bipedal walking control based on capture point dynamics," in *Proc. IEEE/RSJ Int. Conf. Intell. Robot. Syst.* IEEE, 2011, pp. 4420–4427.

[61] J. Englsberger, C. Ott, and A. Albu-Schäffer, "Three-dimensional bipedal walking control based on divergent component of motion," *IEEE Trans. Robotics*, vol. 31, no. 2, pp. 355–368, 2015.

[62] M. A. Hopkins, D. W. Hong, and A. Leonessa, "Humanoid locomotion on uneven terrain using the time-varying divergent component of motion," in *Humanoid Robots (Humanoids), 2014 14th IEEE-RAS International Conference on*. IEEE, 2014, pp. 266–272.

[63] J. Patton, Y.-C. Pai, and W. A. Lee, "Evaluation of a model that determines the stability limits of dynamic balance," *Gait & Posture*, vol. 9, pp. 38–49, 1999.

[64] A. Mahboobin, R. Cham, and S. J. Piazza, "The impact of a systematic reduction in shoe-floor friction on heel contact walking kinematics - A gait simulation approach," *J. Biomech.*, vol. 43, pp. 1532–1539, 2010.

[65] J. B. Dingwell and H. G. Kang, "Differences between local and orbital dynamic stability during human walking," *ASME J. Biomech. Eng.*, vol. 129, pp. 586–593, 2007.

[66] L. Strandberg and H. Lanshammar, "The dynamics of slipping accidents," *J. Occupat. Accidents*, vol. 3, pp. 153–162, 1981.

[67] R. A. Brady, M. J. Pavol, T. M. Owings, and M. D. Grabiner, "Foot displacement but not velocity predicts the outcome of a slip induced in young subjects while walking," *J. Biomech.*, vol. 33, pp. 803–808, 2000.

[68] P. J. Perkins, "Measurement of slip between the shoe and ground during walking," in *Walkway Surfaces: Measurements of Slip Resistance*, C. Anderson and J. Senne, Eds. Philadelphia, PA: ASTM, 1978, vol. ASTM-STP 649.

[69] T. E. Lockhart, J. C. Woldstad, and J. L. Smith, "Effects of age-related gait changes on the biomechanics of slips and falls," *Ergonomics*, vol. 46, no. 12, pp. 1136–1160, 2003.

[70] R. W. McGorry, A. DiDomenico, and C.-C. Chang, "The anatomy of a slip: Kinetic and kinematic characteristics of slip and non-slip matched trials," *Appl. Ergon.*, vol. 41, pp. 41–46, 2010.

[71] B. E. Moyer, A. J. Chambers, M. S. Redfern, and R. Cham, "Gait parameters as predictors of slip severity in younger and older adults," *Ergonomics*, vol. 49, no. 4, pp. 329–343, 2006.

[72] K. Chen, M. Trkov, J. Yi, Y. Zhang, T. Liu, and D. Song, "A robotic bipedal model for human walking with slips," in *Proc. IEEE Int. Conf. Robot. Autom.*, Seattle, WA, 2015.

[73] H. Onodera, T. Yamaguchi, H. Yamanouchi, K. Nagamori, M. Yano, Y. Hirata, and K. Hokkirigawa, "Analysis of the slip-related falls and fall prevention with an intelligent shoe system," in *Biomedical Robotics and Biomechatronics (BioRob), 2010 3rd IEEE RAS and EMBS International Conference on*. IEEE, 2010, pp. 616–620.

[74] G. Shi, C. S. Chan, W. J. Li, K.-S. Leung, Y. Zou, and Y. Jin, "Mobile human airbag system for fall protection using mems sensors and embedded svm classifier," *Sensors Journal, IEEE*, vol. 9, no. 5, pp. 495–503, 2009.

[75] T. Tamura, T. Yoshimura, M. Sekine, M. Uchida, and O. Tanaka, "A wearable airbag to prevent fall injuries," *Information Technology in Biomedicine, IEEE Transactions on*, vol. 13, no. 6, pp. 910–914, 2009.

[76] J. B. Andersen and T. Sinkjær, "An actuator system for investigating electrophysiological and biomechanical features around the human ankle joint during gait," *IEEE Trans. Biomed. Eng.*, vol. 3, no. 4, pp. 299–306, 1995.

[77] ——, "Mobile ankle and knee perturbator," *IEEE Trans. Biomed. Eng.*, vol. 50, no. 10, pp. 1208–1211, 2003.

[78] M. R. Tucker, A. Moser, O. Lambercy, J. Sulzer, and R. Gassert, "Design of a wearable perturbator for human knee impedance estimation during gait," in *Proc. 2013 IEEE Int. Conf. Rehabil. Robot.*, Seattle, WA, June 2013.

[79] J. S. Sulzer, R. A. Roiz, M. A. Peshkin, and J. L. Patton, "A highly backdrivable, lightweight knee actuator for investigating gait in stroke," *IEEE Trans. Robotics*, vol. 25, no. 3, pp. 539–548, 2009.

[80] T. Bhatt, J. D. Wening, and Y.-C. Pai, "Adaptive control of gait stability in reducing slip-related backward loss of balance," *Experimental Brain Research*, vol. 170, no. 1, pp. 61–73, 2006.

[81] P. Parijat and T. E. Lockhart, "Effects of movable platform training in preventing slip-induced falls in older adults," *Ann. Biomed. Eng.*, vol. 40, no. 5, pp. 1111–1121, 2012.

[82] F. Yang, T. Bhatt, and Y.-C. Pai, "Generalization of treadmill-slip training to prevent a fall following a sudden (novel) slip in over-ground walking," *Journal of biomechanics*, vol. 46, no. 1, pp. 63–69, 2013.

[83] T. Bhatt, F. Yang, and Y.-C. Pai, "Learning to resist gait-slip falls: long-term retention in community-dwelling older adults," *Archives of physical medicine and rehabilitation*, vol. 93, no. 4, pp. 557–564, 2012.

[84] R. Cham and M. S. Redfern, "Lower extremity corrective reactions to slip events," *J. Biomech.*, vol. 34, pp. 1439–1445, 2001.

[85] J. Liu and T. E. Lockhart, "Age-related joint moment characteristics during normal gait and successful reactive-recovery from unexpected slip perturbations," *Gait & Posture*, vol. 30, no. 3, pp. 276–281, 2009.

[86] A. J. Chambers and R. Cham, "Slip-related muscle activation patterns in the stance leg during walking," *Gait & Posture*, vol. 25, pp. 565–572, 2007.

[87] S. A. Wyszomierski, A. J. Chambers, and R. Cham, "Knee strength capabilities and slip severity," *J. App. Biomech*, vol. 25, pp. 140–148, 2009.

[88] R. Grönqvist, J. Abeysekera, G. Gard, S. M. Hsiang, T. B. Leamon, D. J. Newman, K. Gielo-Perczak, T. E. Lockhart, and C. Y.-C. Pai, "Human-centred approaches in slipperiness measurement," *Ergonomics*, vol. 44, no. 13, pp. 1167–1199, 2001.

[89] J. E. Perry, J. O. Hall, and B. L. Davis, "Simultaneous measurement of plantar pressure and shear forces in diabetic individuals," *Gait & posture*, vol. 15, no. 1, pp. 101–107, 2002.

[90] J. R. Mackey and B. L. Davis, "Simultaneous shear and pressure sensor array for assessing pressure and shear at foot/ground interface," *J. Biomech.*, vol. 39, no. 15, pp. 2893–2897, 2006.

[91] M. Yavuz, G. Botek, and B. L. Davis, "Plantar shear stress distributions: comparing actual and predicted frictional forces at the foot–ground interface," *J. Biomech.*, vol. 40, no. 13, pp. 3045–3049, 2007.

[92] M. Ueda, K. Sekiguchi, H. Takemura, and H. Mizoguchi, "Plantar 3-axis distributed forces sensor based on measurement of silicone rubber deformation for walking analysis," in *Sensors, 2008 IEEE*. IEEE, 2008, pp. 945–948.

[93] H. Uno, H. Takemura, and H. Mizoguchi, "An effect on walk and plantar contact area from ice immersion approach," in *Systems, Man and Cybernetics, 2007. ISIC. IEEE International Conference on*. IEEE, 2007, pp. 1524–1529.

[94] F. S. Abuzzahab, G. F. Harris, and S. M. Kidder, "A kinetic model of the foot and ankle," *Gait & Posture*, vol. 5, no. 2, p. 148, 1997.

[95] C. Giacomozzi and V. Macellari, "Piezo-dynamometric platform for a more complete analysis of foot-to-floor interaction," *IEEE Trans. Rehab. Eng.*, vol. 5, no. 4, pp. 322–330, 1997.

[96] H. B. Pacejka, *Tire and vehicle dynamics*, 2nd ed. Warrendale, PA: SAE International, 2006.

[97] M. Tada and T. Kanade, "An imaging system of incipient slip for modelling how human perceives slip of a fingertip," in *Engineering in Medicine and Biology Society, 2004. IEMBS'04. 26th Annual International Conference of the IEEE*, vol. 1. IEEE, 2004, pp. 2045–2048.

[98] Y. Zhang and J. Yi, "Tire/road stick-slip interactions: Analysis and experiments," in *Proc. ASME Dyn. Syst. Control Conf.*, Ft. Lauderdale, FL, 2012, Paper # DSCC2012-8619.

[99] M. Abramowitz and I. A. Stegun, *Handbook of mathematical functions: with formulas, graphs, and mathematical tables*. Mineola, NY: Dover Publications, 1964.

[100] H. Olsson, "Control systems with friction," Ph.D. dissertation, Dept. Automat. Contr., Lund Inst. Tech., Lund, Sweden, 1996.

[101] C. C. De Wit, H. Olsson, K. J. Astrom, and P. Lischinsky, "A new model for control of systems with friction," *Automatic Control, IEEE Transactions on*, vol. 40, no. 3, pp. 419–425, 1995.

[102] S. Srinivasan, I. A. Raptis, and E. R. Westervelt, "Low-dimensional sagittal plane model of normal human walking," *ASME J. Biomech. Eng.*, vol. 130, pp. 051 017–1–051 017–11, 2008.

[103] C. Chevallereau, D. Djoudi, and J. W. Grizzle, "Stable bipedal walking with foot rotation through direct regulation of the zero moment point," *IEEE Trans. Robotics*, vol. 24, no. 2, pp. 390–401, 2008.

[104] D. J. Braun and M. Goldfarb, "A control approach for actuated dynamic walking in biped robots," *IEEE Trans. Robotics*, vol. 25, no. 6, pp. 1292–1303, 2009.

[105] H.-H. Zhao, W.-L. Ma, M. B. Zeagler, and A. D. Ames, "Human-inspired multi-contact locomotion with AMBER2," in *Proc. ACM/IEEE Int. Conf. Cyber-Phys. Syst.*, Berlin, Germany, 2014.

[106] Y. Zhang, K. Chen, J. Yi, and L. Liu, "Pose estimation in physical human-machine interactions with application to bicycle riding," in *Proc. IEEE/RSJ Int. Conf. Intell. Robot. Syst.*, Chicago, IL, 2014, pp. 3333–3338.

[107] A. M. Sabatini, C. Martelloni, S. Scapellato, and F. Cavallo, "Assessment of walking features from foot inertial sensing," *IEEE Trans. Biomed. Eng.*, vol. 52, no. 3, pp. 486–494, 2005.

[108] I. P. I. Pappas, M. R. Popovic, T. Keller, V. Dietz, and M. Morari, "A reliable gait phase detection systemgyroscope-based gait-phase detection sensor embedded in a shoe insole," *IEEE Trans. Neural Syst. Rehab. Eng.*, vol. 9, no. 2, pp. 113–125, 2001.

[109] K. Aminian, B. Najafi, C. Bla, P.-F. Leyvraz, and P. Robert, "Spatio-temporal parameters of gait measured by an ambulatory system using miniature gyroscopes," *J. Biomech.*, vol. 35, no. 5, pp. 689 – 699, 2002.

[110] R. W. Selles, M. A. G. Formanoy, J. B. J. Bussmann, P. J. Janssens, , and H. J. Stam, "Automated estimation of initial and terminal contact timing using Accelerometers; Development and validation in transtibial amputees and controls," *IEEE Trans. Neural Syst. Rehab. Eng.*, vol. 13, no. 1, pp. 81–88, 2005.

[111] J. M. Jasiewicz, J. H. Allum, J. W. Middleton, A. Barriskill, P. Condie, B. Purcell, and R. C. T. Li, "Gait event detection using linear accelerometers or angular velocity transducers in able-bodied and spinal-cord injured individuals," *Gait & Posture*, vol. 24, pp. 502–509, 2006.

[112] B. Mariani, S. Rochat, C. J. Büla, and K. Aminian, "Heel and toe clearance estimation for gait analysis using wireless inertial sensors," *IEEE Trans. Biomed. Eng.*, vol. 59, no. 11, pp. 3162–3168, 2012.

[113] N. C. Bejarano, E. Ambrosini, A. Pedrocchi, G. Ferrigno, M. Monticone, and S. Ferrante, "A novel adaptive, real-time algorithm to detect gait events from wearable sensors," *IEEE Trans. Neural Syst. Rehab. Eng.*, vol. 23, no. 3, pp. 413–422, 2015.

[114] K. Liu, T. Liu, K. Shibata, Y. Inoue, and R. Zheng, "Novel approach to ambulatory assessment of human segmental orientation on a wearable sensor system," *J. Biomech.*, vol. 42, pp. 2747–2752, 2009.

[115] Y. Zhang, K. Chen, and J. Yi, "Rider trunk and bicycle pose estimation with fusion of force/inertial sensors," *IEEE Trans. Biomed. Eng.*, vol. 60, no. 9, pp. 2541–2551, 2013.

[116] K. Liu, T. Liu, K. Shibata, Y. Inoue, and R. Zheng, "Novel approach to ambulatory assessment of human segmental orientation on a wearable sensor system," *J. Biomech.*, vol. 42, no. 16, pp. 2747–2752, 2009.

[117] J. Yi, H. Wang, J. Zhang, D. Song, S. Jayasuriya, and J. Liu, "Kinematic modeling and analysis of skid-steered mobile robots with applications to low-cost inertial-measurement-unit-based motion estimation," *IEEE Trans. Robotics*, vol. 25, no. 5, pp. 1087–1097, 2009.

[118] D. Kotiadis, H. J. Hermens, and P. H. Veltink, "Inertial gait phase detection for control of a drop foot stimulator inertial sensing for gait phase detection," *Med. Eng. & Phys.*, vol. 32, no. 4, pp. 287–298, 2010.

[119] A. E. Patla, "Strategies for dynamic stability during adaptive human locomotion," *IEEE Eng. Med. Biol. Mag.*, vol. 22, no. 2, pp. 48–52, 2003.

[120] M. Trkov, K. Chen, J. Yi, and T. Liu, "Slip detection and prediction in human walking using only wearable inertial measurement units (IMUs)," in *Proc. IEEE/ASME Int. Conf. Adv. Intelli. Mechatronics*, Busan, Korea, 2015, pp. 854–859.

[121] D. S. Marigold and A. E. Patla, "Strategies for dynamic stability during locomotion on a slippery surface: Effects of prior experience and knowledge," *J. Neurophysiol.*, vol. 88, no. 1, pp. 339–353, 2002.

[122] T. L. Heiden, D. J. Sanderson, J. T. Inglis, and G. P. Siegmund, "Adaptation to normal human gait on potentially slippery surfaces: The effects of awareness and prior slip experience," *Gait & Posture*, vol. 24, pp. 237–246, 2006.

[123] Y.-C. P. T. Bhatt, J.D. Wening, "Influence of gait speed on stability: recovery from anterior slips and compensatory stepping," *Gait & Posture*, vol. 21, p. 146156, 2005.

[124] K. Chen, M. Trkov, S. Chen, and J. Yi, "Balance recovery control of human walking with slips," 2016, accepted at *2016 American Control Conference*.

[125] Y.-C. Pai and T. S. Bhatt, "Repeated-slip training: an emerging paradigm for prevention of slip-related falls among older adults," *Phys. Ther.*, vol. 87, no. 11, pp. 1478–1491, 2007.

[126] A. M. Dollar and H. Herr, "Lower extremity exoskeletons and active orthoses: challenges and state-of-the-art," *IEEE Trans. Robotics*, vol. 24, no. 1, pp. 144–158, 2008.

[127] I. Díaz, J. J. Gil, and E. Sánchez, "Lower-limb robotic rehabilitation: literature review and challenges," *Journal of Robotics*, vol. 2011, 2011, article ID 759764.

[128] S. Viteckova, P. Kutilek, and M. Jirina, "Wearable lower limb robotics: a review," *Biocyber. and Biomed. Eng.*, vol. 33, no. 2, pp. 96–105, 2013.

[129] G. Elliott, G. S. Sawicki, A. Marecki, and H. Herr, "The biomechanics and energetics of human running using an elastic knee exoskeleton," in *Proc. 2013 IEEE Int. Conf. Rehabil. Robot.*, Seattle, WA, June 2013.

[130] G. Elliott, A. Marecki, and H. Herr, "Design of a clutch-spring knee exoskeleton for running," *J. Med. Devices*, vol. 8, no. 3, 2014.

[131] A. Zoss and H. Kazerooni, "Design of an electrically actuated lower extremity exoskeleton," *Adv. Robot.*, vol. 20, no. 9, pp. 967–988, 2006.

[132] J. F. Veneman, R. Ekkelenkamp, R. Kruidhof, F. C. T. van der Helm, and H. Van Der Kooij, "A series elastic-and bowden-cable-based actuation system for use as torque actuator in exoskeleton-type robots," *Int. J. Robot. Res.*, vol. 25, no. 3, pp. 261–281, 2006.

[133] J. F. Veneman, R. Kruidhof, E. E. G. Hekman, R. Ekkelenkamp, E. H. F. Van Asseldonk, and H. Van Der Kooij, "Design and evaluation of the LOPES exoskeleton robot for interactive gait rehabilitation," *IEEE Trans. Neural Syst. Rehab. Eng.*, vol. 15, no. 3, pp. 379–386, 2007.

[134] H. Kazerooni, R. Steger, and L. Huang, "Hybrid control of the Berkeley lower extremity exoskeleton (BLEEX)," *Int. J. Robot. Res.*, vol. 25, no. 5-6, pp. 561–573, 2006.

[135] M. A. M. Dzahir and S. ichiroh Yamamoto, "Recent trends in lower-limb robotic rehabilitation orthosis: control scheme and strategy for pneumatic muscle actuated gait trainers," *Robotics*, vol. 3, no. 2, pp. 120–148, 2014.

[136] H. Herr and A. Wilkenfeld, "Useradaptive control of a magnetorheological prosthetic knee," *Ind. Robot*, vol. 30, no. 1, pp. 42–55, 2003.

[137] C. Mavroidis, J. Nikitczuk, B. Weinberg, G. Danaher, K. Jensen, P. Pelletier, J. Prugnarola, R. Stuart, R. Arango, M. Leahey, R. Pavone, A. Provo, and D. Yasevac, "Smart portable rehabilitation devices," *Journal of NeuroEngineering and Rehabilitation*, vol. 2, no. 18, 2005.

[138] J. Nikitczuk, B. Weinberg, P. K. Canavan, and C. Mavroidis, "Active knee rehabilitation orthotic device with variable damping characteristics implemented via an electrorheological fluid," *IEEE/ASME Trans. Mechatronics*, vol. 15, no. 6, pp. 952–960, 2010.

[139] H. Kawamoto and Y. Sankai, "Power assist system HAL-3 for gait disorder person," in *in Proc. Int. Conf. Comput. Helping People Special Needs (ICCHP) (Lecture Notes on Computer Science)*, vol. 2398, Berlin, 2002, berlin, Germany: Springer-Verlag.

[140] H. Kawamoto, S. Lee, S. Kanbe, and Y. Sankai, "Power assist method for HAL-3 using emg-based feedback controller," in *in Proc. IEEE Int. Conf. Syst., Man, Cybern.*, 2003, p. 16481653.

[141] G. Pratt and M. Williamson, "Series elastic actuators," in *Proc. IEEE/RSJ Int. Conf. Intell. Robot. Syst.*, Pittsburgh, PA, 1995, pp. 399–406, human Robot Interaction and Cooperative Robots.

[142] D. Robinson, J. Pratt, D. Paluska, and G. Pratt, "Series elastic actuator development for a biomimetic walking robot," in *Proc. IEEE/ASME Int. Conf. Adv. Intelli. Mechatronics*, Atlanta, USA, 1999, pp. 561–568.

[143] J. Sensinger and R. Weir, "Design and analysis of a nonbackdrivable series elastic actuator," in *Proc. 2005 IEEE Int. Conf. Rehabil. Robot.*, Seattle, WA, June 2005, pp. 390–393.

[144] A. Albu-Schaffer, O. Eiberger, M. Grebenstein, S. Haddadin, C. Ott, T. Wimbock, S. Wolf, and G. Hirzingers, "Soft robotics," *IEEE Robot. Automat. Mag.*, vol. 15, no. 3, pp. 20–30, 2008.

[145] J. E. Pratt, B. T. Krupp, C. J. Morse, , and S. H. Collins, "The RoboKnee: An exoskeleton for enhancing strength and endurance during walking," in *Proc. IEEE Int. Conf. Robot. Autom.*, New Orleans, LA, 2004, pp. 2430–2435.

[146] D. F. Häufle, M. D. Taylor, S. Schmitt, and H. Geyer, "A clutched parallel elastic actuator concept: towards energy efficient powered legs in prosthetics and robotics," in *Biomedical Robotics and Biomechatronics (BioRob), 2012 4th IEEE RAS & EMBS International Conference on.* Rome, Italy: IEEE, June 2012, pp. 1614–1619.

[147] E. J. Rouse, L. M. Mooney, E. C. Martinez-Villalpando, and H. M. Herr, "Clutchable series-elastic actuator: Design of a robotic knee prosthesis for minimum energy consumption," in *Proc. 2013 IEEE Int. Conf. Rehabil. Robot.*, Seattle, WA, June 2013.

[148] E. J. Rouse, L. M. Mooney, and H. M. Herr, "Clutchable series-elastic actuator: Implications for prosthetic knee design," *Int. J. Robot. Res.*, vol. 33, no. 13, pp. 1611–1625, 2014.

[149] N. Mrachacz-Kersting, B. A. Lavoie, J. B. Andersen, and T. Sinkjær, "Characterisation of the quadriceps stretch reflex during the transition from swing to stance phase of human walking," *Exp. Brain Res.*, vol. 159, no. 1, pp. 108–122, 2004.

[150] S. L. Delp, F. C. Anderson, A. Arnold, P. Loan, A. Habib, C. T. John, E. Guendelman, and D. G. Thelen, "OpenSim: open-source software to create and analyze dynamic simulations of mFovement," *IEEE Trans. Biomed. Eng.*, vol. 54, no. 11, pp. 1940–1950, 2007.

[151] D. A. Winter, *Biomechanics and motor control of human movement*, 2nd ed. New York, NY: Wiley and Sons, 1990.

[152] Hugh M. Herr and Jeff A. Weber and David A. Garlow and Richard J. Casler Jr , "Biomimetic joint actuators," US Patent 9,060,883, June 23, 2015.

[153] D. W. Robinson and G. A. Pratt, "Force controllable hydro-elastic actuator," in *Proc. IEEE Int. Conf. Robot. Autom.*, vol. 2, 2010, pp. 1321–1327.

[154] A. H. A. Stienen, E. E. G. Hekman, A. M. M. A. Huub ter Braak, F. C. T. van der Helm, and H. van der Kooij, "Design of a rotational hydroelastic actuator for a powered exoskeleton for upper limb rehabilitation," *IEEE Trans. Biomed. Eng.*, vol. 57, no. 3, pp. 728–735, 2010.

[155] C. Oertel, H. Neuburger, and A. Sabo, "Construction of a test bench for bicycle rim and disc brakes," *Procedia Engineering*, vol. 2, no. 2, pp. 2943–2948, 2010.

[156] M. W. Whitmore, L. J. Hargrove, and E. J. Perreault, "Gait characteristics when walking on different slipperys surfaces," *IEEE Trans. Biomed. Eng.*, vol. 63, no. 1, pp. 228–239, 2016.

[157] K. E. Beschorner, M. S. Redfern, and R. Cham, "Earliest gait deviations during slips: Implications for recovery," *IIE Trans. Occupat. Ergono. Human Fact.*, vol. 1, no. 1, pp. 31–37, 2013.

[158] D. W. Robinson, "Design and analysis of series elasticity in closed-loop actuator force control," Ph.D. dissertation, Massachusetts Institute of Technology, Cambridge, MA, 2000.

[159] K. Kong, J. Bae, and M. Tomizuka, "Control of rotary series elastic actuator for ideal force-mode actuation in humanrobot interaction applications," *IEEE/ASME Trans. Mechatronics*, vol. 14, no. 1, pp. 105–118, 2009.

[160] H. van der Kooij, J. F. Veneman, and R. Ekkelenkamp, *Compliant actuation of exoskeletons*. in Mobile RoboticsTowards New Applications, A. Lazinica, Ed. Mammendorf, Germany: Verlag Rober Mayer-Scholz, 2006.

[161] M. Zinn, B. Roth, O. Khatib, and J. K. Salisbury, "A new actuation approach for human friendly robot design," *Int. J. Robot. Res.*, vol. 23, no. 4-5, pp. 379–398, 2004.